

**Preliminary common-form ground-motion models  
for shallow crustal earthquakes and their use in  
ergodic and partially-ergodic seismic hazard  
calculations in New Zealand**

C Van Houtte

**GNS Science Report 2020/02  
March 2020**



## **DISCLAIMER**

The Institute of Geological and Nuclear Sciences Limited (GNS Science) and its funders give no warranties of any kind concerning the accuracy, completeness, timeliness or fitness for purpose of the contents of this report. GNS Science accepts no responsibility for any actions taken based on, or reliance placed on the contents of this report and GNS Science and its funders exclude to the full extent permitted by law liability for any loss, damage or expense, direct or indirect, and however caused, whether through negligence or otherwise, resulting from any person's or organisation's use of, or reliance on, the contents of this report.

## **BIBLIOGRAPHIC REFERENCE**

Van Houtte, C. 2020. Preliminary common-form ground-motion models for shallow crustal earthquakes and their use in ergodic and partially-ergodic seismic hazard calculations in New Zealand. Lower Hutt (NZ): GNS Science. 91 p. (GNS Science report; 2020/02). doi:10.21420/ZMCK-R234.

C Van Houtte, GNS Science, PO Box 30368, Lower Hutt, New Zealand

## CONTENTS

<b>ABSTRACT .....</b>	<b>V</b>
<b>KEYWORDS .....</b>	<b>V</b>
<b>1.0 INTRODUCTION .....</b>	<b>1</b>
<b>2.0 SEED MODEL SELECTION .....</b>	<b>4</b>
<b>3.0 FITTING MODELS TO COMMON FORM .....</b>	<b>6</b>
<b>4.0 SAMPLING NEW MODELS .....</b>	<b>9</b>
<b>5.0 COMMON FORM MODEL SELECTION .....</b>	<b>17</b>
5.1 Visualisation of Models .....	17
5.2 Selection Procedure .....	23
<b>6.0 STANDARD DEVIATION MODELS .....</b>	<b>26</b>
6.1 Components of Ground-Motion Standard Deviation .....	26
6.1.1 Selected Data .....	27
6.1.2 Form of The Model .....	28
6.1.3 Model Fit .....	29
6.2 Standard Deviation Results .....	31
6.2.1 Between-Event Standard Deviation, $\tau$ .....	31
6.2.2 Within-Event Standard Deviation, $\phi$ .....	32
6.2.3 Single-Station Within-Event Standard Deviation, $\phi_{SS}$ .....	34
6.2.4 Summary of Standard Deviation Observations .....	37
6.3 Selected Standard Deviation Models .....	38
6.3.1 Model for The Between-Event Standard Deviation, $\tau$ .....	38
6.3.2 Model for The Within-Event Standard Deviation, $\phi$ .....	39
6.3.3 Model for The Single-Station Within-Event Standard Deviation, $\phi_{SS}$ .....	39
6.3.4 Model for The Site-To-Site Standard Deviation, $\phi_{S2S}$ .....	39
6.3.5 Additional Considerations .....	40
6.4 Between-Station Terms, $\delta S2S_s$ .....	41
<b>7.0 MODEL WEIGHTING .....</b>	<b>45</b>
7.1 Prior Weights .....	45
7.2 Data-Driven Weights .....	46
7.2.1 Selection of Data .....	46
7.2.2 Mean Between-Event Residual .....	47
7.2.3 Log-Likelihood .....	48
7.3 Overall Weights .....	49
<b>8.0 ERGODIC HAZARD RESULTS .....</b>	<b>52</b>
<b>9.0 PARTIALLY-ERGODIC HAZARD RESULTS .....</b>	<b>55</b>
<b>10.0 DISCUSSION AND FUTURE WORK .....</b>	<b>59</b>
10.1 Use of These Crustal Models .....	59
10.2 Subduction Interface Models .....	59

10.3	Further Development on Ergodic Assumption Removal.....	59
10.3.1	$\delta S2S_s$ Terms for Both Crustal and Subduction Zone Models .....	59
10.3.2	Hazard Maps Using Partially-Ergodic Hazard Analyses .....	60
10.4	Epistemic Uncertainty in Hanging Wall Effects.....	60
10.5	Consideration of Simulated Data .....	61
10.6	Sensitivity Studies .....	61
<b>11.0</b>	<b>ACKNOWLEDGMENTS .....</b>	<b>62</b>
<b>12.0</b>	<b>REFERENCES .....</b>	<b>62</b>

## FIGURES

Figure 2.1	The selected seed models where grey bars represent the range of intensity measures that are predicted by each model. ....	5
Figure 3.1	PGA residuals from fitting the common-form model to the Boore et al. (2014) model.....	7
Figure 3.2	(a) Magnitude scaling for $R_{JB} = 1, 10, 30$ and $100$ km and (b) distance scaling for $M_W = 5, 6, 7,$ and $8$ , for the Boore et al. (2014) model compared to the fitted common-form model. All scenarios are on the footwall.....	7
Figure 3.3	The period-dependent log-likelihood of the common-form fit to the seed models. ....	8
Figure 4.1	(a) The parameters sampled from the multivariate normal distribution, and (b) the correlation matrix from the fitted distribution. ....	10
Figure 4.2	The parameters sampled from the multivariate normal distribution that are removed due to the parameter constraints for (a) PGA and (b) SA(3s). ....	13
Figure 4.3	Kernel density functions for each parameter before and after removal of implausible models for (a) PGA and (b) SA(3s). ....	14
Figure 4.4	The parameter samples after removal of implausible models for (a) PGA and (b) SA(3s). ....	15
Figure 4.5	(a) Magnitude and (b) distance scaling of PGA for the sampled common-form models, relative to the seed models. ....	16
Figure 4.6	(a) Magnitude and (b) distance scaling of SA(3s) for the sampled common-form models, relative to the seed models. ....	16
Figure 5.1	Generic suite of scenarios used to select a suite of widely-applicable ground-motion models... ..	18
Figure 5.2	The higher-dimensional PGA ground-motion space for the generic suite of scenarios .....	18
Figure 5.3	The Euclidean distance of the model to the central model prediction.....	19
Figure 5.4	Disaggregation of the PGA hazard at 0.1 probability of exceedance in 50 years.....	21
Figure 5.5	Two dimensional Sammon's map for the weighted scenarios from the PGA disaggregation.....	22
Figure 5.6	Variance explained by the first two principal components for the disaggregation-weighted scenarios .....	22
Figure 5.7	Workflow for selecting a representative suite of models from the Sammon's map.....	24
Figure 5.8	The (a) magnitude and (b) distance scaling of the selected PGA models, and (c) magnitude and (d) distance scaling .....	25
Figure 6.1	The data used to fit the Bayesian hierarchical model .....	28
Figure 6.2	Residuals of the model against (a) $M_W$ , (b) $R_{rup}$ , (c) $Z_{TOR}$ , (d) style-of-faulting.....	30
Figure 6.3	(a) the magnitude-dependence and (b) the distance-dependence of the fitted model, compared to the seed models, for PGA. ....	30
Figure 6.4	The magnitude-dependence of the between-event standard deviation .....	32

Figure 6.5	The magnitude-dependence of the within-event standard deviation .....	33
Figure 6.6	The distance-dependence of the within-event standard deviation.....	33
Figure 6.7	The magnitude-dependence of the single-station within-event standard deviation .....	35
Figure 6.8	The distance-dependence of the single-station within-event standard deviation.....	35
Figure 6.9	The dependence of the station-specific within-event standard deviation.....	36
Figure 6.10	The period-dependence of $\tau$ , $\phi$ , $\phi_{SS}$ and $\phi_{S2S}$ derived from New Zealand $M_W \geq 5$ data.....	38
Figure 6.11	The period-dependence of the $\tau$ , $\phi$ , $\phi_{SS}$ and $\phi_{S2S}$ models derived from New Zealand data.....	40
Figure 6.12	$\delta S2S_s$ functions at Wellington stations (a) WNAS, (b) POTS, (c) WEMS (d) VUWS, (e) TEPS and (f) FKPS.....	42
Figure 6.13	$\delta S2S_s$ functions at Christchurch stations (a) CBGS, (b) REHS, (c) CACS (d) HVSC, (e) STKS and (f) LPCC .....	43
Figure 6.14	Reduction in the 90% credible interval of the posterior distribution for $\delta S2S_s$ with increasing number of recordings at site $s$ .....	44
Figure 7.1	(a) and (c) probability density of the bivariate normal distribution.....	46
Figure 7.2	(a) and (c) the mean between-event residual for the widely-applicable set of models, for PGA and SA(3s) respectively. (b)-(d) the corresponding model weights based on the mean between-event residuals in (a) and (c).....	48
Figure 7.3	(a) and (c) the log-likelihood contours for the widely-applicable set of models, for PGA and SA(3s) respectively. (b)-(d) the corresponding model weights based on the mean between-event residuals in (a) and (c).....	50
Figure 7.4	Weights for the widely-applicable model set for PGA (a) prior weights, (b) mean between-event residual, (c) log-likelihood and (d) overall weights.....	51
Figure 8.1	Uniform hazard spectra for generic rock sites in (a) and (b) Auckland, (c) and (d) Wellington and (e) and (f) Christchurch.....	53
Figure 8.2	Uniform hazard spectra for generic rock sites in (a) and (b) Auckland, (c) and (d) Wellington and (e) and (f) Christchurch.....	54
Figure 9.1	Partially-ergodic hazard results for the WNAS and POTS sites .....	56
Figure 9.2	Partially-ergodic hazard results for the WEMS and VUWS sites .....	57
Figure 9.3	Partially-ergodic hazard results for the TEPS and FKPS sites .....	58

## TABLES

Table 4.1	The multivariate normal parameter distribution for the PGA models .....	9
Table 7.1	Example “weights on weights” used to calculate hazard results.....	50

## APPENDICES

### APPENDIX 1 WEIGHT CALCULATIONS FOR THE AUCKLAND-SPECIFIC MODELS..71

## APPENDIX FIGURES

Figure A1.1	Weights for the Auckland suite of PGV models for 0.1 probability of exceedance in 50 years ..	71
Figure A1.2	Weights for the Auckland suite of PGA models for 0.1 probability of exceedance in 50 years ..	72

Figure A1.3	Weights for the Auckland suite of SA(0.01 s) models for 0.1 probability of exceedance in 50 years.....	73
Figure A1.4	Weights for the Auckland suite of SA(0.02 s) models for 0.1 probability of exceedance in 50 years.....	74
Figure A1.5	Weights for the Auckland suite of SA(0.03 s) models for 0.1 probability of exceedance in 50 years.....	75
Figure A1.6	Weights for the Auckland suite of SA(0.05 s) models for 0.1 probability of exceedance in 50 years.....	76
Figure A1.7	Weights for the Auckland suite of SA(0.075 s) models for 0.1 probability of exceedance in 50 years.....	77
Figure A1.8	Weights for the Auckland suite of SA(0.1 s) models for 0.1 probability of exceedance in 50 years.....	78
Figure A1.9	Weights for the Auckland suite of SA(0.2 s) models for 0.1 probability of exceedance in 50 years.....	79
Figure A1.10	Weights for the Auckland suite of SA(0.3 s) models for 0.1 probability of exceedance in 50 years.....	80
Figure A1.11	Weights for the Auckland suite of SA(0.4 s) models for 0.1 probability of exceedance in 50 years.....	81
Figure A1.12	Weights for the Auckland suite of SA(0.5 s) models for 0.1 probability of exceedance in 50 years.....	82
Figure A1.13	Weights for the Auckland suite of SA(0.75 s) models for 0.1 probability of exceedance in 50 years.....	83
Figure A1.14	Weights for the Auckland suite of SA(1 s) models for 0.1 probability of exceedance in 50 years. ....	84
Figure A1.15	Weights for the Auckland suite of SA(1.5 s) models for 0.1 probability of exceedance in 50 years.....	85
Figure A1.16	Weights for the Auckland suite of SA(2 s) models for 0.1 probability of exceedance in 50 years. ....	86
Figure A1.17	Weights for the Auckland suite of SA(3 s) models for 0.1 probability of exceedance in 50 years. ....	87
Figure A1.18	Weights for the Auckland suite of SA(4 s) models for 0.1 probability of exceedance in 50 years. ....	88
Figure A1.19	Weights for the Auckland suite of SA(5 s) models for 0.1 probability of exceedance in 50 years. ....	89
Figure A1.20	Weights for the Auckland suite of SA(7.5 s) models for 0.1 probability of exceedance in 50 years.....	90
Figure A1.21	Weights for the Auckland suite of SA(10 s) models for 0.1 probability of exceedance in 50 years. ....	91

## **ABSTRACT**

A key aspect of seismic hazard assessment is the prediction of the ground motion distribution from seismic sources. The prediction can either be made using an empirical ground-motion model, sometimes referred to as a ground-motion prediction equation, or using semi-physical, semi-empirical ground-motion simulations. The choice of technique, and model within each technique, often has a very large effect on the results, which renders the final hazard results uncertain. This type of uncertainty is often referred to as epistemic uncertainty. Accounting for epistemic uncertainty involves combining the outputs from all technically defensible models. Seismic hazard assessment in New Zealand has historically suffered from an insufficient availability of technically-defensible models, which has prevented the epistemic uncertainty from being robustly quantified. This study derives preliminary suites of nonredundant median models for shallow crustal earthquakes that are designed to capture the full space of technically defensible models for seismic hazard assessment. With the plausible model space adequately covered, well-performing models based on current evidence can receive higher weights. Preliminary model suites and weights are derived specifically for Auckland, Wellington and Christchurch, as well as a generic model suite for wider application. Ground-motion standard deviation models are derived using New Zealand data, and guided at large magnitudes by global data where the New Zealand dataset is too sparse. Preliminary uniform seismic hazard spectra are calculated using these model suites for rock sites in Auckland, Wellington and Christchurch. Partially-ergodic uniform hazard spectra are also calculated using the model suites for six locations in Wellington.

## **KEYWORDS**

Ground motion; seismic hazard; PGA; ergodic; partially-ergodic; nonergodic; epistemic; aleatory; uncertainty; crustal; subduction; Sammon's map; Royal Commission

This page left intentionally blank.

## 1.0 INTRODUCTION

Probabilistic seismic hazard analysis (PSHA; Cornell, 1968) involves calculating the probability of a certain seismic intensity value being exceeded over a given time period. For a single scenario, this metric is obtained by multiplying the rate of a seismic source rupturing in the given time period by the probability that the seismic source will generate seismic intensities that exceed the given seismic intensity value. The overall seismic hazard is obtained by summing this function over all seismic sources in the vicinity of a given location.

To determine the conditional probability density function of seismic intensity for a given moment magnitude ( $M_w$ ) and distance scenario, it is common to use an empirical ground-motion model. Such empirical models are statistical representations of recorded and/or simulated ground-motion data, and hundreds of these empirical models have been derived since the PSHA method was first proposed, for various regions around the world (Douglas, 2003; Douglas and Edwards, 2016).

The seismic intensity metrics that are most commonly used by engineering communities are peak ground acceleration (PGA), peak ground velocity (PGV) and 5%-damped pseudo-acceleration elastic response spectra (from which pseudo-velocity and pseudo-displacement response spectra are easily obtained). Modern empirical ground-motion models provide conditional distributions for most or all of these seismic intensity metrics. Other values of damping are also of increasing interest, for which damping modification models are applied to 5%-damped response spectral models.

An issue with empirical models is that different models often provide markedly different conditional distributions for a given source-site scenario, yielding substantially different hazard results. Generally, there is insufficient available data to identify the best model through model testing. Without relevant test data, many models provide plausible distributions and must be considered. The uncertainty that results from between-model variations is known as 'epistemic uncertainty', referring to our lack of knowledge. In the context of ground-motion characterisation for PSHA, the term 'epistemic' is usually reserved for uncertainty in the median of the empirical ground-motion model, and the shape of the probability density function is referred to as 'aleatory uncertainty', referring to underlying randomness. In many cases, this is an imperfect, reductive partitioning of poorly-quantified and truly stochastic processes but is nevertheless a convenient scheme for quantifying and propagating uncertainty.

Epistemic uncertainty is usually accounted for by using multiple models in a logic tree, with weights assigned to each branch. While the importance of treating ground-motion uncertainties in a logic tree has been known for decades, in New Zealand, consideration of uncertainty has been scarce (see review in Van Houtte, 2017a). The issue was highlighted during an international review of New Zealand's National Seismic Hazard Model (NSHM; Stirling et al. 2012) during the Canterbury Earthquakes Royal Commission of Inquiry (Abrahamson, 2011), which stated that

*"... the ground motion model is often one of the largest sources of uncertainty in seismic hazard studies ... the NSHM ground motion model should be changed to include additional GMPEs considered applicable to New Zealand."*

It is not straightforward to address the concerns raised in the Royal Commission of Inquiry. While there have been hundreds of empirical models previously derived, generally there are

very few that would be suitable for application in New Zealand, for example because they are derived only with small magnitude data, or with data from a tectonic environment that doesn't exist in New Zealand. Additionally, the logic tree framework for considering epistemic uncertainty treats the model weights as model probabilities, which requires the models to be mutually exclusive and collectively exhaustive. Bommer and Scherbaum (2008) describe how models are rarely mutually exclusive, as they are derived with overlapping datasets, and because models are being weighted rather than outputs, redundant model predictions often bias the logic tree weights. Satisfying the collectively exhaustive criterion is also difficult, because the 'true model' may lie outside the range of published models.

The approach in this study hopes to mitigate these issues by deriving a suite of models that are closer to mutually exclusive and collectively exhaustive than currently. This study's method for addressing these issues relies on a key assumption. Most empirical ground-motion models utilise similar equations but are fitted to different datasets and thus have different model parameters. This motivates an assumption that all models can be represented with a single equation but with different parameters. By fitting existing models to this common form, a distribution of plausible model parameters, as indicated by the publication record, can be calculated. Sampling from this distribution allows many new models to be generated, which provide median ground-motion predictions between those of the published models, and beyond what has been published. The sampled ground-motion model distributions can then be analysed in the ground-motion space rather than the model space, to select unique, nonredundant models that approach being mutually exclusive and collectively exhaustive.

The procedure can be summarised in five steps:

1. Select an initial suite of ground-motion models, known as 'seed models'.
2. Select a model form that is a good representation of all of the seed models and fit all of the seed models to this form. This procedure yields a suite of models with the same form, but different model parameters.
3. Fit the suite of model parameters with a multivariate normal distribution, to define a continuous space of ground-motion models. Sample new models from this distribution to interpolate between and extrapolate beyond the ground-motions predicted by the seed models.
4. From the sampled models, visualise the relevant ground motions predicted by the models rather than the models themselves, then select a well-balanced suite of models that cover the full space of epistemic ground-motion uncertainty to be considered.
5. Assign weights to the selected models.

This procedure has been utilised in a handful of overseas hazard assessments (e.g. Chiou, 2015; Kuehn and Abrahamson, 2015; Phung et al. 2019), but is still somewhat of a nascent approach. For the NGA-East project in the United States, a slightly different approach was adopted for steps 2 and 3, where instead of deriving a common-form model with a multivariate normal parameter distribution, a covariance model is derived for ground motions from the seed models, calculated for a range of magnitude, distance and intensity measure scenarios. This covariance model can then be assigned to each seed model to sample new models (Goulet et al. 2018). The approach outlined in steps 1–5 above was preferred for this study, for simplicity. This study represents a pilot study that only derives a preliminary suite of models, but eventually, final versions of these models aim to satisfy the concerns raised in the Canterbury Earthquakes Royal Commission of Inquiry.

The framework provided by this procedure allows for convenient updating of hazard models in the future, as new information can be incorporated into hazard assessment simply by adjusting model weights. The five-step procedure only derives median models, and to allow the models to be used in hazard analyses, standard deviation models are required to predict a conditional ground-motion distribution for PSHA. This study also derives a set of standard deviation models to be used in concert with the median models.

This study is focussed solely on epistemic uncertainty in the median ground motion for shallow crustal events in active seismic regions. Epistemic uncertainty in ground-motion prediction from subduction interface earthquakes is one of the most critical issues in seismic hazard currently. The Hikurangi subduction is currently modelled in the NSHM as  $M_w$ 8.1,  $M_w$ 8.3 and  $M_w$ 9 events but currently only the Abrahamson et al. 2016 (and its interim update in 2018) model considers data from the recent  $M_w > 8.3$  subduction interface events from the last decade. Most subduction interface models have few, if any, data available in the magnitude range of interest for predicting Hikurangi ground-motion distributions. This study initially attempted to derive a suite of models for both crustal and subduction interface events, but there were too few published models to fit a meaningful the multivariate normal distribution of model parameters (step 3 above). It is anticipated that a new suite of subduction interface models will shortly become available from the NGA-Sub project (Kishida et al. 2018) after which the procedure in this study can potentially be adapted for Hikurangi subduction zone sources.

In this report, a selection of crustal models that are appropriate for three of New Zealand's major centres, Auckland, Wellington and Christchurch, are derived, as well as a suite of models suitable for wider application. The model suites are used to calculate the ground-motion hazard using the 2010 NSHM source model, and the adaption of the Canterbury Seismic Hazard Model (CSHM; Gerstenberger et al. 2014; 2016) source model developed in Van Houtte and Abbott (2019). The models are defined for PGV, PGA and 5%-damped pseudo-spectral acceleration (SA) between oscillator periods of 0.01 and 10 s.

## 2.0 SEED MODEL SELECTION

The initial suite of starting models or ‘seed models’ define the model parameter space, which will in turn define the considered ground-motion space. The seed models are selected from the OpenQuake Engine’s *gsim* library (Pagani et al. 2014; Silva et al. 2014). To be considered for selection in this study, a set of criteria were defined that a model needed to meet to become a seed model. Any selected model must be flagged in OpenQuake as verified, non-experimental, defined for a tectonic region of ‘Active Shallow Crust’, be well-fit by the selected common functional form, and have physically-plausible behaviour over the desired magnitude and distance range.

For New Zealand seismic hazard analysis, the magnitude range of interest for crustal faults is  $5 \leq M_W \leq 8.2$ , and the maximum considered source-to-site distance ( $R_{RUP}$ ) is 200 km. Currently in the published National Seismic Hazard Model (Stirling et al. 2012) and Canterbury Seismic Hazard Model (Gerstenberger et al. 2014; Van Houtte and Abbott 2019),  $M_W 8.2$  corresponds to the largest crustal fault sources, the Alpine Fault and Wairarapa-Nicholson Fault. Any considered ground-motion models must have technically defensible predictions for sources of this magnitude. Examples of models that were excluded from consideration for New Zealand seismic hazard applications are:

- Cauzzi et al. (2014) model, for which peak ground motions significantly over-saturate with magnitude (i.e. the predicted ground-motions decrease as  $M_W$  increases)
- Kotha et al. (2016) model, where at some periods, the second partial derivative of SA with respect to magnitude becomes positive for  $M_W > 7$ , which was not justified by their data (no events had  $M_W > 7$ )
- McVerry et al. (2006), which appears to greatly over-predict  $M_W < 6$  events (e.g. Bradley, 2013; Gerstenberger et al. 2014; Van Houtte, 2017a), and thus its inclusion might unjustifiably skew the parameter distribution of any common form model.

Other models, like Morikawa and Fujiwara (2013) and Zhao et al. (2016b) were excluded because they are poorly fit by the common functional form. Further investigation is necessary to determine the reasons for the poor fit, and to develop mitigation measures. The selected seed models selected are shown in Figure 2.1. The ground motion intensity measures used for this study are PGV, PGA and pseudo-spectral accelerations of SDOF oscillators, with natural periods up to 10 s. Not all seed models provide predictions for all intensity measures, and Figure 2.1 demonstrates that for some periods, particularly long oscillator periods, there are fewer available seed models.

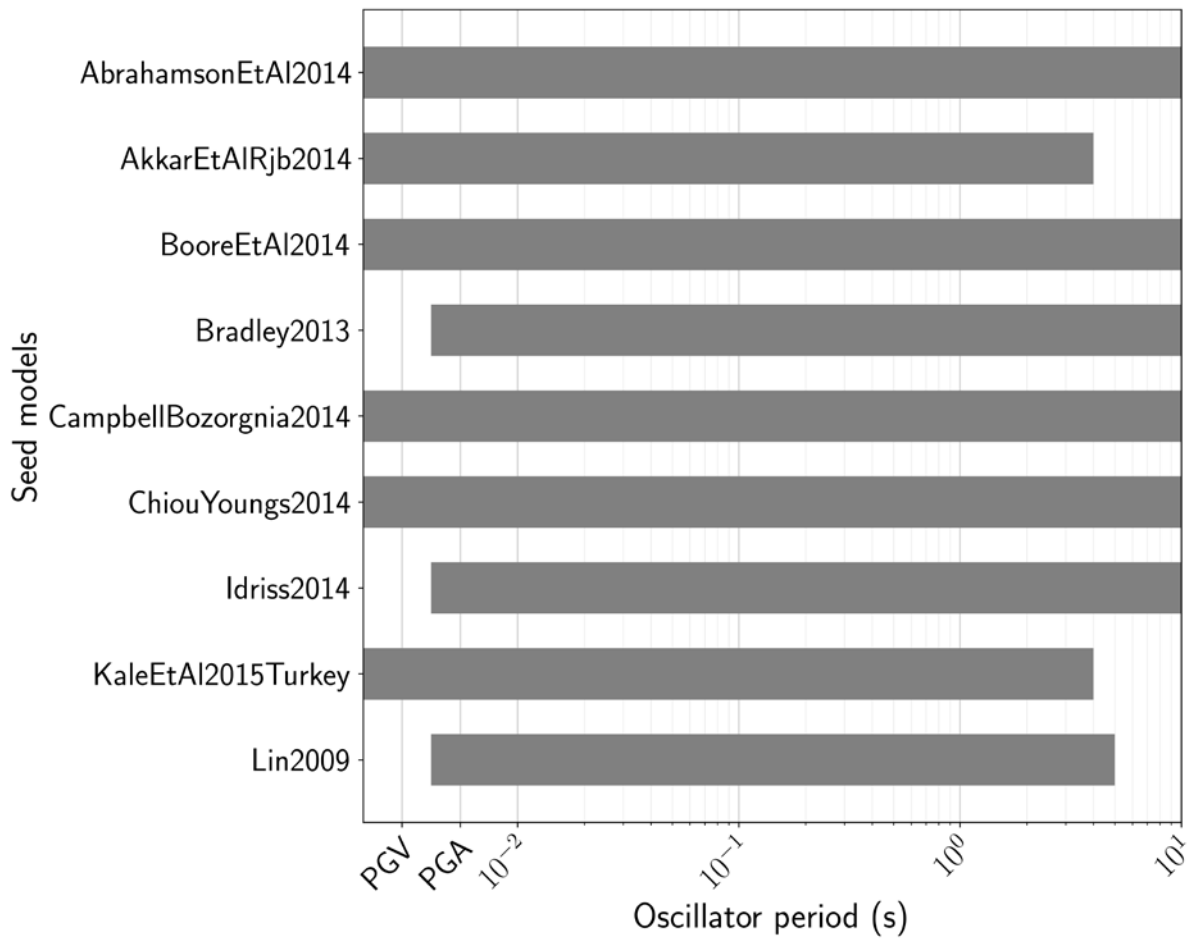


Figure 2.1 The selected seed models where grey bars represent the range of intensity measures that are predicted by each model.

### 3.0 FITTING MODELS TO COMMON FORM

The selected seed models are fit to the following equation (referred to the common-form equation or common-form model):

$$\ln Y = \theta_0 + \theta_1(M_W - 5) + f_M + (\theta_4 + \theta_5(M_W - 5)) \ln \sqrt{(R_{rup}^2 + \theta_6^2)} + \theta_7 R_{rup} + \theta_8 Z_{TOR} + \theta_9 F_{rev} + \theta_{10} F_{nm} + f_{HW} + f_{site}$$

$$f_M = \begin{cases} \theta_2(M_W - 5.5); & \text{for } 5.5 \leq M_W < M_{c2} \\ \theta_2(M_W - M_{c2}) + \theta_3(M_W - M_{c2}); & M_W \geq M_{c2} \end{cases} \quad (3.1)$$

where  $\ln Y$  is the natural logarithm of a given seismic intensity measure,  $M_W$  is the moment magnitude,  $f_M$  represents a trilinear magnitude scaling function,  $R_{rup}$  is the closest distance from a recording location to the fault,  $Z_{TOR}$  is the depth to top of rupture (km),  $F_{rev}$  is a reverse faulting flag (equal to 1 for a reverse fault, zero otherwise) and  $F_{nm}$  is a normal faulting flag,  $f_{HW}$  is a hanging wall model and  $f_{site}$  is a soil response model. The  $\theta$  represent free parameters and include the second hinge magnitude of the trilinear magnitude scaling function,  $M_{c2}$ . Hanging wall and soil response models cannot easily be fit with a common function, so for the purposes of fitting the models to the common form, these terms are fixed to equal the models from the Abrahamson et al. (2014) model. Equations with different magnitude scaling were trialed, but equation (3.1) consistently provided the best fit to the seed models.

To fit the seed models to this form, a set of rupture scenarios to consider are defined:

- Magnitudes between  $M_W 5$  and  $M_W 8.2$  at 0.2 magnitude increments
- Three rake values of -90, 0 and 90 degrees, with respective dip angles of 45, 90 and 45 degrees.
- Three depth values of 0, 5 and 12 km

As the hanging wall term of the common form model is fixed, a set of locations are defined on the footwall, with ten log-spaced Joyner-Boore distances (closest distance to the surface projection of a rupture,  $R_{JB}$ ) between 1 km and 100 km, as well as two additional large-distance  $R_{JB}$  values equal to 150 and 200 km. The models are fit to a reference rock condition with time-averaged shear-wave velocity in the top 30 m,  $V_{S30}$ , equal to 1000 m/s. Accompanying depths to shear-wave velocity horizons of 1 and 2.5 km/s, ( $Z_1$  and  $Z_{2.5}$ ) are 10 m and 0.4 km respectively.

Median predictions are obtained for these scenarios from each seed model. As the Abrahamson et al. (2014)  $f_{site}$  model is non-zero for these site parameters, the predictions for each model are corrected by the  $f_{site}$  model before fitting the parameters, to ensure consistency in later calculations. The free parameters in the common form model in equation (3.1) are fit to each seed model using nonlinear least squares. Starting parameters for each seed model fit are the parameters that best-fit all of the seed models concurrently, as these are better identified than those for an individual seed model. Example of residuals from fitting the worst-case seed model, the Boore et al. (2014) PGA model, is shown in Figure 3.1. The magnitude and distance scaling of the seed model, and the common-form fit, shown in

Figure 3.2. The predictions of the model can generally be matched by the common-form model within around ~20% as the worst case. Some models are better represented by the common form than others. Figure 3.3 shows that the Lin (2009) model is best fit by the common form at short oscillator periods, and the Campbell and Bozorgnia (2014) model is best fit at long oscillator periods. The two models with the lowest log-likelihoods, Boore et al. (2014) and Akkar et al. (2014), base their distance scaling from the  $R_{JB}$  variable, while the common-form equation bases the distance scaling on  $R_{rup}$ . Regardless, the common form model is still a good representation of the median ground-motions predicted by these models.

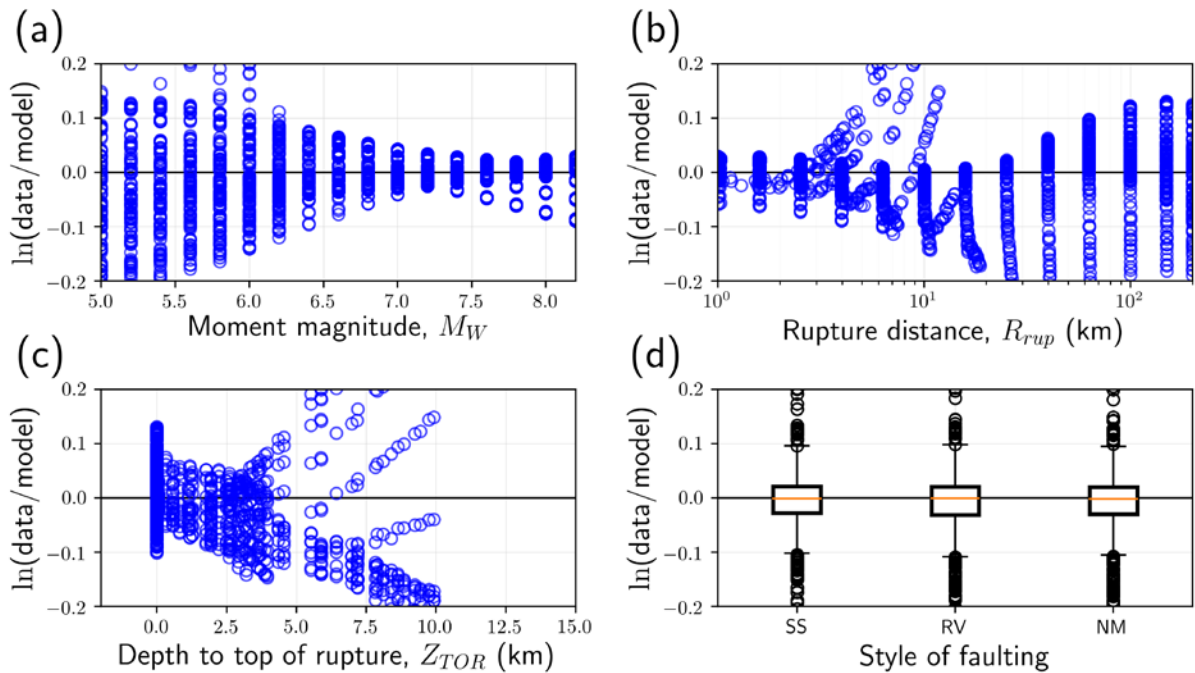


Figure 3.1 PGA residuals from fitting the common-form model to the Boore et al. (2014) model.

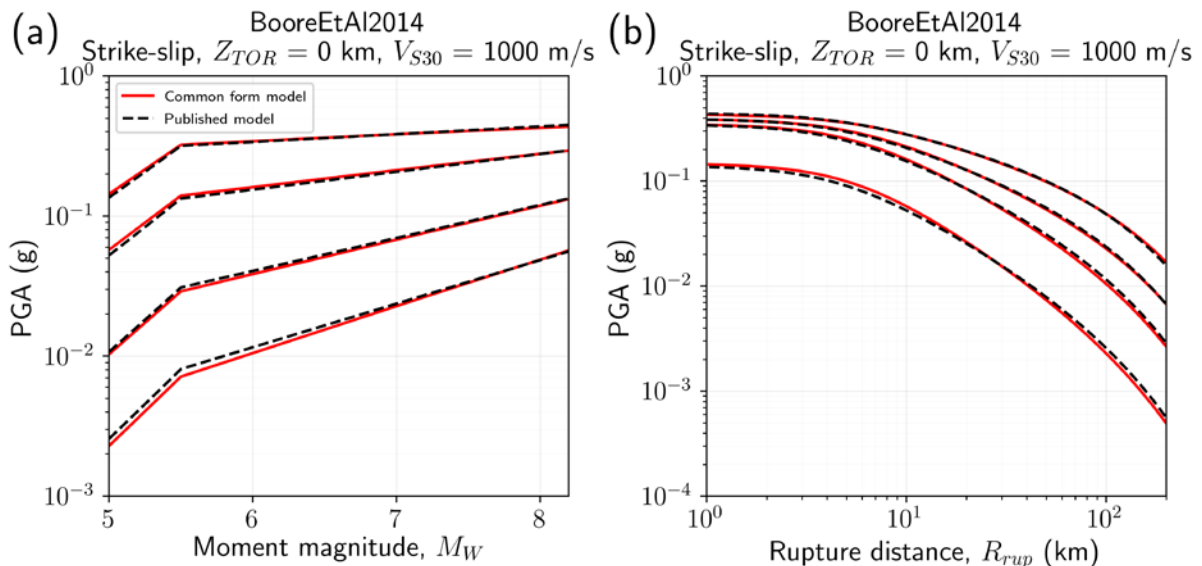


Figure 3.2 (a) Magnitude scaling for  $R_{JB} = 1, 10, 30$  and  $100$  km and (b) distance scaling for  $M_W = 5, 6, 7,$  and  $8$ , for the Boore et al. (2014) model compared to the fitted common-form model. All scenarios are on the footwall.

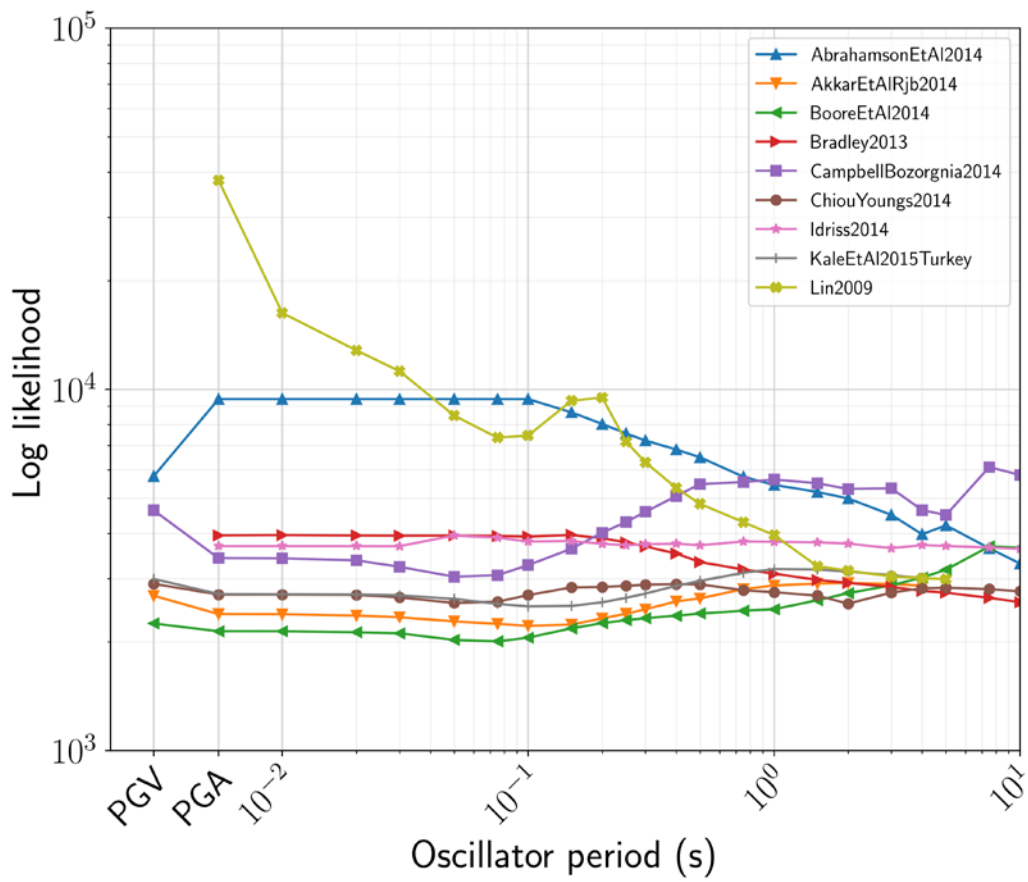


Figure 3.3 The period-dependent log-likelihood of the common-form fit to the seed models.

## 4.0 SAMPLING NEW MODELS

With each of the seed models fit to the common-form equation, we now have a suite of models with the same form but different parameters,  $\theta$ . These parameters are assumed to follow a multivariate normal distribution,

$$\theta \sim \mathcal{N}(\mu_{\theta}, \Sigma_{\theta}) \quad (4.1)$$

where  $\mu_{\theta}$  is the mean of the fitted parameters and  $\Sigma_{\theta}$  represents their covariance.  $\mu_{\theta}$ , and  $\Sigma_{\theta}$  for PGA models are given in Table 4.1. From this continuous parameter distribution, 2000 new models are sampled, but  $\Sigma_{\theta}$  is doubled to ensure the sampled models extrapolate parameters beyond the range of the published seed models. Extrapolating beyond what is published is important to ensure the sampled models are collectively exhaustive. The 2000 sampled parameters are shown in Figure 4.1a. The covariance matrix for the selected, fitted seed models is not positive-definite for any of the seismic intensity measures, and thus the probability density function of the multivariate normal distribution is undefined. The reason for may be because the number of parameters is greater than the number of seed models. To confirm that the sampled parameters are a good representation of the parameter covariance, Figure 4.1b visualises the correlation matrix in a similar form to the sampled parameters and demonstrates that the correlation in the sampled parameters is very similar.

Table 4.1 The multivariate normal parameter distribution for the PGA models.

	$M_{c2}$	$\theta_0$	$\theta_1$	$\theta_2$	$\theta_3$	$\theta_4$	$\theta_5$	$\theta_6$	$\theta_7$	$\theta_8$	$\theta_9$	$\theta_{10}$
	<b>Median</b>											
	6.718	0.765	0.477	-0.371	-0.414	-1.383	0.233	5.61	-0.004	0.031	0.032	-0.175
	<b>Covariance</b>											
$M_{c2}$	0.061	-0.016	0.035	-0.069	0.035	0.006	0.002	0.093	-0.000	0.001	-0.01	0.005
$\theta_0$	-0.016	0.267	-0.12	0.139	-0.059	-0.093	0.005	0.514	-0.001	-0.002	0.013	0.023
$\theta_1$	0.035	-0.12	0.184	-0.214	0.022	0.037	-0.002	-0.012	-0.000	0.001	-0.016	-0.026
$\theta_2$	-0.069	0.139	-0.214	0.29	-0.06	-0.05	-0.003	0.096	0.001	-0.003	-0.018	0.037
$\theta_3$	0.035	-0.059	0.022	-0.06	0.059	0.031	0.000	-0.189	-0.001	0.000	0.000	-0.006
$\theta_4$	0.006	-0.093	0.037	-0.05	0.031	0.037	-0.002	-0.22	-0.001	0.000	-0.003	-0.008
$\theta_5$	0.002	0.006	-0.002	-0.003	0.000	-0.002	0.002	0.001	-0.000	-0.001	-0.000	-0.002
$\theta_6$	0.093	0.514	-0.012	0.096	-0.189	-0.22	0.001	2.26	0.003	-0.004	-0.46	0.107
$\theta_7$	-0.000	0.001	-0.000	0.001	-0.001	-0.001	-0.000	0.003	0.000	-0.000	-0.000	0.000
$\theta_8$	0.001	-0.002	0.001	-0.003	0.000	0.000	0.001	-0.004	-0.000	0.000	-0.000	-0.001
$\theta_9$	-0.01	0.013	-0.016	0.018	0.000	-0.003	-0.000	-0.46	0.000	-0.000	0.006	-0.003
$\theta_{10}$	0.004	0.023	-0.026	0.037	-0.006	-0.008	-0.003	0.207	0.000	-0.002	-0.003	0.019

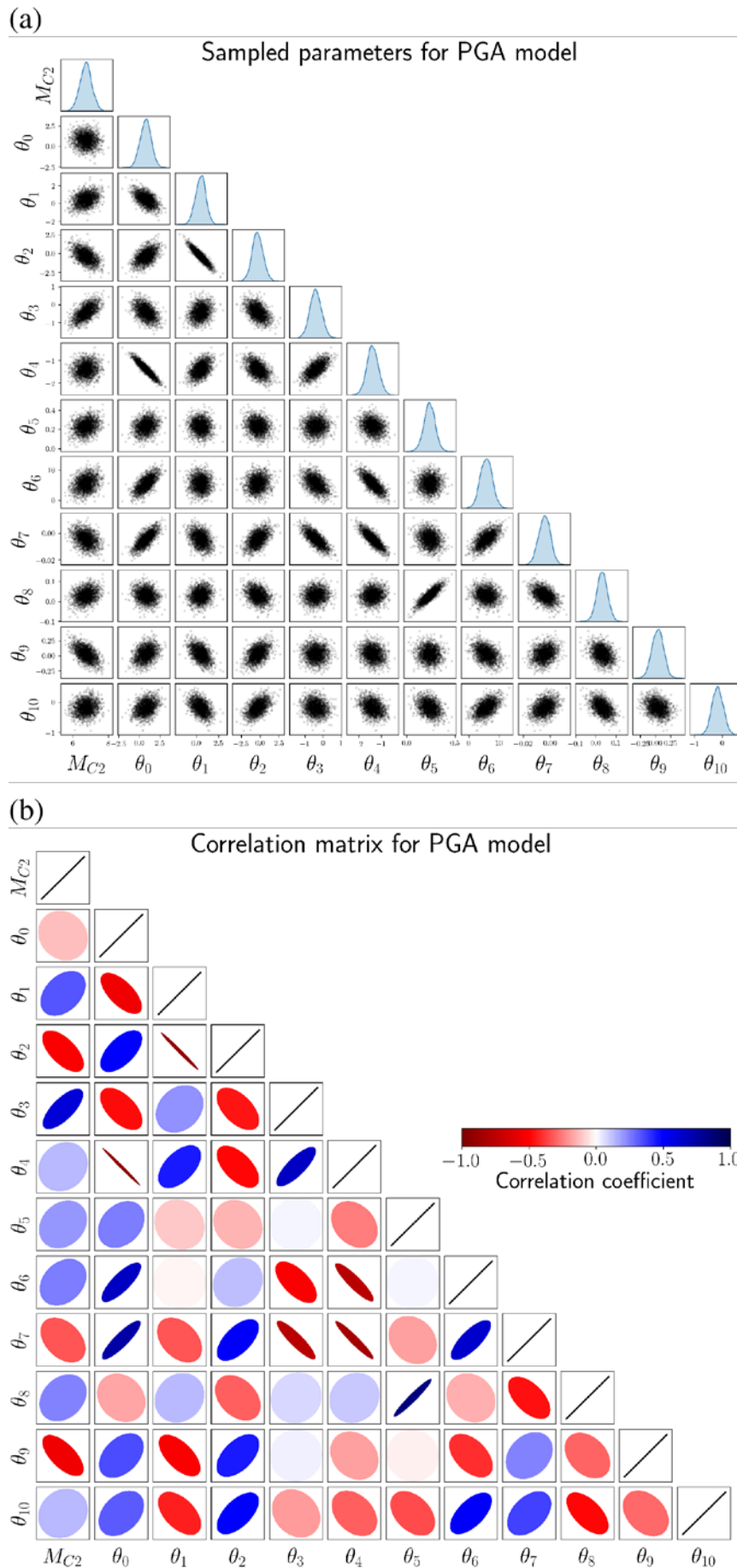


Figure 4.1 (a) The parameters sampled from the multivariate normal distribution, and (b) the correlation matrix from the fitted distribution.

Of the sampled models, some provide implausible predictions. For example, some of the sampled models have median ground motion increasing with distance, which contradicts the well-established theoretical and observed loss of energy to geometric, intrinsic and scattering attenuation of seismic wave amplitudes. Some sampled models also have median ground-motion decreasing as magnitude increases, usually referred to ‘over-saturation with magnitude’. Phung et al. (2019) judged this over-saturation with magnitude effect to be unlikely enough that such models could be excluded from their continuous parameter distribution when sampling ground-motion models.

The physicality of over-saturation with magnitude is unclear and debatable. Schmedes and Archuleta (2008) used simulated ground-motion data to conclude that PGA and PGV from  $M_w > 7$  strike-slip earthquakes saturate in the near-field, but do not over-saturate. Roten et al. (2014) numerically model fault zone plasticity and show that such models dramatically reduce ground-motion in events that generate large strains. The physical parameters that govern the degree of reduction are, however, very poorly constrained. While earthquakes with larger  $M_w$  obviously release more seismic moment, some observations suggest that earthquakes on ‘mature faults’ have lower stress drops and generate lower ground motion than corresponding earthquakes on immature faults (Manighetti et al. 2007; Radiguet et al. 2009). Given that larger-magnitude earthquakes tend to occur on more mature faults, in this author’s opinion the over-saturation with magnitude is not so implausible that it can be excluded, particularly when the goal of this study is to model epistemic uncertainty. Of course, there are limits to the plausibility of magnitude over-saturation. This study allows oversaturation for magnitudes greater than  $M_w 7$ , for oscillator periods less than 1 s, but defines an over-saturation limit of a 10% maximum decrease in peak ground-motions at  $M_w 8.2$ , relative to the prediction at  $M_w = 7$ .

Four separate constraints are applied to the sampled models, these are:

- Models cannot have  $\left. \frac{\partial \ln SA}{\partial R} \right|_{R \leq 100} > 0$ .
- For periods  $< 1$  s, models cannot have  $\left. \frac{\partial \ln SA}{\partial M_w} \right|_{5 \leq M_w \leq 7} < 0$  or  $\frac{SA(M_w = 8.2, R_{rup} < 10)}{SA(M_w = 7.0, R_{rup} < 10)} < 0.9$ , and for periods  $\geq 1$  s, models cannot have  $\left. \frac{\partial \ln SA}{\partial M_w} \right|_{5 \leq M_w \leq 8.2} < 0$ .
- The near-source saturation parameter,  $\theta_6$  must be positive. While a negative value has no influence on the model predictions, as the term is squared,  $\theta_6$  has units of distance so a negative value has no physical meaning.
- At each hinge point, the magnitude scaling gradient is constrained to decrease i.e. both  $\theta_2$  and  $\theta_3$  must be negative, as there is no evidence to suggest that a positive change in gradient is plausible.

Rejected models are resampled to retain a total of 2000 models. The effects of the sampled model constraints are shown in Figure 4.2. At short periods, the magnitude-scaling constraints are the predominant reasons for rejected samples, but at longer periods, the distance constraints cause more samples to be rejected. Figure 4.3 shows how the marginal density kernels for each parameter change with rejected samples. The parameter constraints can be clearly observed in Figure 4.4, where the samples are truncated at zero for  $\theta_2$ ,  $\theta_3$  and  $\theta_6$ . These samples in Figure 4.4 make up the set of candidate models that are analysed further in section

5.0. The magnitude and distance scaling of the 2000 sampled models, relative to the seed models. As intended, the sampled common-form models interpolate between and extrapolate beyond the range of the seed models.

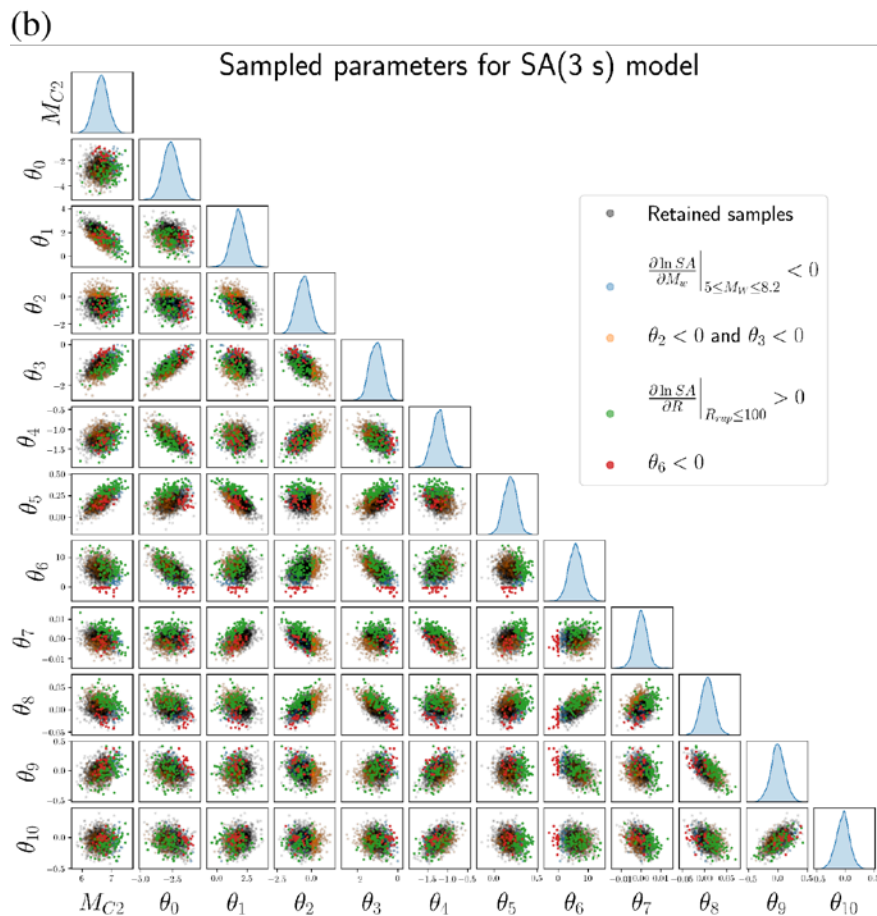
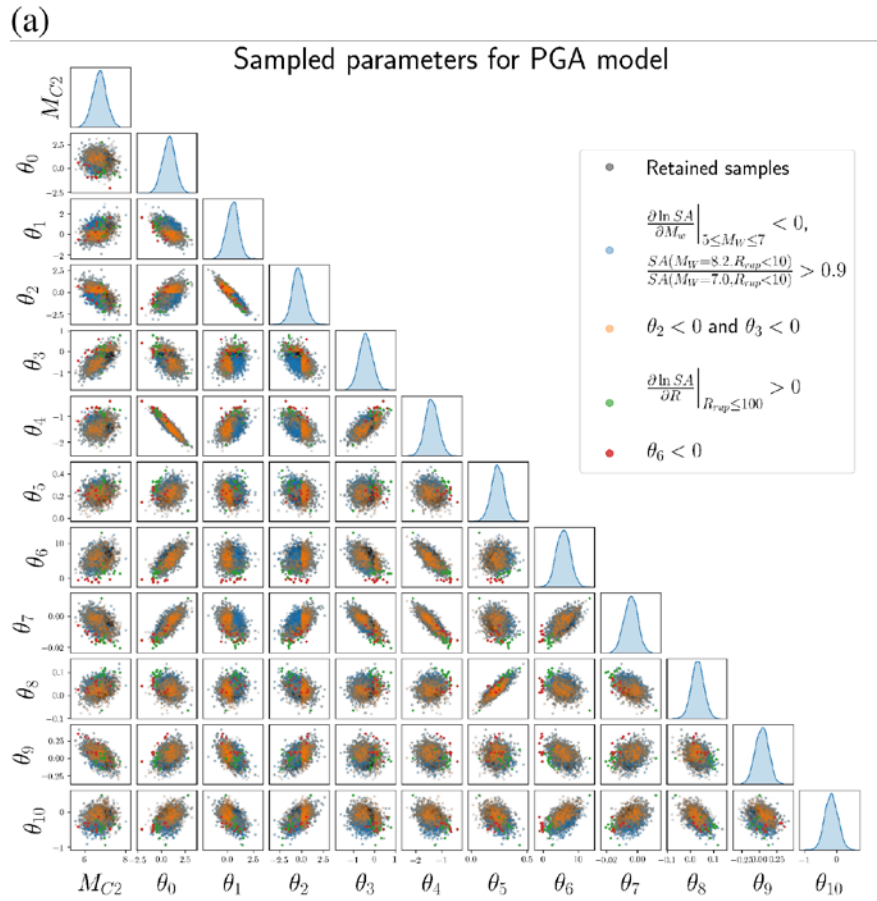


Figure 4.2 The parameters sampled from the multivariate normal distribution that are removed due to the parameter constraints for (a) PGA and (b) SA(3s).

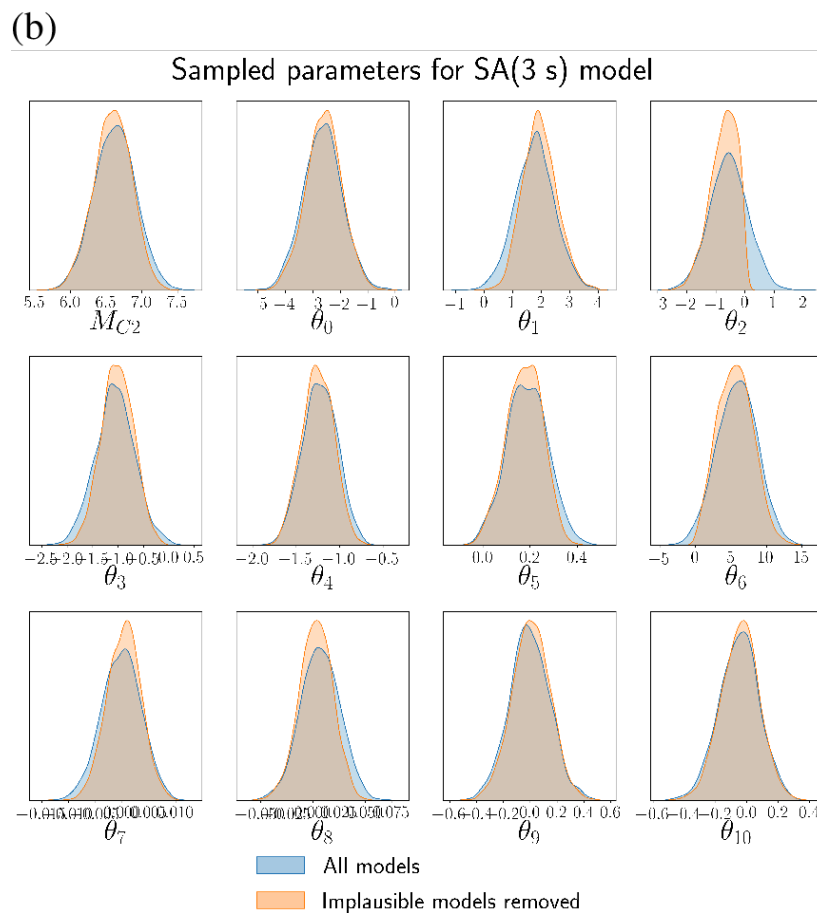
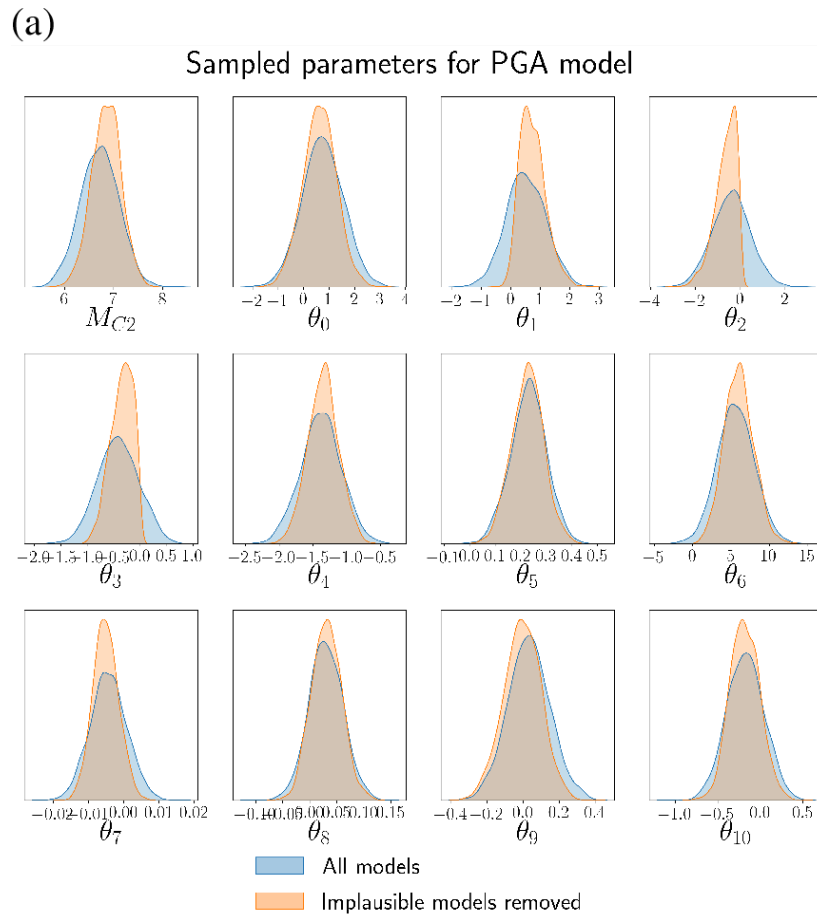


Figure 4.3 Kernel density functions for each parameter before and after removal of implausible models for (a) PGA and (b) SA(3s).

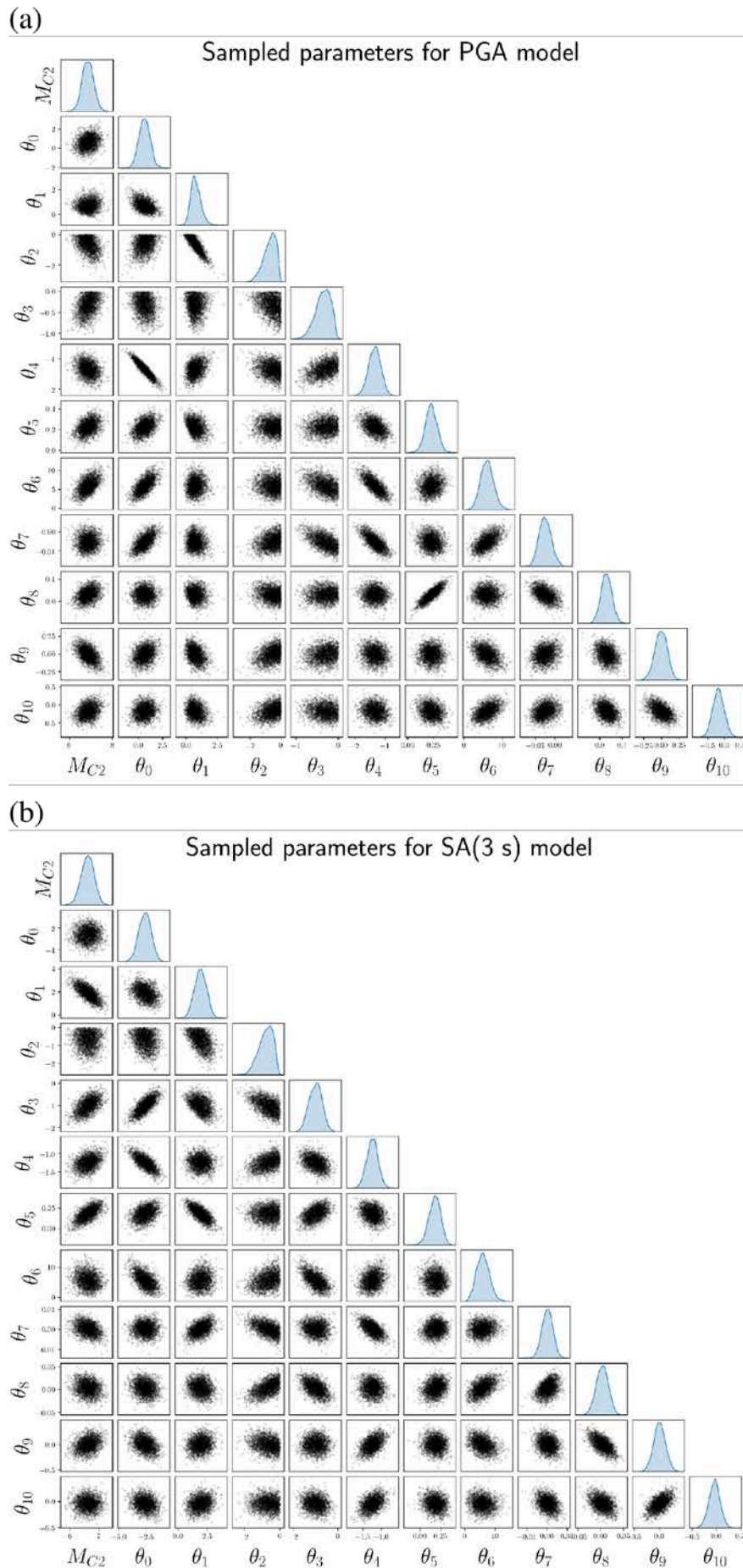


Figure 4.4 The parameter samples after removal of implausible models for (a) PGA and (b) SA(3s).

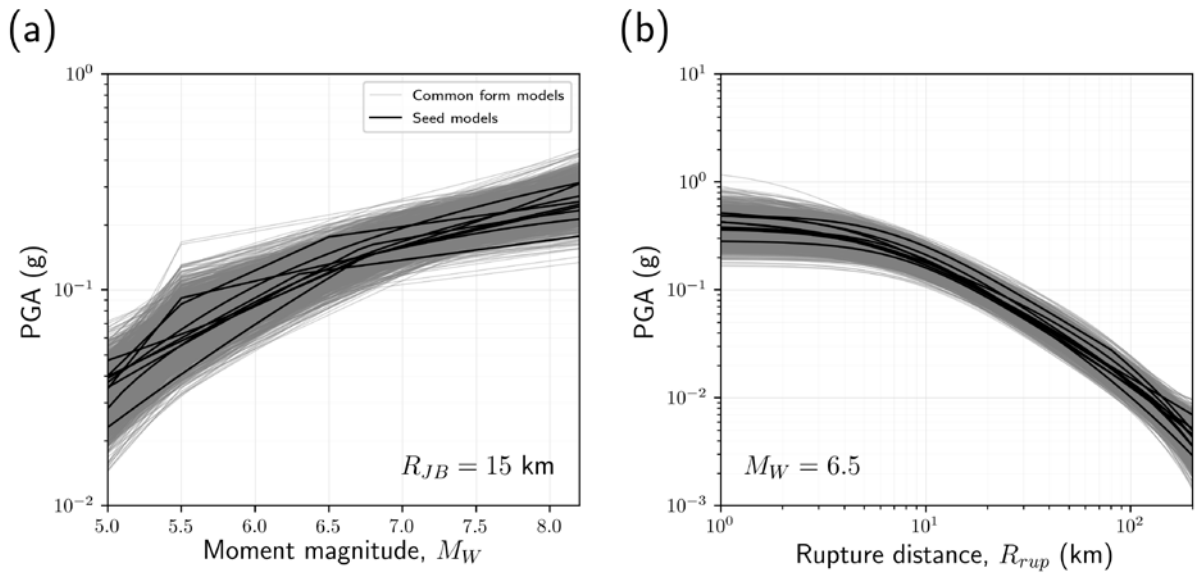


Figure 4.5 (a) Magnitude and (b) distance scaling of PGA for the sampled common-form models, relative to the seed models.

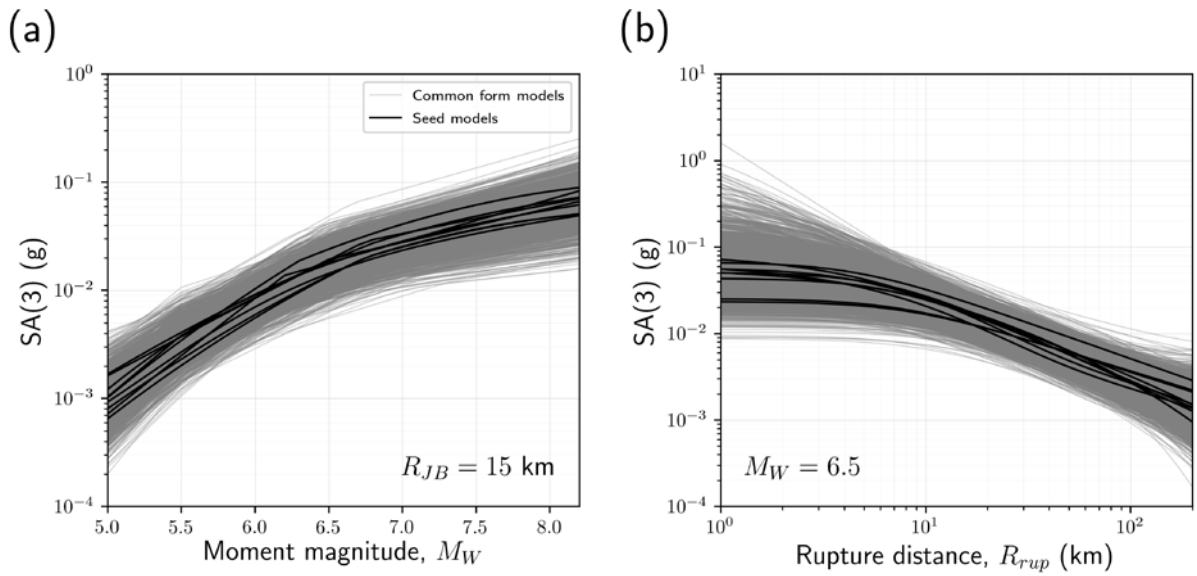


Figure 4.6 (a) Magnitude and (b) distance scaling of SA(3s) for the sampled common-form models, relative to the seed models.

## 5.0 COMMON FORM MODEL SELECTION

By fitting a common-form model to the selected seed models, and sampling new models from an assumed multivariate normal distribution of common-form model parameters, 2000 crustal ground-motion models are now available for seismic hazard analysis. To run 2000 models through hazard calculations is very computationally intensive and is unnecessary because many of these models are redundant. For a given set of scenarios that are relevant for a location's seismic hazard, some of the models will provide a very similar vector of median ground-motion predictions and yield very similar probability of exceedance values. This section focuses on reducing the number of models to a more manageable number that captures a realistic space of epistemic uncertainty.

### 5.1 Visualisation of Models

The relevant scenarios can be substantially different depending on the location. For example, the seismic hazard for locations on the West Coast near the Alpine Fault will be heavily dominated by large-magnitude Alpine Fault events, while the seismic hazard in Northland will be more sensitive to moderate-magnitude earthquake sources. For the West Coast case, the selected common-form models mostly need to represent the epistemic uncertainty in the median model for the Alpine Fault scenario, with other magnitude-distance scenarios contributing little. For the Northland case, the selected models need to represent the epistemic uncertainty for numerous scenarios with different magnitude-distance combinations. If one considers the predicted ground-motion for a magnitude-distance scenario as a dimension, the selected models for Wellington only need to consider a small number of dimensions, but other locations need to consider many dimensions. When the number of dimensions is higher than three, the space of predicted ground motions can no longer be plotted.

To select ground-motion models for a higher-dimensional ground-motion space, it is convenient to reduce the number of dimensions down to two. Dimensionality reduction is a very useful technique for explaining the primary features of higher-dimensional data that lie on a lower-dimensional manifold. In the case of the ground-motion data, it will be demonstrated later that the data often lie on a manifold that is close to a two-dimensional plane. There are many methods of dimensionality reduction, but only two will be discussed in this study, principal component analysis (PCA) and Sammon's mapping (Sammon, 1969; Scherbaum et al. 2010). PCA can be used to transform the higher-dimensional ground-motion data into a set of two orthogonal axes that capture the most variance. The Sammon's mapping algorithm involves calculating the between-sample distances on a two-dimensional plane that best match the between-sample distances in the higher-dimensional space. The between-sample distance calculation can be made in a number of ways, and this study uses the between-sample Euclidean distance as the selected distance metric, for simplicity.

To visualise the ground-motion space that the common form models cover, ground-motions from each model are calculated for the set of magnitude-distance combinations on the footwall, shown in Figure 5.1. Strike-slip, reverse, and normal faulting events are also considered through planar faults with dips of 90, 45 and 45 degrees, and rakes of 0, 90 and -90 degrees respectively. To consider the depth-scaling of the models, two depths are considered, one where all faults rupture the surface, and one where the bottom depth of the fault is fixed to an assumed maximum seismogenic depth of 12 km. Fault planes are simulated using the Stafford (2014b) magnitude scaling relationship, assuming that the faults all have the median rupture width. For the larger magnitude scenarios that rupture the full 12 km seismogenic thickness, the simulated fault planes are identical for the two different depths, but for smaller magnitude

scenarios the depth to top of rupture,  $Z_{TOR}$ , is different. For the 275 magnitude-distance combinations, three different mechanisms and two different depths, a total of 1,650 scenarios are considered. These scenarios correspond to a 1,650-dimensional ground-motion space and are intended to cover the scenarios that are relevant to seismic hazard in New Zealand. This suite of scenarios will also be used to select a suite of widely-applicable models that cover the epistemic ground-motion uncertainty for these particular scenarios.

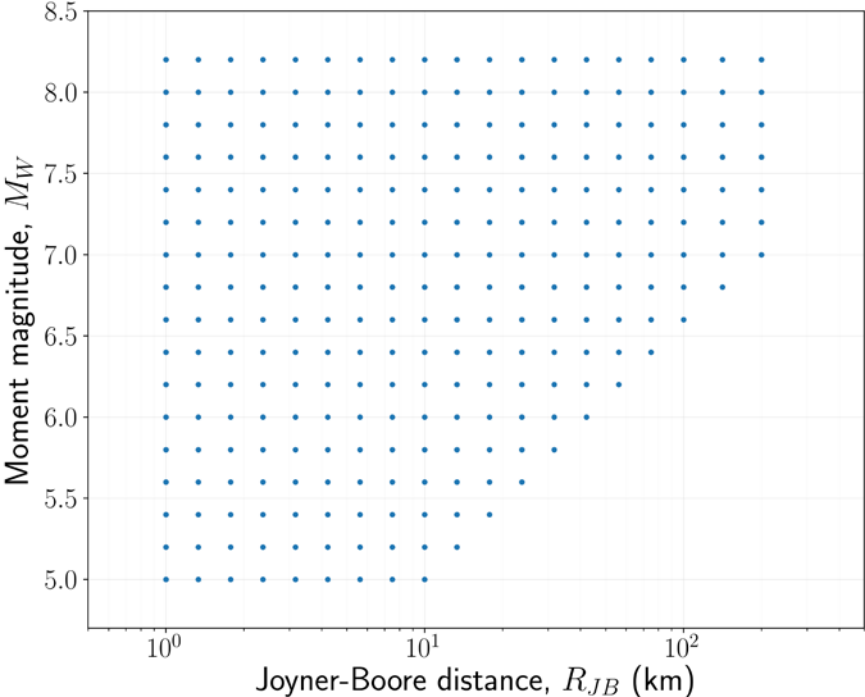


Figure 5.1 Generic suite of scenarios used to select a suite of widely-applicable ground-motion models.

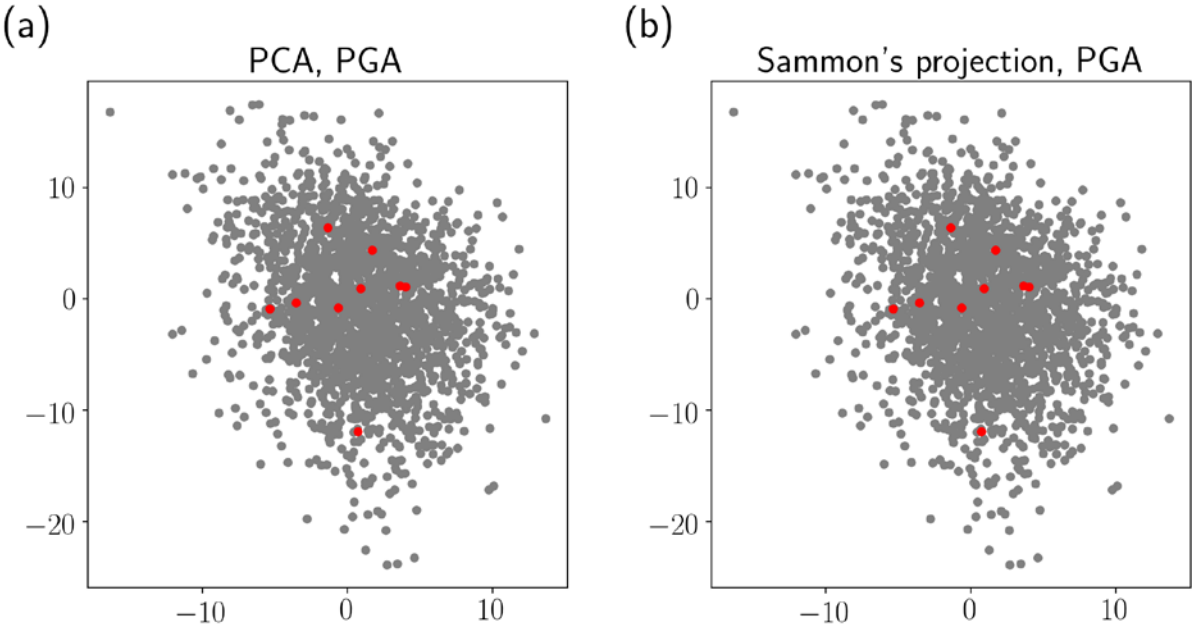


Figure 5.2 The higher-dimensional PGA ground-motion space for the generic suite of scenarios, projected onto two dimensions using (a) principal component analysis and (b) Sammon's mapping. The predictions from the seed models are in red, and the 2000 common form models are in grey. Vertical axis approximately represents the change in average  $\ln(SA)$ .

Figure 5.2 shows the 1,650-dimensional space for the natural logarithm of PGA, for all of the common-form and seed models, projected onto (a) the first two principal components and (b) a Sammon's map. Points that lie close together on these plots represent models that provide similar ground-motion predictions for the 1,650 scenarios. In this case, the two methods of dimensionality reduction provide a nearly-identical projection. For the remainder of this report, Sammon's maps are used hereafter for all dimensionality reduction calculations, as many people find these plots slightly simpler to interpret. No units are given for the PCA or Sammon's map plots. To help interpret the units of the Sammon's maps, Figure 5.3 shows the Euclidean distances of each common-form model to the mean prediction in the 1,650-dimensional space, for two different ground-motion intensity measures, PGA and SA(3 s). If the contours in Figure 5.3 are a perfect circle, then the points in the 1,650-dimensional space lie on a two-dimensional plane. For PGA, there is some variability about a two-dimensional plane, but the data are still well-represented in two dimensions. For SA(3 s), the data lie on a manifold that is very close to a plane. In the case of SA(3 s), the two-dimensional distance matrix is almost identical to the Euclidean distance matrix in 1,650 dimensions. This means that the units of the Sammon's map are the same as the input data, which in this case are  $\ln$  units. For the PGA map, the units are more an approximation of  $\ln$  units than pure  $\ln$  units and have more meaning locally than globally.

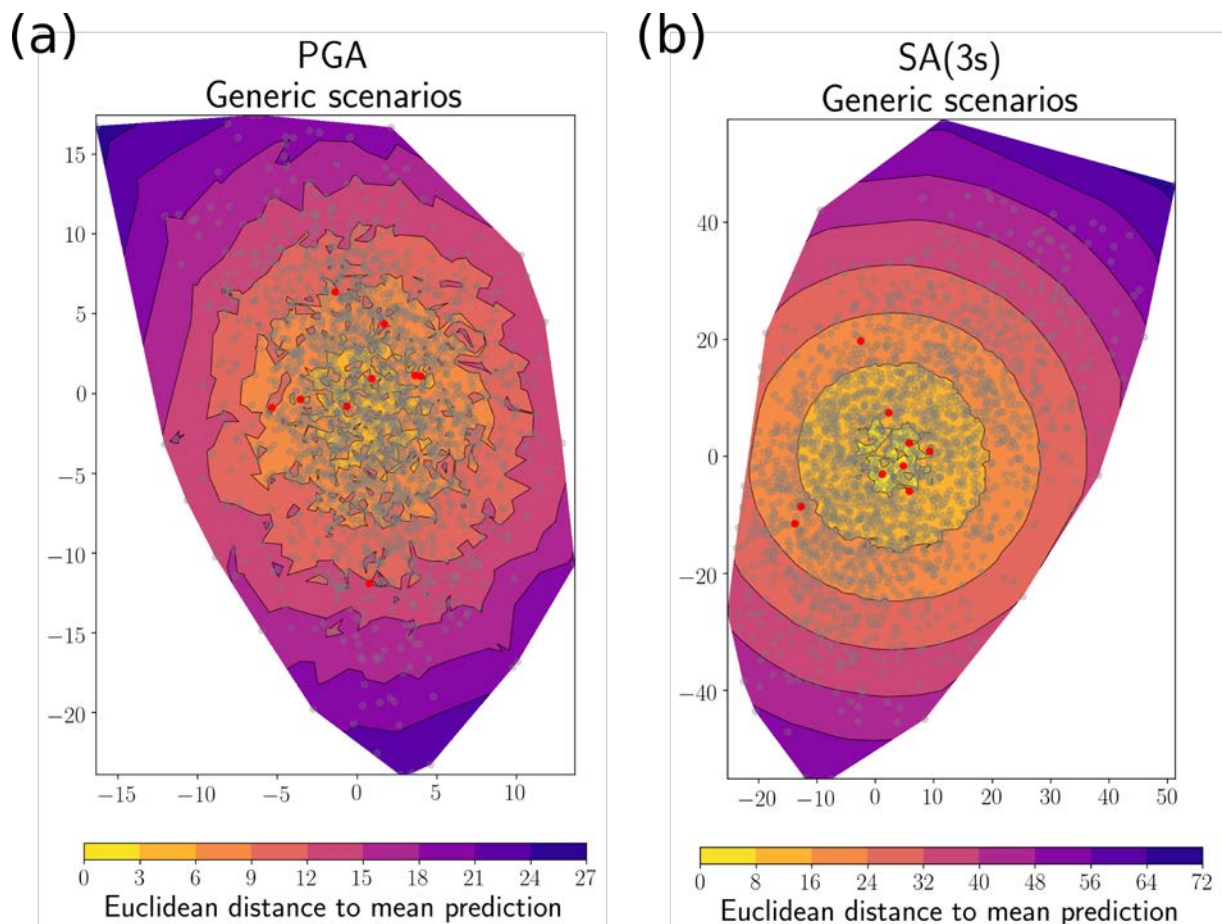


Figure 5.3 The Euclidean distance of the model to the central model prediction, projected onto two dimensions using Sammon's algorithm for (a) PGA and (b) SA(3 s). Red circles represent the seed models. A perfect circle represents model predictions lying on two-dimensional plane in the higher-dimensional space.

While Figure 5.1, Figure 5.2 and Figure 5.3 demonstrate a projection for a wide range of scenarios, for many locations in New Zealand, the seismic hazard is controlled by far fewer scenarios. For example, Figure 5.4 shows the disaggregated PGA hazard for shallow crustal

events in Auckland, Wellington and Christchurch, corresponding to a 10% probability of exceedance in 50 years. The Auckland and Wellington results are calculated using the 2010 National Seismic Hazard Model (Stirling et al. 2012) seismic source model, while the Christchurch results are calculated using the source model from the OpenQuake implementation of the Canterbury Seismic Hazard Model (Gerstenberger et al. 2014; 2016; Van Houtte and Abbott, 2019). The ground-motion logic tree for the disaggregation calculation uses the seed models, including scaled 'upper' and 'lower' versions, where the median models are scaled up and down by the Al Atik and Youngs (2014) epistemic uncertainty model, as would be typical in a PSHA study. For these source models, ground-motion models and this probability of exceedance, the modelled PGA hazard from shallow crustal earthquakes near Auckland is much more influenced by moderate magnitude earthquakes than Wellington, which is only sensitive to a small number of scenarios, most notably the Wellington Fault scenario. Christchurch is roughly equally sensitive to a range of different magnitudes between  $M_w5.5$  and  $M_w7.5$ , but predominantly near-field scenarios.

Figure 5.5 shows the predictions from the seed and common form models, projected onto Sammon's maps, for Auckland, Wellington and Christchurch, for the scenarios that contribute to the PGA hazard with 10% probability of exceedance. The predictions are weighted by their contribution to the hazard, so the Sammon's map units in Figure 5.5 do not correspond to ln units. For each location, different models will be in close proximity to one another. For example, nearby models for the Wellington case will provide similar median PGAs for the  $M_w7.5$ , short distance scenario, but will not necessarily provide similar median PGAs for the smaller magnitude scenarios that underly the projection for Auckland. Selecting models for each location for the specific scenarios relevant to that location will provide a better estimate of the epistemic ground-motion uncertainty at that location.

With fewer scenarios, the location-specific  $n$ -dimensional spaces tend to be better represented by a plane than the projection for the 1,650-dimensional space of generic scenarios. Figure 5.6 shows the amount of variance of the  $n$ -dimensional space explained by the first two principal components. For the city-specific scenarios based on the weighted disaggregation scenarios, the explained variance is always greater than 90%. For the generic scenarios, the explained variance ranges from around 65-90%. Given that the PGA data for the 1,650-dimensional space of generic scenarios has the lowest explained variance, the projection shown in Figure 5.3a can be considered a worst case.

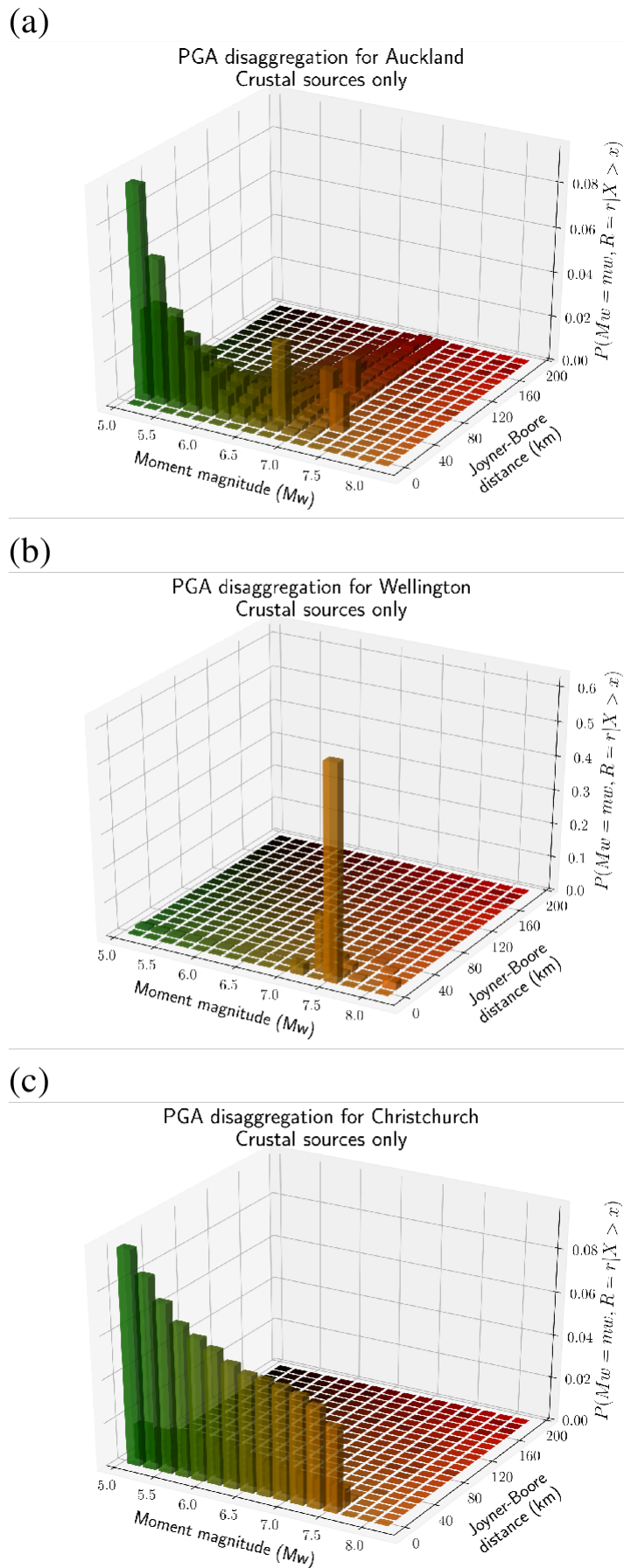


Figure 5.4 Disaggregation of the PGA hazard at 0.1 probability of exceedance in 50 years, using equally-weighted seed models for the ground-motion models for (a) Auckland, (b) Wellington and (c) Christchurch.

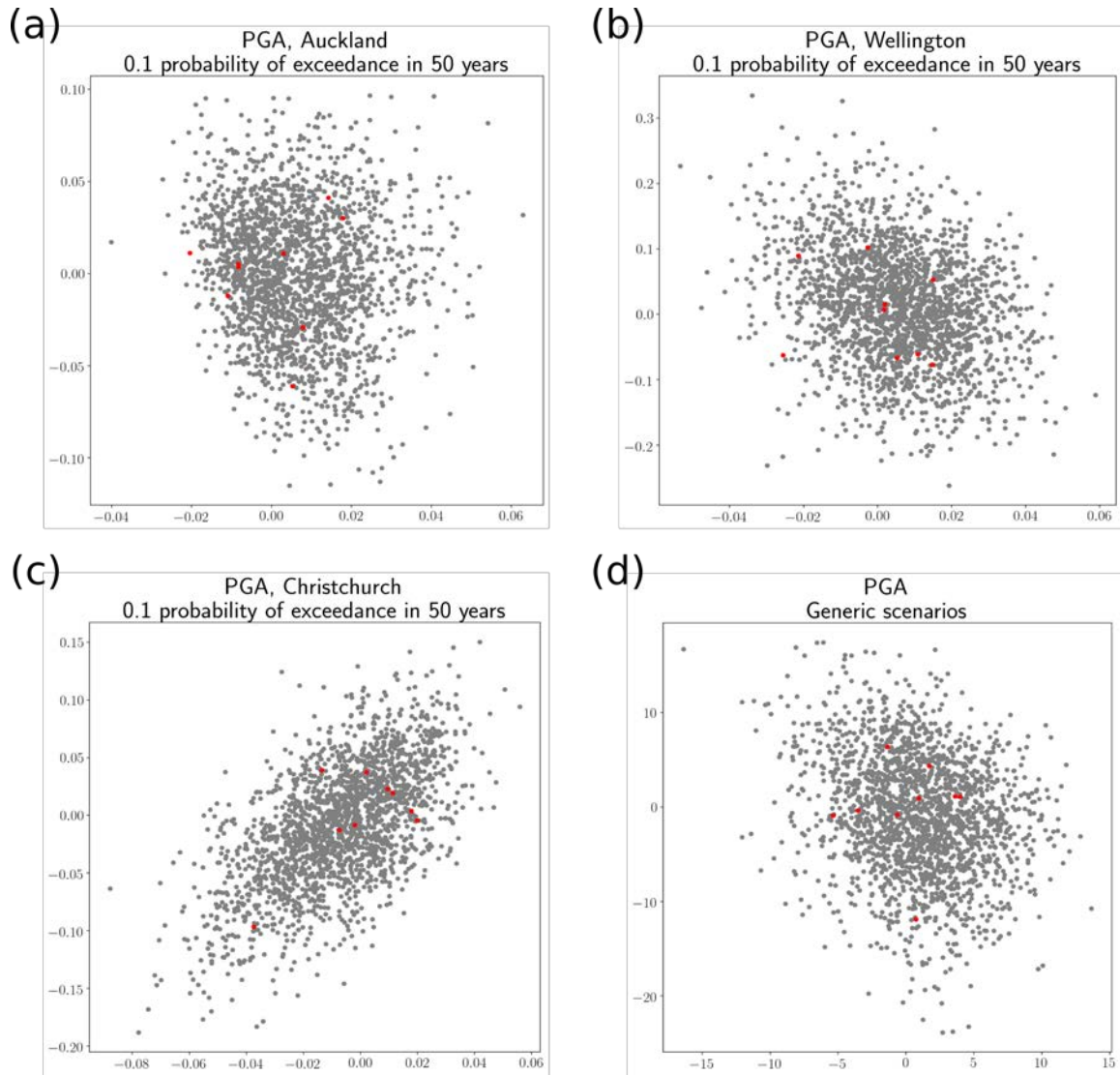


Figure 5.5 Two dimensional Sammon's map for the weighted scenarios from the PGA disaggregation, for (a) Auckland, (b) Wellington, (c) Christchurch and (d) the generic, unweighted suite of scenarios. Vertical axis approximately represents the change in average  $\ln(SA)$ . Red points represent the seed models.

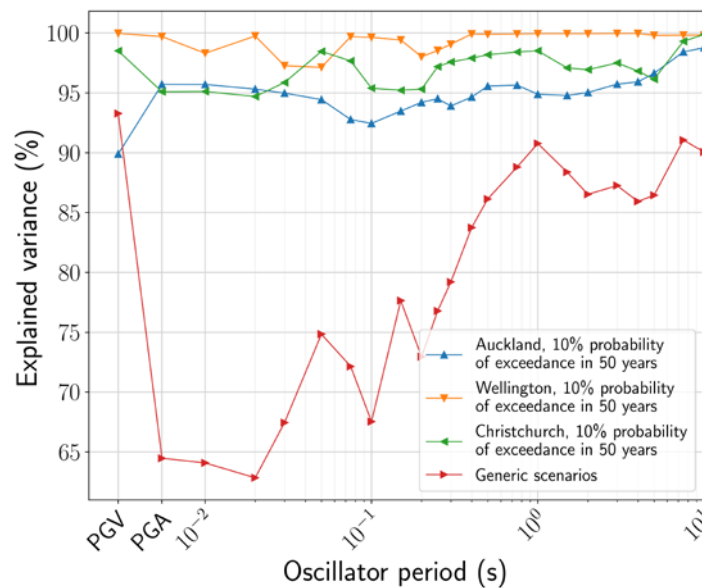


Figure 5.6 Variance explained by the first two principal components for the disaggregation-weighted scenarios at Auckland, Wellington, Christchurch, and the generic scenarios.

## 5.2 Selection Procedure

Given that the Sammon's maps are a good representation of the higher-dimensional ground-motion space, they form a good basis for model selection. There is little advantage to selecting two models located nearby on a Sammon's map, as one of the two will provide redundant predictions. It is instead desirable to obtain models that represent technically-defensible regions of models on the Sammon's map, where the region is considered technically defensible.

Selecting the models from the map can be done in numerous ways. This study adopts the following procedure, guided by the work of Phung et al. (2019):

- Scale the seed models up and down by 1.96x the Al Atik and Youngs (2014) epistemic uncertainty standard deviation model,  $1.96\sigma_{AY14}$ , which quantifies the uncertainty in the NGA-West2 median models from the parameter standard errors. The factor of 1.96 defines 95% confidence intervals of a standard normal distribution.
- Fit an ellipse to the convex hull of the scaled seed models.
- If the ellipse falls outside an outer polygon, defined as the convex hull of all sampled common-form models, then the major axis of the ellipse is scaled down such that the ellipse falls inside this outer hull. This constraint is to prevent unreasonable ground-motion spaces being considered.
- Scale the ellipse by factors of 0.4, 0.8 and 1.2, then subdivide the outer two regions defined by these ellipses in 45 degree increments from the major axis of the ellipse.
- Select the model in the centroid of each region, defining a total of 17 models.

In a single isolated case, the best-fit ellipse to the convex hull was degenerate. This issue was mitigated by fitting an ellipse to the points representing the convex hull, along with the closest point to the edge of the polygon that defines the convex hull, i.e. an additional point to better constrain the ellipse.

The procedure typically aligns the major axis of the ellipse close to vertical, i.e. a scaling up and down of the median model predictions, with the minor axis capturing differences in magnitude and distance scaling. This procedure differs slightly from the procedure undertaken in Phung et al. (2019), who instead placed more emphasis on aligning the major axis of the ellipse more with difference in the slopes of the magnitude scaling. An example of the model selection procedure is shown in Figure 5.7. Figure 5.8 shows the magnitude and distance scaling of the selected models relative to the common-form models.

For SA(3s) in Figure 5.7c, the ellipse-fitting procedure results in a space that is not overly consistent with the underpinning seed models. While this inconsistency can be accounted for later in model weighting, alternative procedures for selecting the models from the Sammon's projection need to be considered before the selected models can be finalised for application.

Another issue with this procedure is that implausible models were already removed in Section 4.0, this procedure represents a second reduction in the range of considered models for PSHA. The primary justification for this reduction is to define the 'technically-defensible' regions as those covered by published models in the literature. There are innumerable alternative selection procedures that could have been used to discretise the ground-motion space, and these need to be further investigated in a sensitivity study.

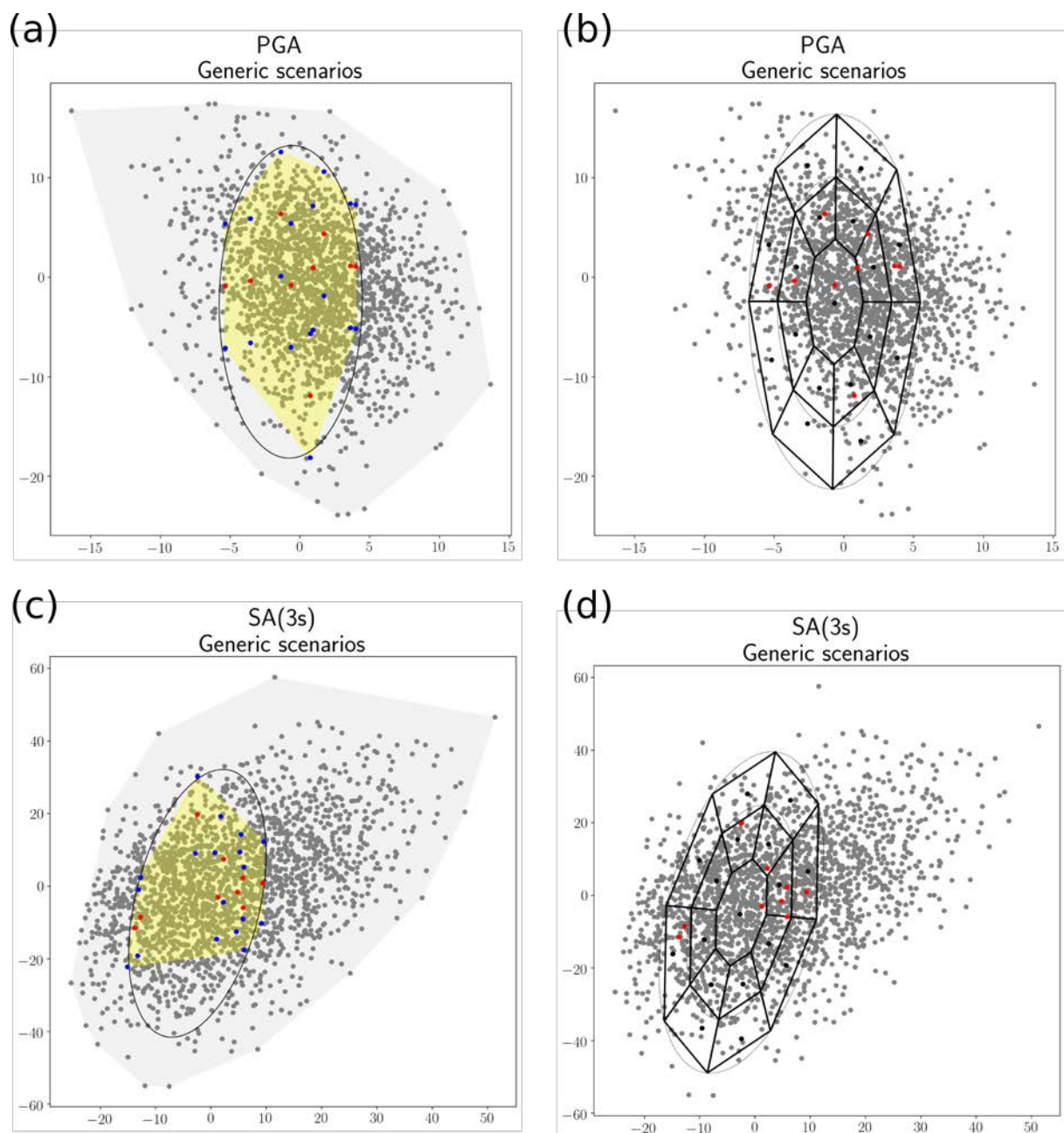


Figure 5.7 Workflow for selecting a representative suite of models from the Sammon's map. For PGA and SA(3s) and the generic suite of scenarios, (a) and (c) respectively show the seed models (in red) are scaled up and down by  $1.96\sigma_{AY2014}$  from the Al Atik and Youngs (2014) epistemic uncertainty model (blue points). An ellipse is fit to the convex hull of the scaled seed models (yellow polygon), but the major axis of the ellipse is scaled down if it falls outside the outer hull (light grey polygon). For the same PGA and SA(3s) scenarios, (b) and (d) respectively show seventeen polygons defined by scaling the ellipse in (a) scaled by 0.4, 0.8 and 1.2, then defining trapezia by subdividing the ellipses in 45-degree increments. The selected models (black dots) are those closest to the polygon centroid.

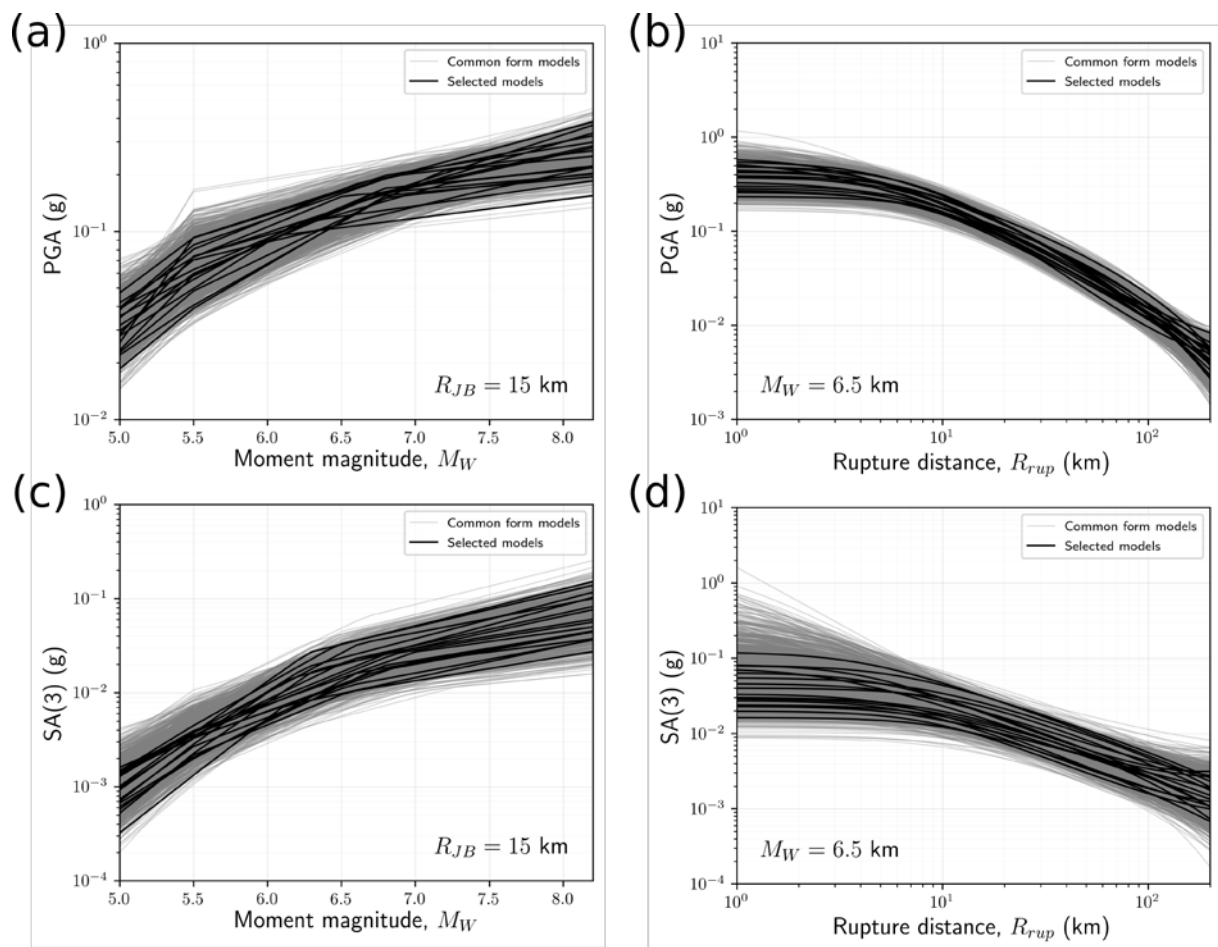


Figure 5.8 The (a) magnitude and (b) distance scaling of the selected PGA models, and (c) magnitude and (d) distance scaling of the selected SA(3s) models from Figure 5.7, relative to all of the sampled common-form models.

## 6.0 STANDARD DEVIATION MODELS

### 6.1 Components of Ground-Motion Standard Deviation

The median models derived in this study are intended to collectively represent the epistemic uncertainty in the median prediction. In PSHA, the aleatory component of the ground-motion variability is typically accounted for using the within-model uncertainty, defined by the residual standard deviation. The procedure thus far only involves analysis of published median models, and thus none of the selected models have accompanying standard deviation models. Standard deviation models must be derived before the suite of median models can be used in PSHA.

Standard deviation models are derived by analysing the components of ground-motion residuals. In a traditional “random-effects” ground-motion model, the total model residuals ( $\epsilon$ ) are composed of:

$$\epsilon = \delta B_e + \delta W_e \quad (6.1)$$

where  $\delta B_e$  represents the between-event residual and  $\delta W_e$  represents the within-event residual for event  $e$ . The standard deviations of  $\delta B_e$  and  $\delta W_e$  are known as  $\tau$  and  $\phi$  respectively, and the total variance ( $\tau^2 + \phi^2$ ) is defined as  $\sigma^2$ . By modelling the aleatory variability using  $\tau$ ,  $\phi$  and  $\sigma$ , one is implicitly making an ergodic assumption i.e. the variability in space is the same as the variability in time at a single site. For PSHA at a single site, the ergodic assumption is generally considered by most researchers to overestimate the aleatory variability (Anderson and Brune, 1999)

In a hierarchical model that also analyses station-to-station effects,  $\delta W_e$  is decomposed further such that

$$\epsilon = \delta B_e + \delta W S_{e_s} + \delta S_2 S_s \quad (6.2)$$

where  $\delta S_2 S_s$  is the between-station residual and  $\delta W S_{e_s}$  is the single-station within-event residual at station  $s$ . The standard deviations of  $\delta S_2 S_s$  and  $\delta W S_{e_s}$  are referred to as  $\phi_{S_2 S}$  and  $\phi_{SS}$  respectively. In PSHA, one can partially remove an aspect of the ergodic assumption by using the so-called ‘single-station sigma’,  $\sigma_{SS}$ , to represent the aleatory variability (Atkinson, 2006; Al Atik et al. 2010),

$$\sigma_{SS} = \sqrt{\tau^2 + \phi_{SS}^2} \quad (6.3)$$

Using  $\sigma_{SS}$  to represent the ground-motion variability represents a reduction in aleatory variability compared to the ergodic model (sigma). Traditionally, to consider the single-station sigma concept in PSHA, one must have an estimate of  $\delta S_2 S_s$  and the epistemic uncertainty and its calculation and calculate a station-specific  $\phi_{SS}$  at the site in question, solely from recordings at that station. This quantity is known as  $\phi_{SS,S}$  (Rodriguez-Marek et al. 2013; Faccioli et al. 2015). In this framework, the sigma utilised for the hazard calculation is

$$\sigma_{SS,S} = \sqrt{\tau^2 + \phi_{SS,S}^2} \quad (6.4)$$

with  $\delta S2S_s$  and its uncertainty modelled as epistemic uncertainty using a logic tree.

In New Zealand, little attention has been paid to ground-motion variability, and Bradley (2015) represents the only dedicated study, where  $\delta S2S_s$  and  $\sigma_{SS,S}$  terms (among others) were derived for a Canterbury-specific dataset. Van Houtte and Abbott (2019) incorporated minor aspects of this model in partially-ergodic hazard assessment in Christchurch CBD.

Kotha et al. (2017) have questioned the  $\sigma_{SS,S}$  approach, suggesting that  $\phi_{SS,S}$  can often be artificially low in cases where similar source-to-site paths are being sampled, for example when a station records a mainshock-aftershock sequence. This effect would be expected for Wellington stations, for example, where stations have predominantly recorded events from the south in the Cook Strait and Kaikōura earthquake sequences. Kotha et al. (2017) also contend that  $\phi_{SS,S}$  is typically calculated from a small dataset, and may not sample the magnitude and distance scenarios that are of interest for hazard. Instead, those authors suggest  $\sigma_{SS}$  is more appropriate to use for partially-ergodic PSHA instead of  $\sigma_{SS,S}$ .

This author shares the opinions of Kotha et al. (2017). For the common-form models to be used in both ergodic and partially-ergodic PSHA, it is necessary to provide accompanying  $\tau$ ,  $\phi$  and  $\phi_{SS}$  models. To derive these models, the database of New Zealand strong motion compiled in Van Houtte et al. (2017) and Kaiser et al. (2017) is analysed. The results are then placed in the context of global models and inform selection of standard deviation models to accompany the common-form models. To derive the components of ground-motion variability from New Zealand data, it is necessary to have an unbiased ground-motion model of New Zealand data. In this section, a hierarchical model that separates the residuals into between-event, between-station and single-station within-event residuals, is derived from the New Zealand Strong Motion Database. This model is derived with the sole intention of analysing residuals and is not intended for forward use as a median model.

In addition to recommending the use of  $\phi_{SS}$  in partially-ergodic seismic hazard instead of  $\phi_{SS,S}$ , Kotha et al. (2017) also provide a method for hazard analysts to undertake partially-ergodic hazard without having access to the residuals themselves, which relies on a known  $\phi_{S2S}$  model. While  $\phi_{S2S}$  is not necessary to obtain hazard results in this particular study,  $\phi_{S2S}$  results are analysed to allow application of the Kotha et al. (2017) method.

### 6.1.1 Selected Data

The data used to fit the model are all  $M_w \geq 4$  crustal events in the New Zealand Strong Motion Database. Recordings with  $R_{rup} \geq 200$  km are removed, as are recordings that triggered on the S-wave rather than P-wave arrival. The dataset is further reduced such that each event and station have a minimum of three associated recordings, to remove very poorly-constrained  $\delta B_e$  and  $\delta S2S_s$  residuals. We make the assumption that any bias from data censoring, which occurs from applying these criteria, to be minimal. A total of 73 events, 208 stations and 1506 recordings form the selected dataset at PGA, which is shown in Figure 6.1a-c. The available data decrease as oscillator periods increase beyond 1 s, as demonstrated in Figure 6.1d, with longer-period data comprised of fewer, large-magnitude events recorded by relatively more stations. The average horizontal component of ground-motion, using the RotD50 definition (Boore, 2010), is used for the ground-motion data. The underlying data can be found at <https://github.com/GeoNet/data/tree/master/nzsm-d-flatfiles> (last accessed 5 December 2019).

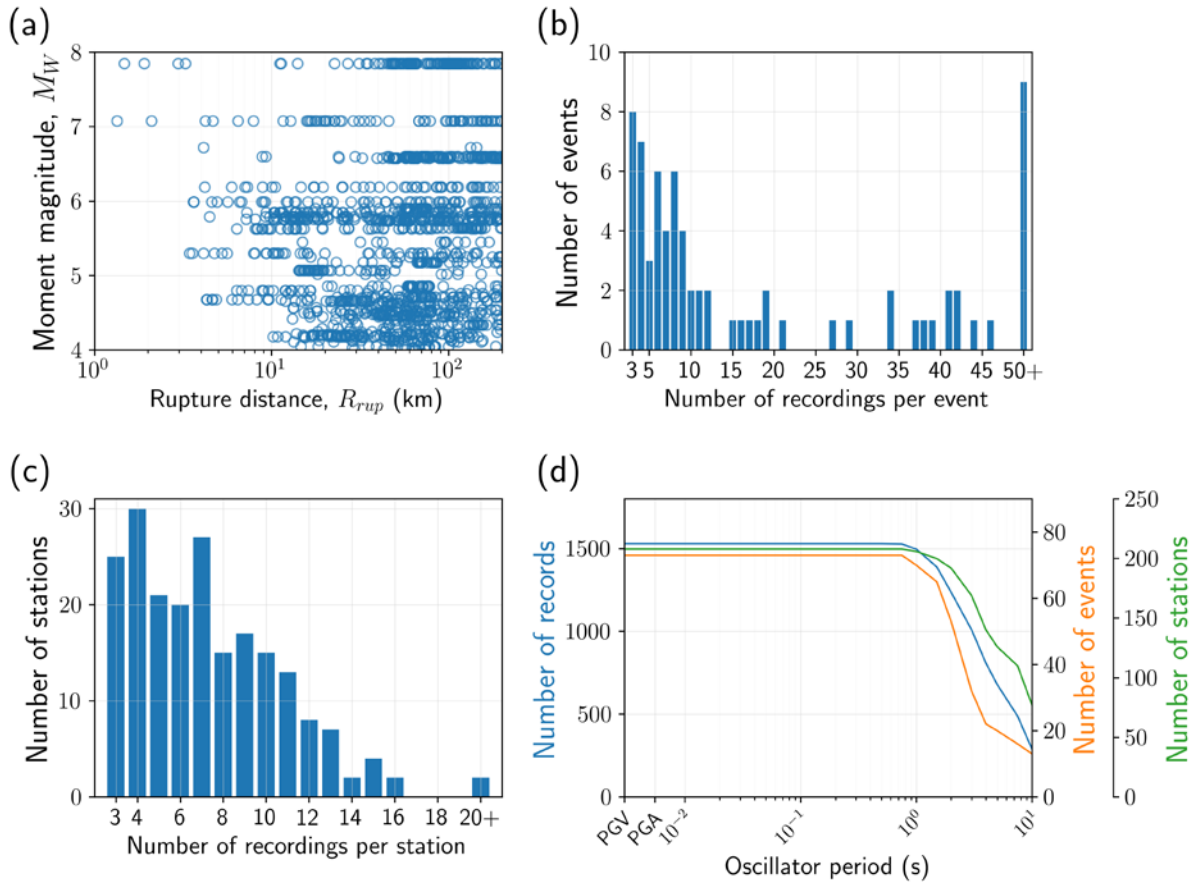


Figure 6.1 The data used to fit the Bayesian hierarchical model. (a) the  $M_W$  -  $R_{rup}$  distribution of available PGA data, (b) the number of events with a given number of recordings for each event, as an illustration of how well-constrained each  $\delta B_e$  is (c) the number of stations with a given number of recordings at each station, as an illustration of how well-constrained each  $\delta S2S_s$  is, and (d) the reduction in available recordings, events and stations with increasing oscillator period.

### 6.1.2 Form of The Model

The model is formulated as

$$\ln Y = f(\mathbf{X}|\boldsymbol{\theta}) + \delta B_e + \delta W S_{es} + \delta S2S_s \quad (6.5)$$

where  $\mathbf{X}$  are the independent variables. The form of  $f(\mathbf{X}|\boldsymbol{\theta})$  is the same as the common-form model in equation (3.1), except the  $M_{c2}$  parameter is fixed to equal 6.75 to aid model convergence where the New Zealand dataset is sparse. The site effects and hanging wall effects terms,  $f_{site}$  and  $f_{HW}$ , are not solved for, and are instead fixed to equal the Abrahamson et al. (2014) site response and hanging wall models. These terms are fixed so that the derived between-station residuals ( $\delta S2S_s$ ) can be applied to the common form models in an internally-consistent manner, in a partially-ergodic PSHA study. As is typical in hierarchical modelling, a normal distribution prior is placed on the event and stations terms where

$$\delta B_e \sim \mathcal{N}(0, \tau) \quad (6.6)$$

$$\delta S2S_s \sim \mathcal{N}(0, \phi_{S2S}) \quad (6.7)$$

The  $\delta W S_{es}$  residuals are assumed to be uncorrelated.

Priors on each parameter in  $\theta$  are defined using the multivariate normal distribution determined in Section 4.0, with each parameter having a prior median value matching the multivariate normal distribution and a prior standard deviation value equal to three times the standard deviation. The only exception was for the short-distance saturation term,  $\theta_6$ , which is poorly constrained by New Zealand data and is instead assigned a prior standard deviation equal to the standard deviation of the multivariate normal distribution. Only the diagonal terms of the covariance matrix in equation (4.1) are utilised for the prior distributions. The  $\tau$ ,  $\phi_{SS}$  and  $\phi_{S2S}$  terms are assigned weakly-informative priors, specifically half-Cauchy distributions with a scale parameter equal to two.

### 6.1.3 Model Fit

The models are defined in the probabilistic programming language Stan (Carpenter et al. 2017), and fit using Hamiltonian Monte Carlo (HMC). For each oscillator period, four independent HMC chains of 1000 samples are modelled, each with 500 warm-up samples and 500 samples of the posterior distributions, to make a total of 2000 posterior samples. Starting values are random. Model convergence is checked through the mixing of the four chains, as defined by the  $\hat{R}$  statistic (Gelman and Rubin, 1992). Convergence is defined as  $0.9 < \hat{R} < 1.1$  for all parameters in the model, including the event and station terms. All models satisfied this criterion.

Model residuals for PGA are shown in Figure 6.2, and the median PGA model's magnitude and distance scaling is shown in Figure 6.3. The most obvious characteristic of these two figures is the model's large overprediction of PGA the Kaikōura earthquake, as well as the underprediction of short-distance recordings. This is a known difficulty from fitting ground-motion models to the New Zealand dataset, which is characterised by moderate magnitude earthquakes,  $M_W \sim 6$ , with large near-source ground motions. The same issue was also encountered in Van Houtte (2017b) when deriving empirical Fourier amplitude spectral and response spectral models, and isn't resolved by allowing  $\theta_6$  to be magnitude-dependent. To ensure this shortcoming doesn't affect the standard deviation results, only events with  $M_W < 7$  are analysed herein, and the  $R_{rup} < 10$  km data are analysed with caution.

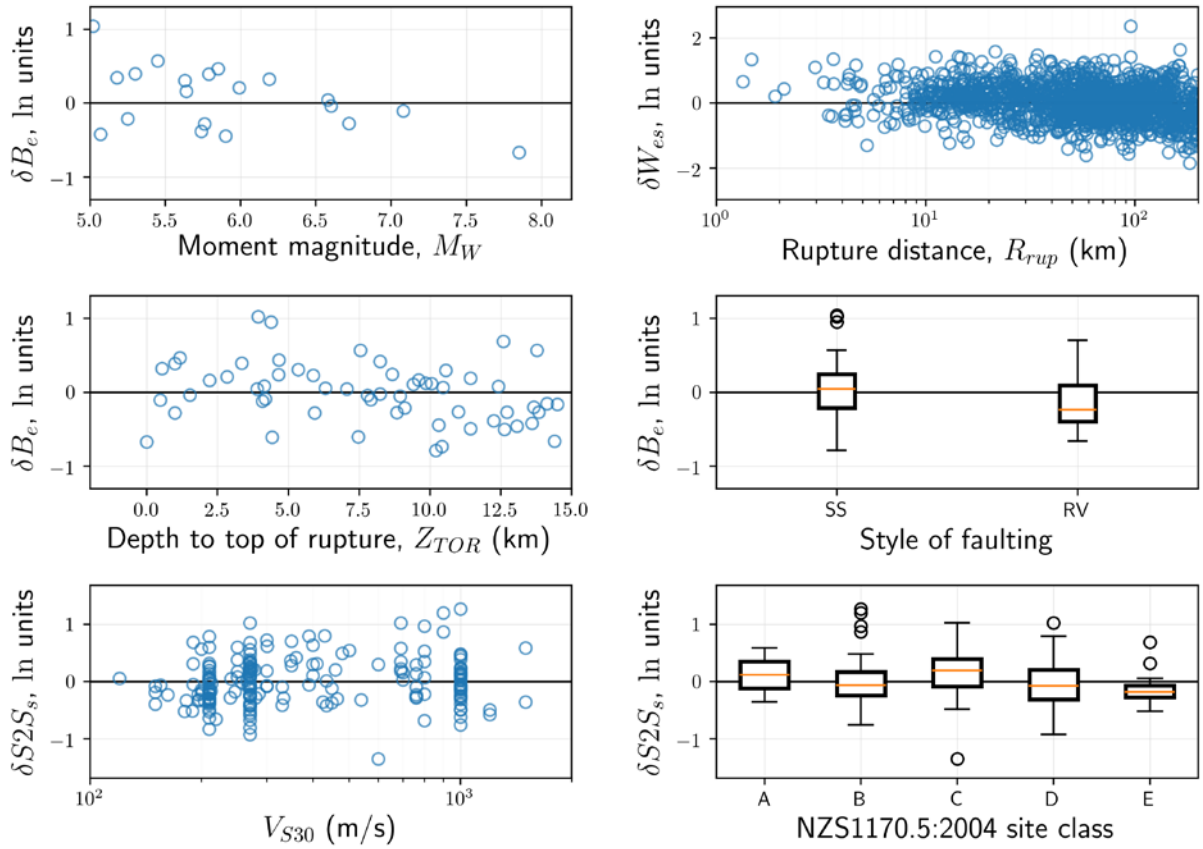


Figure 6.2 Residuals of the model against (a)  $M_W$ , (b)  $R_{rup}$ , (c)  $Z_{TOR}$ , (d) style-of-faulting (note there are no normal faulting events in the dataset), (e)  $V_{S30}$  and (f) NZS1170.5:2004 site classification, for PGA.

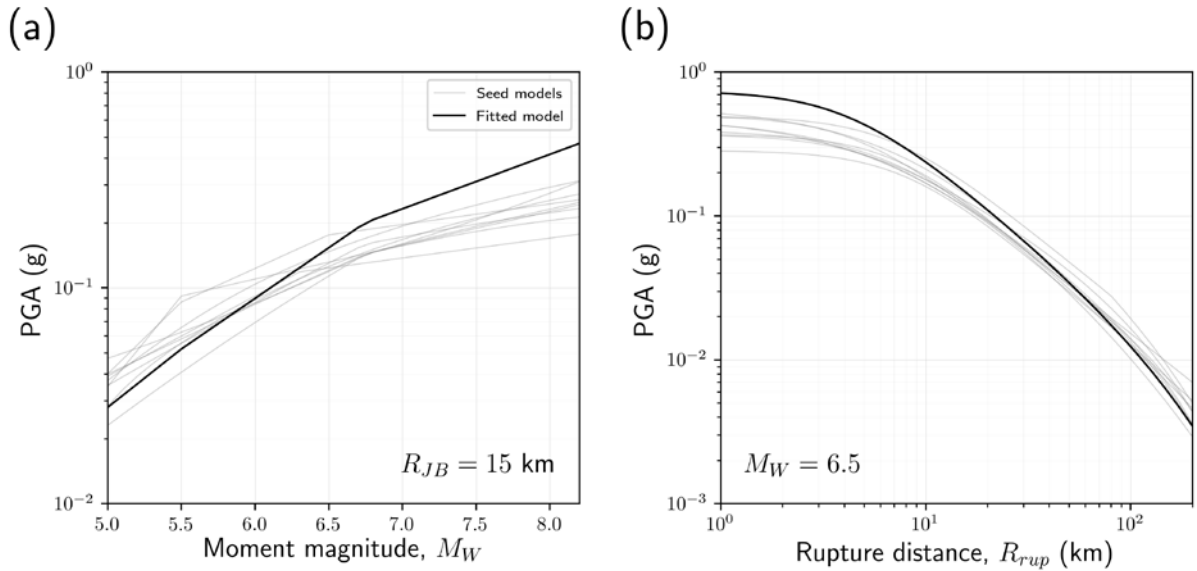


Figure 6.3 (a) the magnitude-dependence and (b) the distance-dependence of the fitted model, compared to the seed models, for PGA.

## 6.2 Standard Deviation Results

The magnitude- and distance-dependence of the residual standard deviation are analysed and compared to those defined by the seed models. Results are only presented for  $M_w \geq 5$ , as this is the minimum magnitude of interest in New Zealand seismic hazard analyses. To calculate the standard deviation in each magnitude or distance bin

$$\tau_b = \sqrt{\frac{\sum_{n=1}^{N_b} \delta B_{e,n}^2}{N_b - 1}} \quad (6.8)$$

where  $N$  is the number of recordings in the  $i$ th bin.  $\phi$  and  $\phi_{ss}$  in each bin are calculated in a similar manner.

Given that there are few available events with  $M_w \geq 5$ , only two magnitude bins are defined, each spanning one magnitude increment between  $M_w$  5 and 7. There are only two events in the New Zealand Strong Motion Database, with  $M_w \geq 7$ , so reliable standard deviation values cannot be determined. Results are presented as the expected value of the standard deviation in each bin, and the 90% credible intervals of the posterior density function.

### 6.2.1 Between-Event Standard Deviation, $\tau$

The magnitude-dependence of  $\tau$  for PGA, SA(0.5s), SA(1s) and SA(3s) is shown in Figure 6.4, and compared against to the  $\tau$  models associated with the seed models, where available. Not all seed models have  $\tau$  models, for example Lin (2009) and Idriss (2014) only provide a total standard deviation model, so are not shown in Figure 6.4.

It is clear in Figure 6.4 demonstrates that the  $\tau$  value determined from New Zealand data between  $M_w$ 6 and  $M_w$ 7 is poorly constrained, but  $\tau$  for events with  $5 \leq M_w \leq 6$  is high compared to the seed models, across all periods. The mean  $\tau$  value is consistently at or higher than the highest  $\tau$  model from all the seed models, but the credible intervals demonstrate that this is not statistically significant. The New Zealand dataset is unfortunately unable to inform selection of a  $\tau$  model at magnitudes larger than 6, which is the most relevant magnitude range for New Zealand hazard assessment.

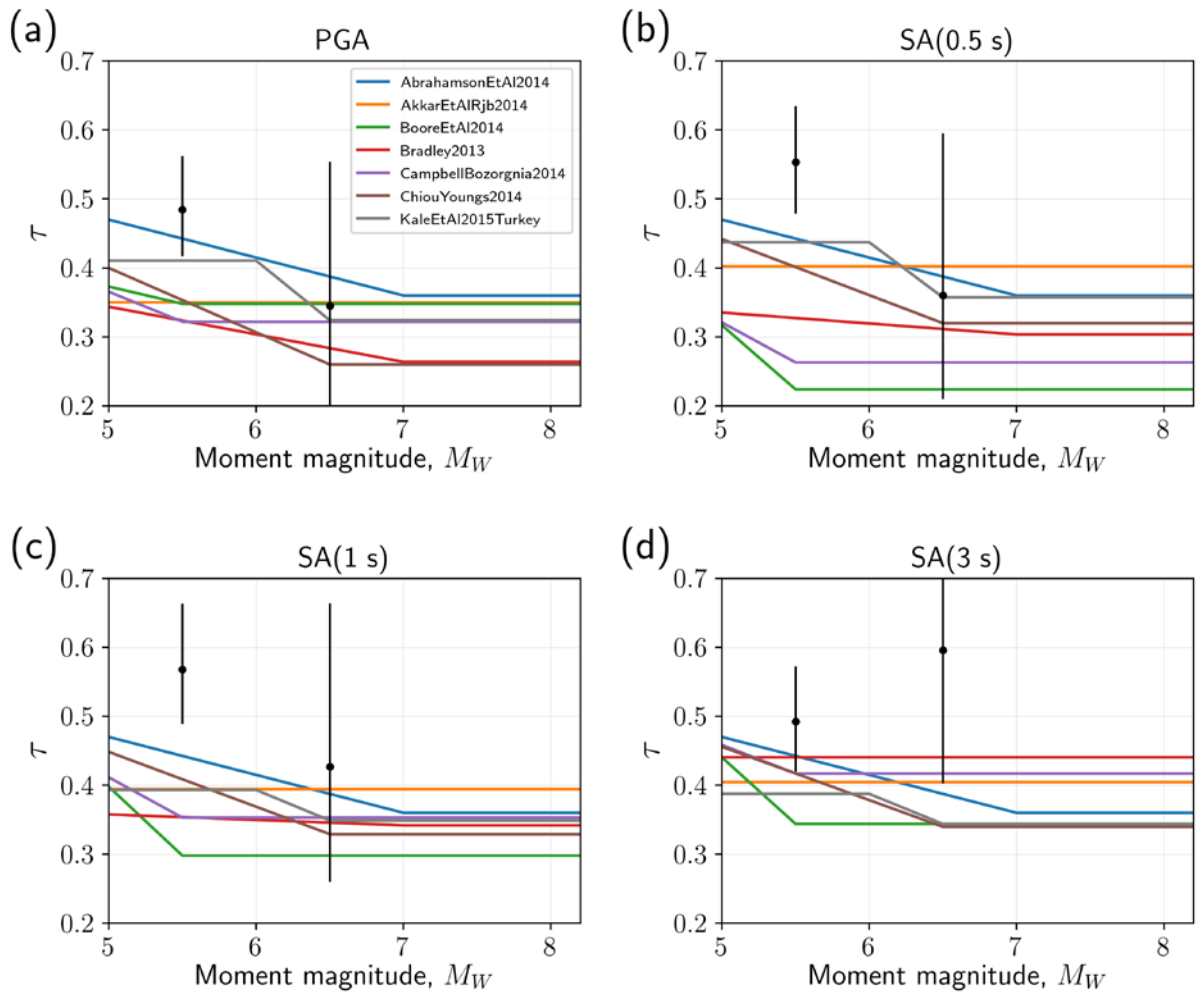


Figure 6.4 The magnitude-dependence of the between-event standard deviation,  $\tau$ , for (a) PGA, (b) SA(0.5s), (c) SA(1s) and (d) SA(3s) derived from New Zealand data, compared to the available  $\tau$  models of the seed models. Points represent expected values and bars represent 90% credible intervals.

## 6.2.2 Within-Event Standard Deviation, $\phi$

The magnitude-dependence of  $\phi$  for PGA, SA(0.5s), SA(1s) and SA(3s) is shown in Figure 6.5, and compared against to the  $\phi$  models associated with the seed models, where available. The magnitude-dependent  $\phi$  data are better constrained than the  $\tau$  data because they are underpinned by more data i.e. the total number of available recordings, as opposed to the total number of available events. The  $\phi$  data appear largely magnitude-independent across all periods in Figure 6.5, although their values relative to the seed  $\phi$  models varies strongly with oscillator period. The distance-dependence of  $\phi$ , for the same intensity measures as Figure 6.5, is shown in Figure 6.6. Only within-event residuals from events with  $M_W \geq 5$  are included in this analysis. The  $\phi$  data also appear predominantly independent of distance, similar to the  $\phi$  models from the selected seed models.

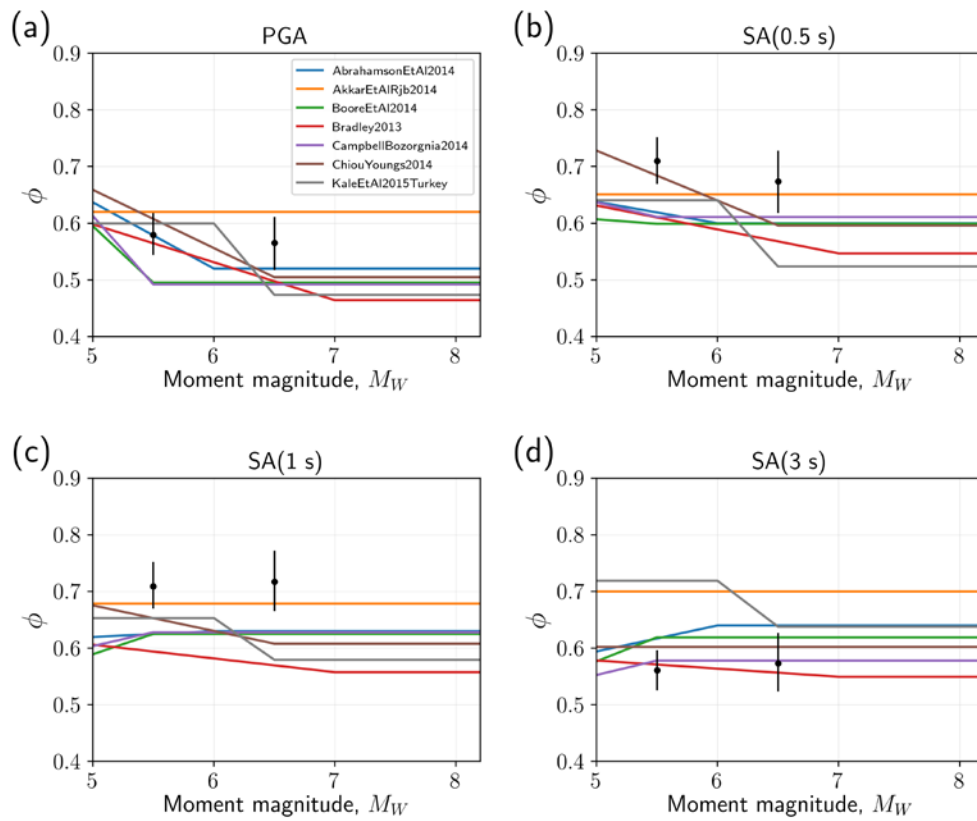


Figure 6.5 The magnitude-dependence of the within-event standard deviation,  $\phi$ , for (a) PGA, (b) SA(0.5s), (c) SA(1s) and (d) SA(3s) derived from New Zealand data, compared to the available  $\phi$  models of the seed models.

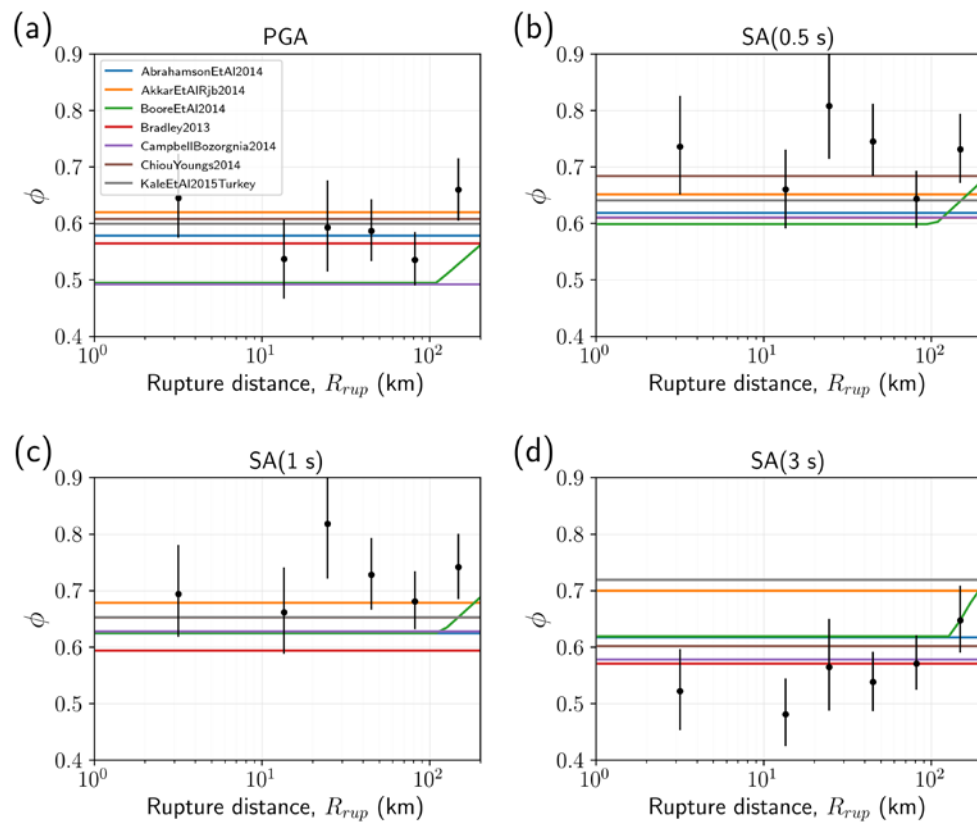


Figure 6.6 The distance-dependence of the within-event standard deviation,  $\phi$ , for (a) PGA, (b) SA(0.5s), (c) SA(1s) and (d) SA(3s) derived from New Zealand data, compared to the available  $\phi$  models of the seed models.

### 6.2.3 Single-Station Within-Event Standard Deviation, $\phi_{SS}$

$\phi_{SS}$  has been shown to be stable across many regions (Rodriguez-Marek et al. 2013). None of the seed models have associated  $\phi_{SS}$  models, but Rodriguez-Marek et al. (2013) provide  $\phi_{SS}$  models, and Al Atik (2015) derived a global  $\phi_{SS}$  model from the residuals of four NGA-West2 models (Abrahamson et al. 2014; Boore et al. 2014; Campbell and Bozorgnia, 2014; Chiou and Youngs (2014). Figure 6.7 compares the magnitude-dependence of New Zealand  $\phi_{SS}$  data against the Rodriguez-Marek et al. (2013) and Al Atik (2015) models, and Figure 6.8 compares the distance-dependence. As with the  $\phi$  analysis, only residuals from events with  $M_W \geq 5$  are analysed here.

$\phi_{SS}$ , as indicated by the New Zealand dataset, is slightly lower than the Rodriguez-Marek et al. (2013) and Al Atik (2015) global models for shorter oscillator periods and  $5 \leq M_W \leq 6$ , and comparable at longer oscillator periods for the same magnitude range. For the larger magnitudes, the  $\phi_{SS}$  data are similar to the global models. The credible intervals suggest that the short-period, low magnitude differences in  $\phi_{SS}$  are statistically significant, which contradicts the common belief that  $\phi_{SS}$  is regionally-independent.

There appears to be an increase in  $\phi_{SS}$  at short distances. Rodriguez-Marek et al. (2013) also observe a similar increase for their three largest datasets from California, Japan and Taiwan, but suggest that the increase could be a result of poorly-constrained hypocentral depths rather than a characteristic effect. In this case, the increase is likely a result of the biased predictions of the median model, due to the nature of the New Zealand database.

As discussed in Section 6.1, traditional partially-ergodic seismic hazard analysis typically applies  $\phi_{SS,S}$ , rather than  $\phi_{SS}$  in the hazard calculation (Rodriguez-Marek et al. 2013). The mean  $\phi_{SS,S}$  can vary substantially from the overall  $\phi_{SS}$ , as demonstrated in Figure 6.9, though in many cases, the differences are not statistically different from the overall mean  $\phi_{SS}$  determined in this study. Regardless, the hazard calculations in this study utilise  $\phi_{SS}$ , rather than  $\phi_{SS,S}$ .

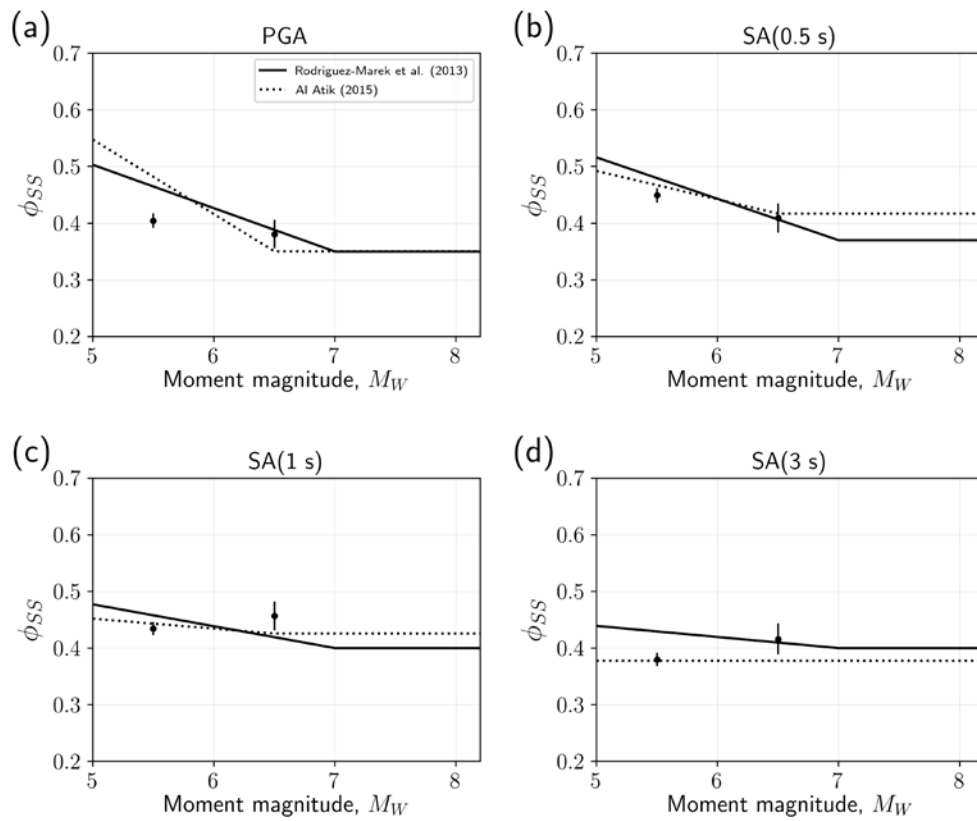


Figure 6.7 The magnitude-dependence of the single-station within-event standard deviation,  $\phi_{SS}$ , for (a) PGA, (b) SA(0.5s), (c) SA(1s) and (d) SA(3s) derived from New Zealand data, compared to the  $\phi_{SS}$  models of Rodriguez-Marek et al. (2013).

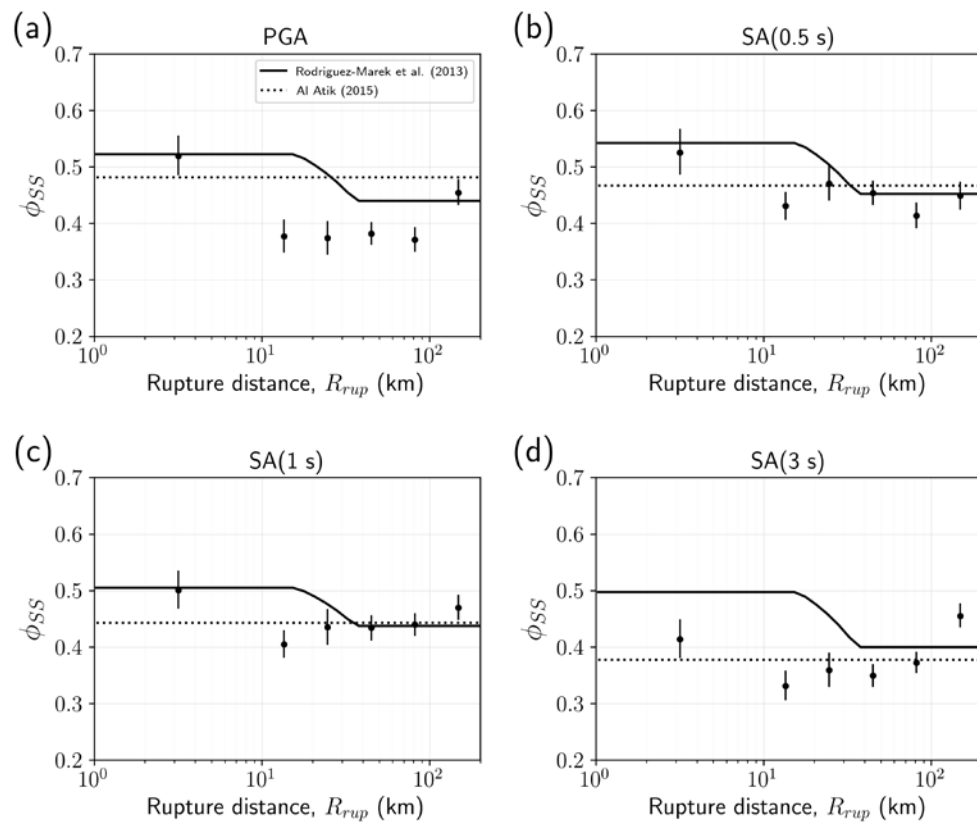


Figure 6.8 The distance-dependence of the single-station within-event standard deviation,  $\phi_{SS}$ , for (a) PGA, (b) SA(0.5s), (c) SA(1s) and (d) SA(3s) derived from New Zealand data, compared to the  $\phi_{SS}$  models of Rodriguez-Marek et al. (2013).

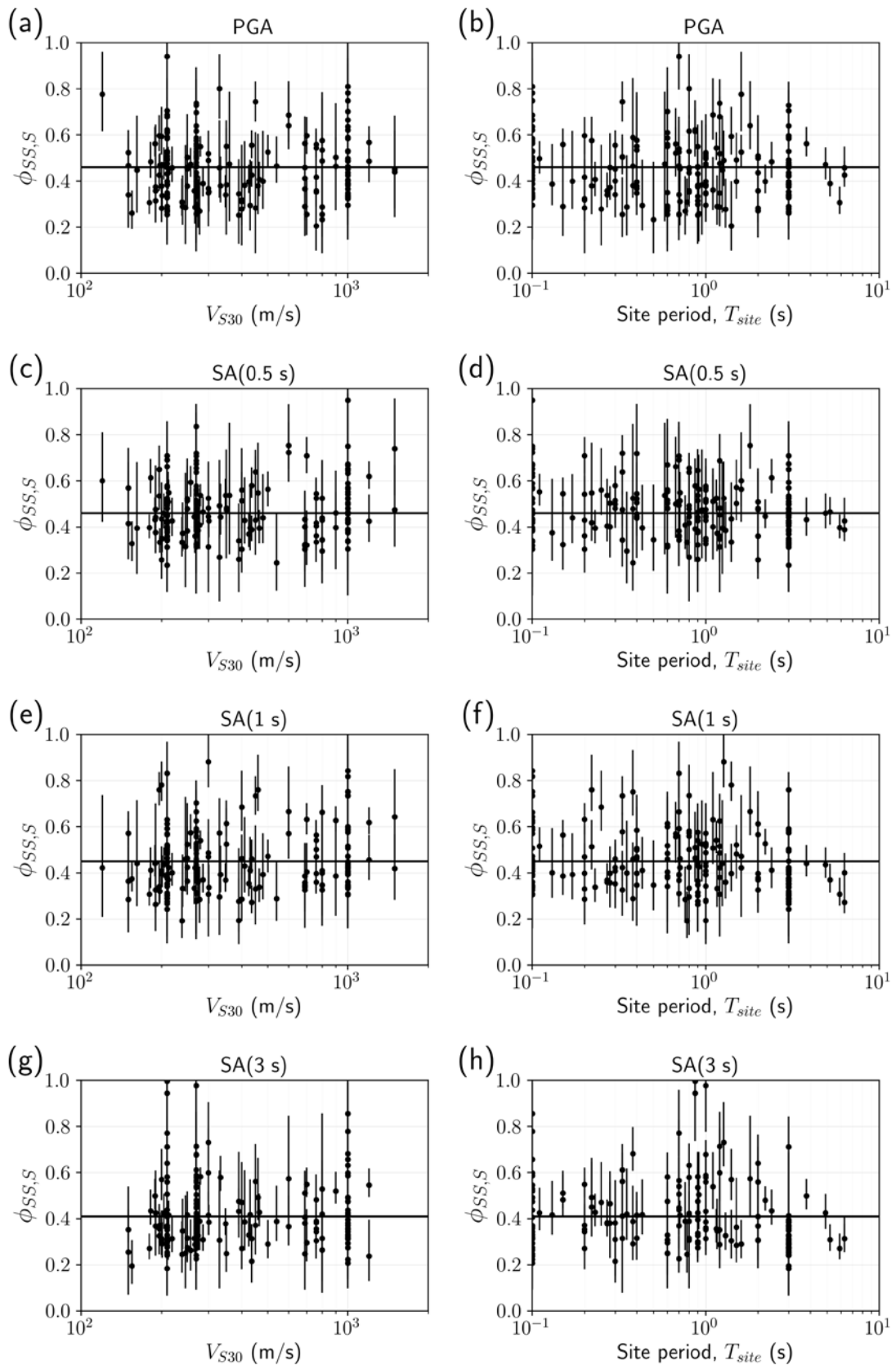


Figure 6.9 The dependence of the station-specific within-event standard deviation,  $\phi_{SS,S}$ , on  $V_{S30}$  and fundamental site period,  $T_{site}$ , for (a)-(b) PGA, (c)-(d) SA(0.5s), (e)-(f) SA(1s) and (g)-(h) SA(3s) derived from New Zealand data. Bars represent 90% credible intervals.

#### 6.2.4 Summary of Standard Deviation Observations

The dependence of the standard deviation observations on oscillator period can be found in Figure 6.10. A key observation in Figure 6.10a is the increase in  $\tau(5 \leq M_W \leq 6)$  between around 0.5 s and 2 s period, which is notably higher than any of the  $\tau$  models from the seed models. In this oscillator period range, for the magnitude range of the New Zealand data, peak spectral amplitudes are sensitive to changes in the “stress parameter”,  $\Delta\sigma$  (Molkenthin et al. 2014).  $\Delta\sigma$  is essentially a proxy for scaled source duration, which suggests that earthquake source durations may be more variable in New Zealand than globally. The  $\tau$  results are also larger than the  $\tau$  models from the seed models across all periods. With such a complex tectonic environment, it seems intuitive that events in New Zealand could be more variable than other regions in the world. There is, however, insufficient information here to determine whether this is a result of poorly-constrained  $M_W$  values in the underlying dataset, or a physical effect. The  $\tau$  values may reduce when uncertainties in  $M_W$  values from the New Zealand Strong Motion Database are explicitly modelled (Rhoades, 1997; Stafford, 2014a; Kuehn and Abrahamson, 2018). Modelling these uncertainties was not considered here for simplicity but will be modelled in future work.

The  $\phi$  results are largely comparable to the global models, while  $\phi_{SS}$  is lower for the New Zealand short-period data than the global models of Rodriguez-Marek et al. (2013) and Al Atik (2015). None of the seed models have associated  $\phi_{S2S}$  models associated with them, nor does a comparable model exist to the author’s knowledge. There is a peak in the  $\phi_{S2S}$  result at oscillator periods around one second, which may be due to many sites in Wellington and Christchurch that resonate at around one second (Kaiser et al. 2017). Fundamental-mode site period is rarely included as a predictive parameter in empirical ground-motion models. The lack of consideration may lead to misleading ergodic seismic hazard calculations, although this is mitigated when modelling  $\delta S2S_s$  in partially-ergodic hazard analysis. In addition to the 1 s resonance influencing the large  $\phi_{S2S}$  values,  $\phi_{S2S}$  is also likely to be inflated due to misclassified sites in terms of  $V_{S30}$  and  $Z_1$ .

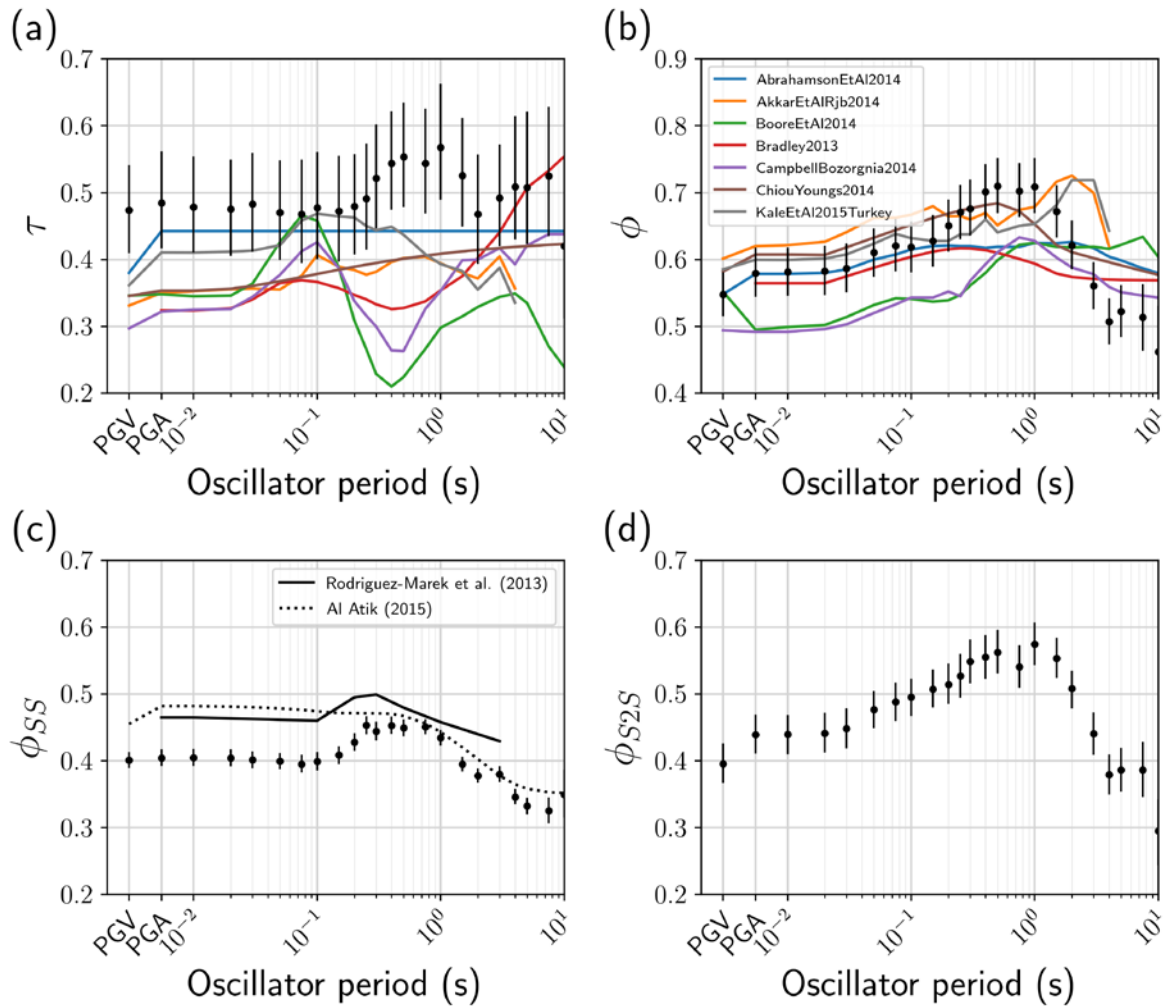


Figure 6.10 The period-dependence of  $\tau$ ,  $\phi$ ,  $\phi_{SS}$  and  $\phi_{SS2S}$  derived from New Zealand  $M_w \geq 5$  data. The  $\tau$  and  $\phi_{SS}$  data in (a) and (c) are for  $5 \leq M_w \leq 6$  only, as the data are expected to be magnitude-dependent. The bars represent 90% credible intervals. The published model predictions are for  $M_w = 5.5$  and  $R_{rup} = 30$  km.

## 6.3 Selected Standard Deviation Models

### 6.3.1 Model for The Between-Event Standard Deviation, $\tau$

Given that the New Zealand dataset cannot inform the behaviour of  $\tau$  at large magnitudes, the large-magnitude scaling of the New Zealand specific  $\tau$  model is constrained to match the Al Atik (2015) global  $\tau$  model, which is an average  $\tau$  from the NGA-West2  $\tau$  models. At lower magnitudes,  $M_w < 6.5$ , the model is guided by the New Zealand data. The model is given by

$$\tau(T) = \begin{cases} \tau_1(T), & M_w \leq 5.5 \\ \tau_1(T) + (M_w - 5.5) \times (\tau_2 - \tau_1(T)), & 5.5 < M_w < 6.5 \\ \tau_2, & M_w \geq 6.5 \end{cases} \quad (6.9)$$

The values of  $\tau_1(T)$  are determined by smoothing the  $\tau(5 \leq M_w \leq 6)$  data in Figure 6.10 across the logarithm of oscillator period using a lowess fit. The PGA and PGV values are unsmoothed.  $\tau_2$  is independent of oscillator period and taken from the Al Atik (2015) global model. The breakpoint for  $\tau_1(T)$  is at  $M_w 5.5$ , the centre of the binned data, rather than  $M_w 6$ , to allow a more gradual transition between  $\tau_1$  and  $\tau_2$ . The model is shown in Figure 6.11a.

The mean  $\tau$  values are subject to uncertainty, with 90% credible intervals spanning more than 0.1 natural log unit. 5% and 95%  $\tau$  models are also derived, where  $\tau_{1\_5\%}(T)$  and  $\tau_{1\_95\%}(T)$  are determined by smoothing the  $\tau(5 \leq M_W \leq 6)$  credible interval data in Figure 6.10, and the difference between  $\tau_1$  from these models and the mean  $\tau_1(T)$  model are held constant across magnitude. The median, 5% and 95% models are assigned weights of 0.63, 0.185 and 0.185 respectively, following Al Atik (2015).

### 6.3.2 Model for The Within-Event Standard Deviation, $\phi$

The  $\phi$  model is magnitude- and distance-independent, and is determined by smoothing the  $\phi(M_W \geq 5)$  data with a lowess fit. The model is shown in Figure 6.11b. As the  $\phi$  values are much better constrained than the  $\tau$  values, modelling of uncertainty in  $\phi$  is not considered necessary unless very low probabilities of exceedance become of more interest to New Zealand PSHA.

### 6.3.3 Model for The Single-Station Within-Event Standard Deviation, $\phi_{SS}$

The selected model is shown in Figure 6.11c, and is given by

$$\phi_{SS}(T) = \begin{cases} \phi_{SS1}(T), & M_W \leq 5.5 \\ \phi_{SS1}(T) + (M_W - 5.5) \times (\phi_{SS2}(T) - \phi_{SS1}(T)), & 5.5 < M_W < 6.5 \\ \phi_{SS2}(T), & M_W \geq 6.5 \end{cases} \quad (6.10)$$

Similar to the  $\tau$  model, the large-magnitude behaviour of the selected  $\phi_{SS}$  model is guided by the global Al Atik (2015) model. For oscillator periods greater than one second, the  $\phi_{SS1}$  and  $\phi_{SS2}$  parameters are identical to the Al Atik (2015) “a” and “b” parameters. Below one second,  $\phi_{SS1}$  is determined by a lowess fit of the  $\phi_{SS}(5 \leq M_W \leq 6)$  data in Figure 6.10c across the logarithm of oscillator period. For the same reason as the  $\phi$  model, no uncertainty in  $\phi_{SS}$  is modelled here.

### 6.3.4 Model for The Site-To-Site Standard Deviation, $\phi_{S2S}$

The  $\phi_{S2S}$  model is magnitude- and distance-independent and is determined by smoothing the  $\phi_{S2S}$  data with a lowess fit across log(period). The model is shown in Figure 6.11d.

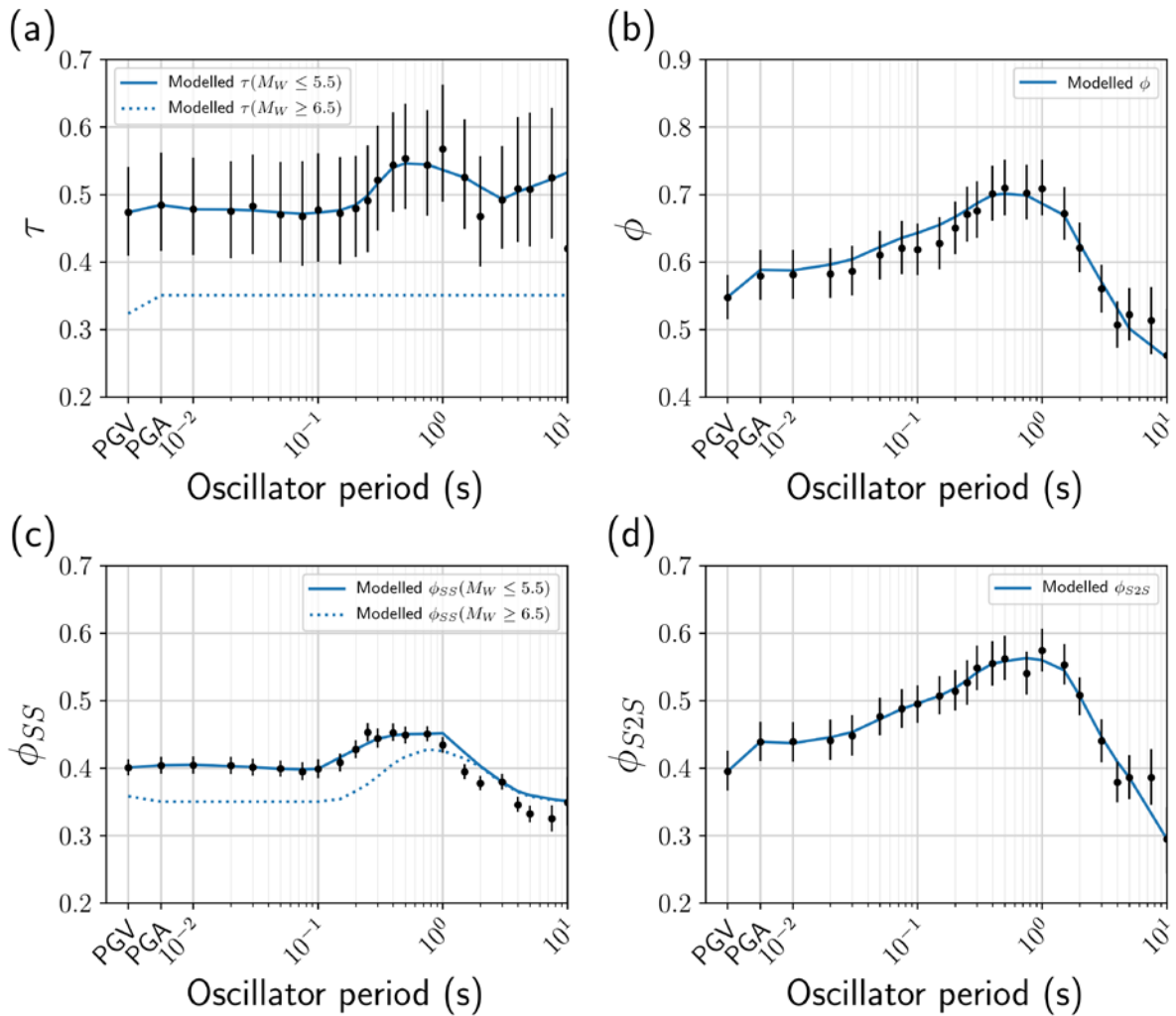


Figure 6.11 The period-dependence of the  $\tau$ ,  $\phi$ ,  $\phi_{SS}$  and  $\phi_{S2S}$  models derived from New Zealand data. The bars represent 90% credible intervals.

### 6.3.5 Additional Considerations

An important aspect of seismic hazard analysis for Wellington is whether  $\phi$  and  $\phi_{SS}$  are different in the near-field ( $R_{rup} < 10$  km). With hazard from crustal faults heavily dominated by a Wellington Fault rupture,  $\phi$  and  $\phi_{SS}$  values essentially need to be representative of a single  $M_W 7.5$ ,  $R_{rup} < 10$  km scenario, where there are very few data to constrain the values. With insufficient data, one must revert to simulated ground-motion to inform this issue. Several studies have used ground-motion simulations to estimate  $\phi$  at short distances. For example, Imtiaz et al. (2014) find that for bilateral ruptures,  $\phi$  decreases as source-to-site distance decreases but observe the opposite trend for unilateral ruptures. Vyas et al. (2016) perform simulations for unilateral strike-slip events and derive a model for  $\phi$  that increases as source-to-site distance decreases for unilateral strike-slip ruptures, but the values are substantially different to what is indicated by empirical models, even at large distances.

The Imtiaz et al. (2014) and Vyas et al. (2016) studies utilised 1D velocity models and low frequency simulations. Withers et al. (2019b) modelled a bilateral strike-slip earthquake with 3D simulations, complete with fault roughness, small-scale medium heterogeneities and medium plasticity. The simulations showed a decrease in  $\phi$  for distances less than around 20 km. Withers et al. (2019a) perform a similar analysis for a buried thrust fault, and find that,

for the most part,  $\phi$  is larger at short distances (less than around 20 km) compared to larger distances, particularly for short oscillator periods.

Generally, it appears likely that  $\phi$  is larger in the near-field when dealing with unilateral rupture directivity, but smaller when directivity is not a factor. Bilateral ruptures appear more common than strongly unilateral ruptures (Mai et al. 2005; Melgar and Hayes, 2019). In the author's opinion, the results cannot yet be generalised for hazard assessment, and a simulation study that applies probabilistic hypocentral locations to a variety of fault types is necessary before decisions can be made on short-distance behaviour of  $\phi$ . For this reason, this study models  $\phi$  (and  $\phi_{SS}$ ) as distance-independent.

#### 6.4 Between-Station Terms, $\delta S2S_s$

From this analysis,  $\delta S2S_s$  terms are now available for each station and can be utilised in partially-ergodic seismic hazard calculations. Example  $\delta S2S_s$  terms for six sites in Wellington are shown in Figure 6.12. The selected sites are the Wellington Airport (WNAS), a rock site outside the northern Wellington CBD basin (POTS), two stations in the northern Wellington CBD basin (WEMS and VUWS) and two stations in the southern Wellington CBD basin (TEPS and FKPS). These  $\delta S2S_s$  terms provide broadly similar inferences to previous site response studies, that Wellington basin response consists of strong amplification in the 1-2 s range (e.g. Holden et al. 2013; Kaiser et al. 2017; Bradley et al. 2018; Ren et al. 2018). The differences in  $\delta S2S_s$  from zero can be a result of a site's systematic deviation in response from a generic site response model parametrised by  $V_{S30}$  and  $Z_1$ , as well as a result of site misclassification with incorrect  $V_{S30}$  and  $Z_1$  values.

$\delta S2S_s$  terms for six sites in Christchurch are shown in Figure 6.13, three located in the main Christchurch urban area (CBGS, REHS, CACS), one in the Heathcote Valley (HVSC), one in the Port Hills (STKS), and one in Lyttelton (LPCC). These  $\delta S2S_s$  terms are similar to those in Bradley (2015) but are expected to be slightly different because they are derived from an unbiased median model, the recordings are processed using a different method, and they defined relative to different values of  $V_{S30}$  and  $Z_1$ .

The  $\delta S2S_s$  terms for both cities, and their posterior credible intervals, can be utilised in partially-ergodic hazard calculations in Wellington and Christchurch. The median, 5% and 95% values for each  $\delta S2S_s$  posterior distribution at each intensity measure receive weights of 0.63, 0.185 and 0.185 respectively, following Al Atik and Youngs (2014). Figure 6.14 shows how the  $\delta S2S_s$  become better constrained as the number of observations increase, with the narrower credible intervals representing a reduction in the epistemic uncertainty.

These  $\delta S2S_s$  terms are independent of magnitude, yet linear site effects terms of response spectral models are expected to be magnitude- and distance-dependent (Zhang and Zhao, 2009; Zhao et al. 2009; Stafford et al. 2017). For both Wellington and Christchurch, the magnitudes of the data used to derive the  $\delta S2S_s$  terms are not too far removed from the key crustal seismic sources for their PSHA but are still predominantly of lower magnitude. This issue cannot easily be addressed given that the Abrahamson et al. (2014)  $f_{site}$  model, and other NGA-West2 models, are independent of magnitude and distance. Future  $f_{site}$  models are likely to model linear site effects as magnitude- and distance-dependent, which will mitigate this issue. Additionally, these  $\delta S2S_s$  terms only adjust ground-motion models for linear site effects, with nonlinear site response remaining ergodic.

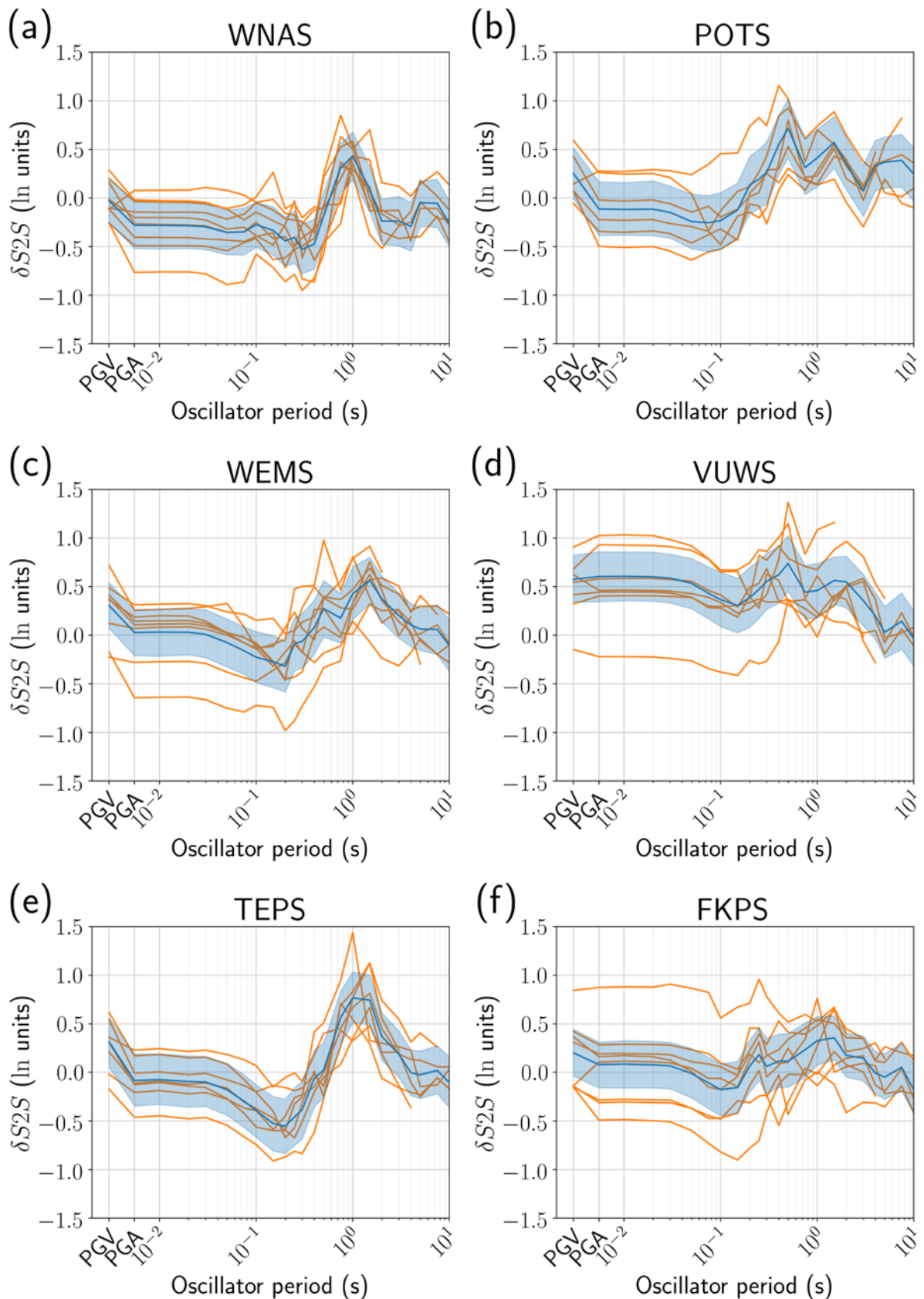


Figure 6.12  $\delta S2S_s$  functions at Wellington stations (a) WNAS, (b) POTS, (c) WEMS (d) VUWS, (e) TEPS and (f) FKPS. Dark blue lines represent the expected value of  $\delta S2S_s$ , light blue shaded area is the 90% credible interval of the posterior distribution and orange lines are the mean within-event residuals.

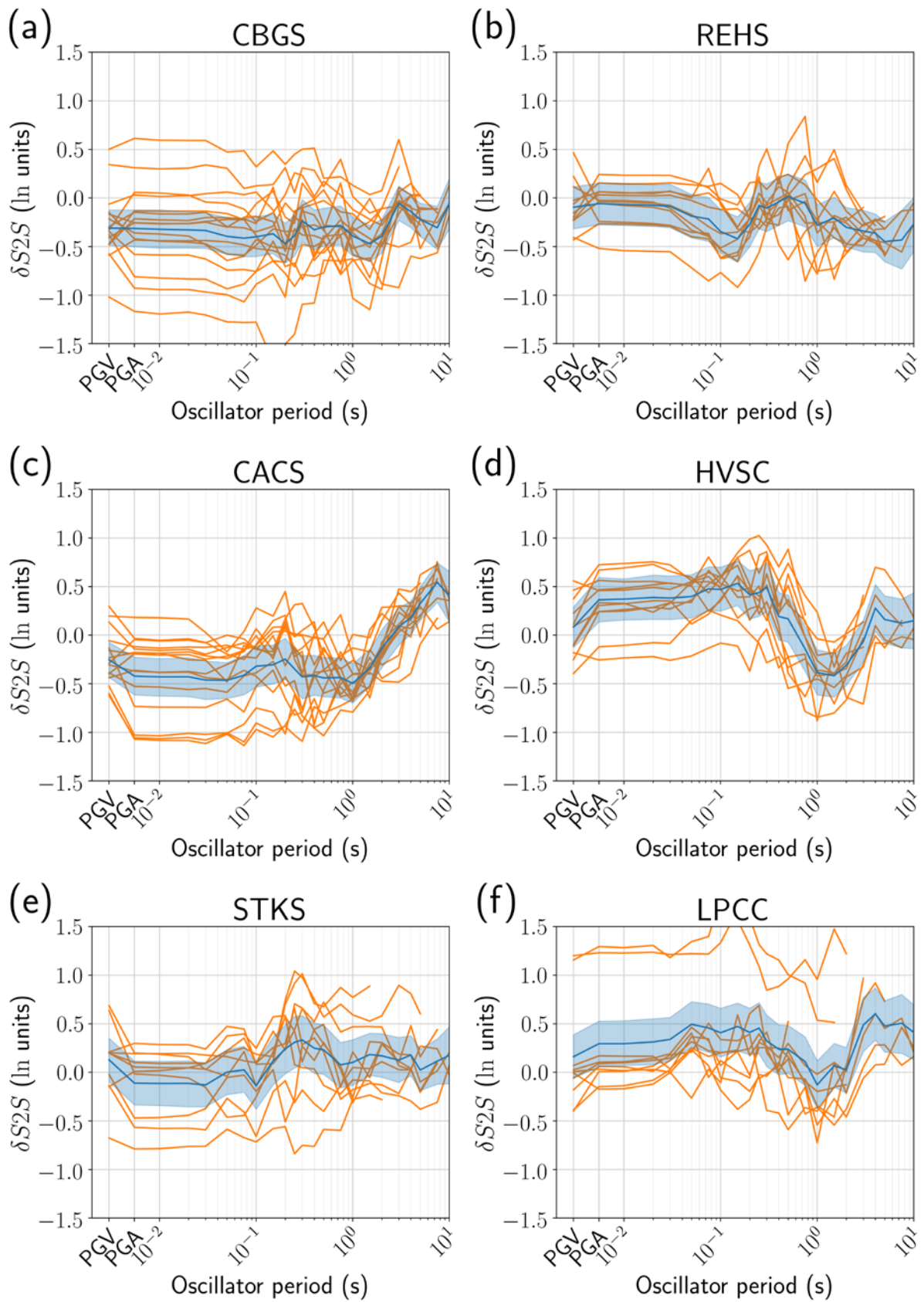


Figure 6.13  $\delta S2S_s$  functions at Christchurch stations (a) CBGS, (b) REHS, (c) CACS (d) HVSC, (e) STKS and (f) LPCC. Dark blue lines represent the expected value of  $\delta S2S_s$ , light blue shaded area is the 90% credible interval of the posterior distribution and orange lines are the mean within-event residuals.

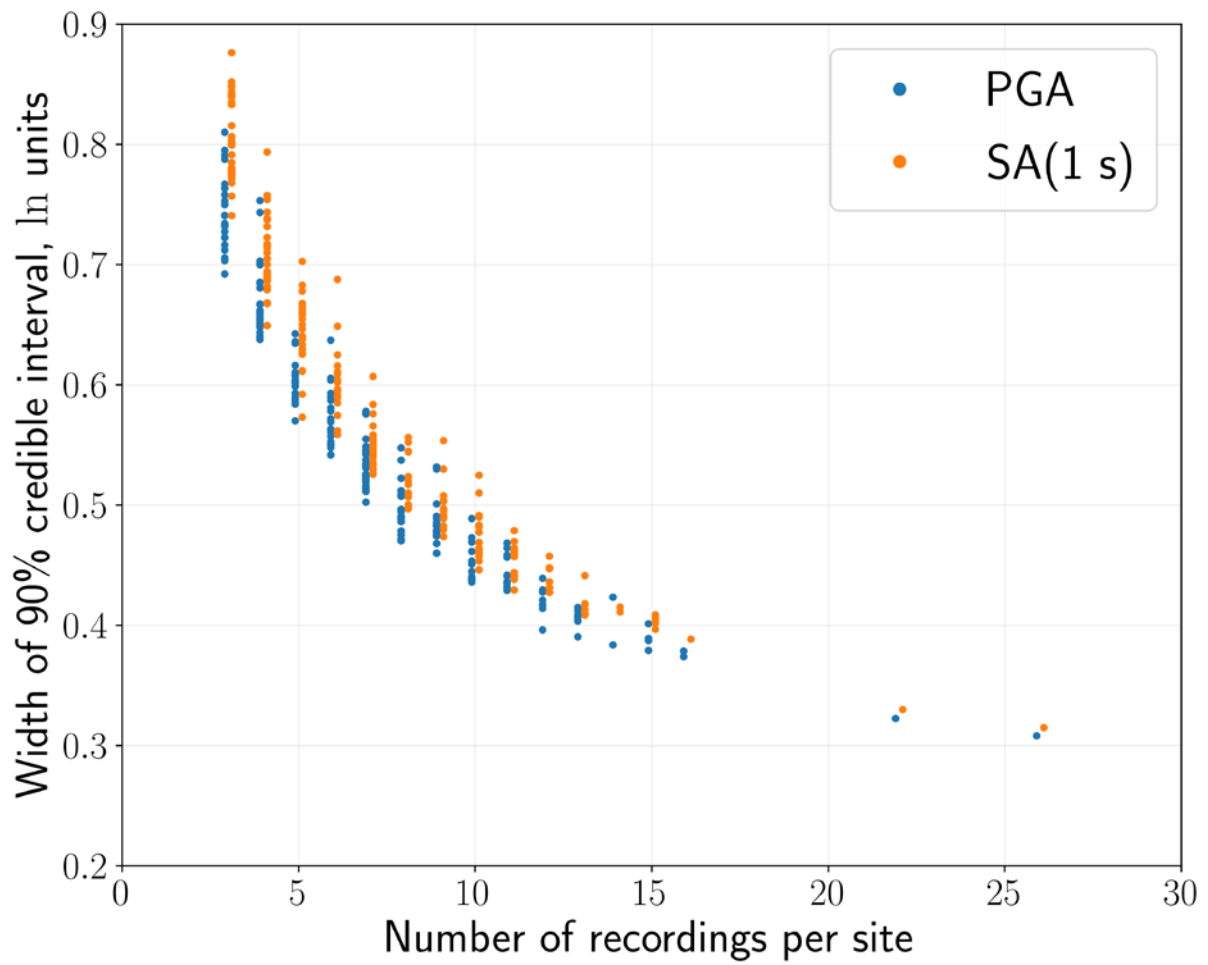


Figure 6.14 Reduction in the 90% credible interval of the posterior distribution for  $\delta S2S_s$  with increasing number of recordings at site  $s$ .

## 7.0 MODEL WEIGHTING

Epistemic uncertainties in probabilistic seismic hazard analyses are propagated in a 'logic tree' framework, whereby hazard results are obtained for each possible interpretation independently, then the outputs are combined together in a weighted average. Thus far, this study has provided 17 different interpretations for median ground motion for shallow crustal earthquakes, and three different interpretations for the corresponding ground-motion standard deviation. The different median and standard deviation interpretations lie on different levels of the ground-motion logic tree. To calculate the weighted average hazard, each of the 17-median ground-motion models need to be assigned weights that sum to one.

Assigning weights is a fraught process and is often based on expert judgement rather than clear evidence. The method used to derive the seventeen models, however, mitigates one common issue of model weighting through expert judgement, where two models that predict similar ground motion are assigned different weights. In this section, weights are assigned using two separate methods, (a) where weights are assigned without data using prior information and (b) where weights are assigned based on comparison of the models against recorded data from the New Zealand Strong Motion Database. These two methods are combined to obtain overall weights, that can be utilised to calculate seismic hazard spectra. These weighting methods are considered demonstrative only and can be iterated upon in the future to discern the best method for calculating model weights.

### 7.1 Prior Weights

In PSHA studies around the world, model weights are often assigned without using recorded data, because it is rare for apposite data for a given site to be available. Equal weights are often the default choice for many hazard analysts, which essentially corresponds to an uninformative prior. This study utilises the procedure for selecting models in section 5.2 to provide a more informative prior. The ellipse for defining the space was derived by fitting the convex hull to the seed models, which were scaled to define the 95% confidence interval boundaries of the Al Atik and Youngs (2014) epistemic uncertainty model. By making the assumption that this ellipse corresponds to the 95% confidence ellipse of a bivariate normal distribution, each selected common-form model can be assigned a weight based on its probability from this bivariate normal distribution. Examples of the probability density of this bivariate normal distribution for the PGA and SA(3s) predictions from the widely-applicable models are shown on the Sammon's maps in Figure 7.1a and Figure 7.1c respectively. Recalling that the regions on the Sammon's map for selecting models are defined by scaling the fitted ellipse by factors of 0.4, 0.8 and 1.2, these respectively correspond to error ellipses of 38%, 85% and 99% confidence. This means that the central model is assigned a weight of 0.38, the eight models in the inner ring each receive weights of 0.06 and the eight models in the outer ring each receive weights of 0.017. These weights are normalised to sum to one. Examples of model weights are shown in Figure 7.1b and Figure 7.1d respectively. Note that the prior weights for each cell are identical for all cases.

This procedure differs from that in Phung et al. (2019), who calculate sample probabilities from the multivariate normal parameter distribution to assign prior weights. In this study, the covariance matrix from the multivariate normal parameter distribution was not positive definite, so no density function exists, and the sample probability cannot be calculated.

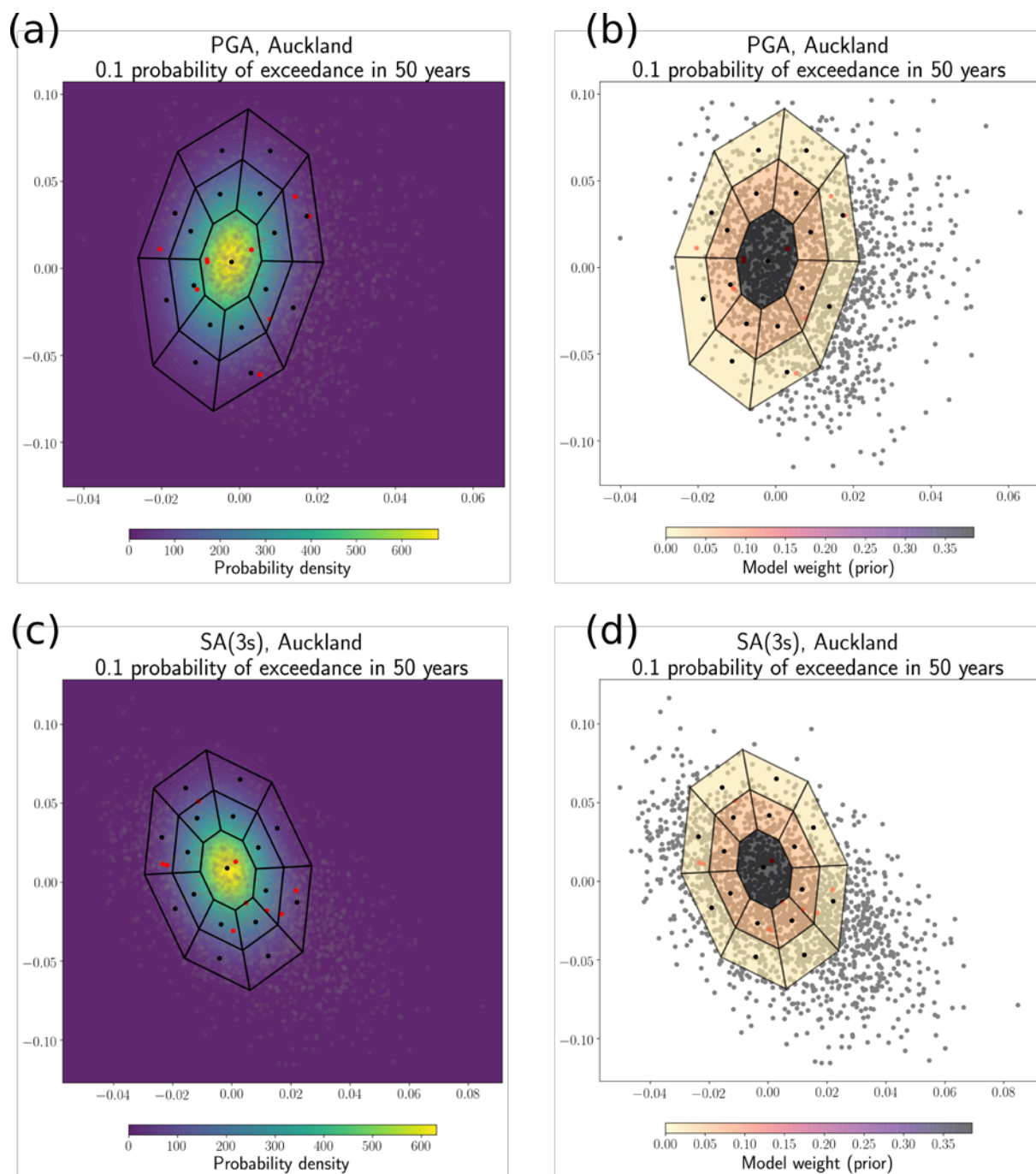


Figure 7.1 (a) and (c) probability density of the bivariate normal distribution, based on the assumption that the fitted ellipse corresponds to a 95% confidence error ellipse, for PGA and SA(3s) respectively. (b)-(d) the corresponding model weights based on the density functions in (a) and (c).

## 7.2 Data-Driven Weights

Model weights can also be derived from data, using numerous methods. This study utilises two methods, based on model mean bias and model log-likelihood, similar to Goulet et al. (2018) and Phung et al. (2019).

### 7.2.1 Selection of Data

To compare the models to recorded data, it is important to select data that are as relevant as possible to the hazard-contributing scenarios. For example, events with moment magnitudes between  $M_w5$  and  $M_w7$  contribute strongly to the 10% probability of exceedance in 50-year

hazard in Auckland and Christchurch across most oscillator periods, while in Wellington, only events with  $M_W > 7$  have large influence. For this reason, the models for each location are compared to different subsets of the New Zealand Strong Motion Database (Van Houtte et al. 2017). Specifically:

- For Auckland, the models are compared to all recorded crustal earthquake data with magnitudes between  $M_w 4.5$  and  $M_w 7.5$ , with rupture distance  $R_{rup} < 100$  km.
- For Wellington, the models are compared to crustal data with  $M_W > 6$  and  $R_{rup} < 50$  km, including data from the Cook Strait, Lake Grassmere and Kaikōura earthquakes.
- For Christchurch, the test dataset consists of eight crustal events from the Canterbury earthquake sequence with  $R_{rup} < 80$  km are compared to the derived models.
- The widely-applicable set of models are compared to all crustal data with  $M_W > 5$  and  $R_{rup} < 100$  km.

For all locations, a minimum of three recordings per event is required, and recordings are neglected if the accelerogram triggered on the S-wave instead of the P-wave.

### 7.2.2 Mean Between-Event Residual

To address the mean bias of the common-form models with respect to the recorded data, it is necessary to calculate residuals between the common-form models and the data. As empirical ground-motion models are typically hierarchical models that separate event-specific and site-specific effects, residuals need to be partitioned accordingly when comparing models against a test dataset. The event-specific effect or between-event residual,  $\delta B_e$ , is the residual of interest when comparing the models against data, because bias from between-site residuals can be addressed with site-specific modelling in partially-ergodic hazard assessment. To calculate the between-event residuals, the data are corrected using the  $\delta S2S_s$  terms calculated in Section 6.0, then the between-event residuals are calculated using the following equation, adapted from Abrahamson and Youngs (1992),

$$\delta B_{e,i} = \frac{\tau^2 \sum_{j=1}^{n_i} (\ln Y_{ij} - \mu_{ij})}{n_i \tau^2 + \phi_{SS}^2} \quad (7.1)$$

$i$  corresponds to the event number,  $n_i$  is the number recordings in event  $i$ ,  $j$  is the index of each recording,  $\mu$  is the median prediction and  $\ln Y$  is the observation.  $\phi_{SS}$  is used in the denominator, rather than  $\phi$ , because the data are corrected by the  $\delta S2S_s$  terms.

Contours of the mean between-event residuals for the widely-applicable set of PGA and SA(3s) models are shown in Figure 7.2. The weights in each cell are determined by

$$w_{\delta B_e} = \frac{1}{N_{k,c} \sum_{c=1}^C A_c} \sum_{k=1}^{N_{k,c}} \frac{1}{\left| \sum_{i=1}^I \delta B_{e,i} + \alpha \right|} \times A_c \quad (7.2)$$

in each cell  $c$ , where  $I$  is the total number of events in the test dataset,  $k$  is the model index,  $N_{k,c}$  is the total number of  $k$  models in cell  $c$ ,  $A_c$  is the area of the cell on the Sammon's map and  $C$  is the total number of cells. A constant  $\alpha$  of 0.015 is added to  $\delta B_e$  to avoid singularities.

The quantity in equation (7.2) is calculated across all cells then normalised to sum to one. The model weights based on this procedure are also shown in Figure 7.2.

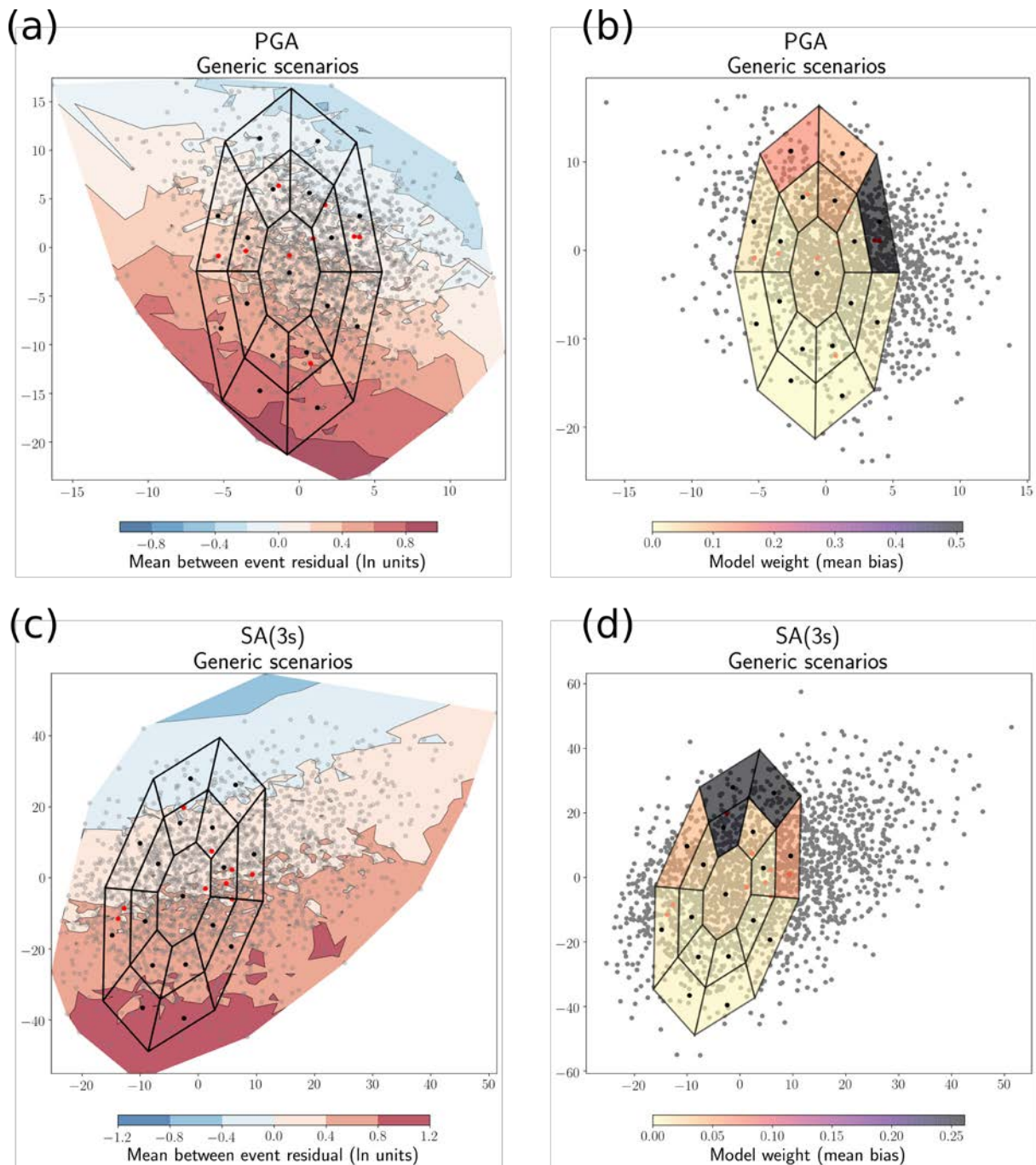


Figure 7.2 (a) and (c) the mean between-event residual for the widely-applicable set of models, for PGA and SA(3s) respectively. (b)-(d) the corresponding model weights based on the mean between-event residuals in (a) and (c).

### 7.2.3 Log-Likelihood

Another method of comparing models against data is through the log-likelihood of the model given the observations. This method tests models based on their predicted standard deviation information as well as overall bias. As empirical ground-motion models are hierarchical, the model log-likelihood for each model is calculated using the multivariate log-likelihood score of Mak et al. (2017).

As described in Section 7.2.2, residuals are corrected using the  $\delta S_2 S_s$  terms before comparing to the models, and as such the standard deviation term used for log-likelihood calculation is  $\sigma_{SS}$  rather than the total  $\sigma$ . Figure 7.3a and Figure 7.3c shows the log-likelihood contours for the same models in Figure 7.2.

Weights can be calculated from the log-likelihood data using different methods. A very popular method is that of Scherbaum et al. (2009), based on the negative average sample log-likelihood,  $-\overline{LLH}$ . In this approach, the weight for model  $k$  is calculated using

$$w_{\overline{LLH}_k} = \frac{2^{-\overline{LLH}_k}}{\sum_{k=1}^K 2^{-\overline{LLH}_k}} \quad (7.3)$$

Weights determined using this approach do not converge to the best model and tend not to distinguish strongly between well-performing and poorly-performing models. Mak et al. (2017) propose a frequentist weight, that we have adapted slightly here.

$$w_c = \frac{1}{N_{bs}} \sum_s^{N_{bs}} \mathbb{1} \left( \max_{k_c} \{ \mathcal{L}_{k_c}^{(s)} \} = \max_{k_c, c} \{ \mathcal{L}_{k_c, c}^{(s)} \} \right) \quad (7.4)$$

In this equation, the weight  $w$  in cell  $c$  is determined by the number of times, over  $N_{bs}$  cluster bootstrap samples, that the  $k$ th model in cell  $c$  with the largest log-likelihood  $\mathcal{L}$  is equal to the maximum log-likelihood of all  $k$  models located in all  $c$  cells. The double-struck 1 is the indicator function that takes a value of 1 if the statement in brackets is true, and zero otherwise. One bootstrap sample  $s$  consists of the suite of  $I$  events in the test dataset sampled  $I$  times with replacement, and  $N_{bs}$  equals to 2000. Mak et al. (2017) interpret this weight to be the probability that the model is better than the other models. In this study, this meaning is altered to be the probability that the selected model from cell  $c$  is better than the selected models in all other cells, assuming that the selected model from cell  $c$  is a good representation of the best model within that cell. The weights from this approach are shown in Figure 7.3b and Figure 7.3d.

### 7.3 Overall Weights

To determine overall model weights, a ‘weights on weights’ approach is taken, similar to Goulet et al. (2018) and Phung et al. (2019). For example, the overall weights  $w_{overall}$  can be calculated using

$$w_{overall} = a \times w_{prior} + b \times (c \times w_{\delta B_e} + d \times w_{LL}) \quad (7.5)$$

where  $a + b = 1$  and  $c + d = 1$ ,  $w_{prior}$  are the prior weights,  $w_{\delta B_e}$  are the data-driven weights using mean between-event residual criterion and  $w_{LL}$  are the data-driven weights calculated using equation (7.4). The values of  $a$ ,  $b$ ,  $c$  and  $d$  should typically be dependent on intensity measure and determined through expert elicitation, but some example weights, independent of intensity measure and probability of exceedance, are shown in Table 7.1. These weights are utilised for seismic hazard outputs in the following section.

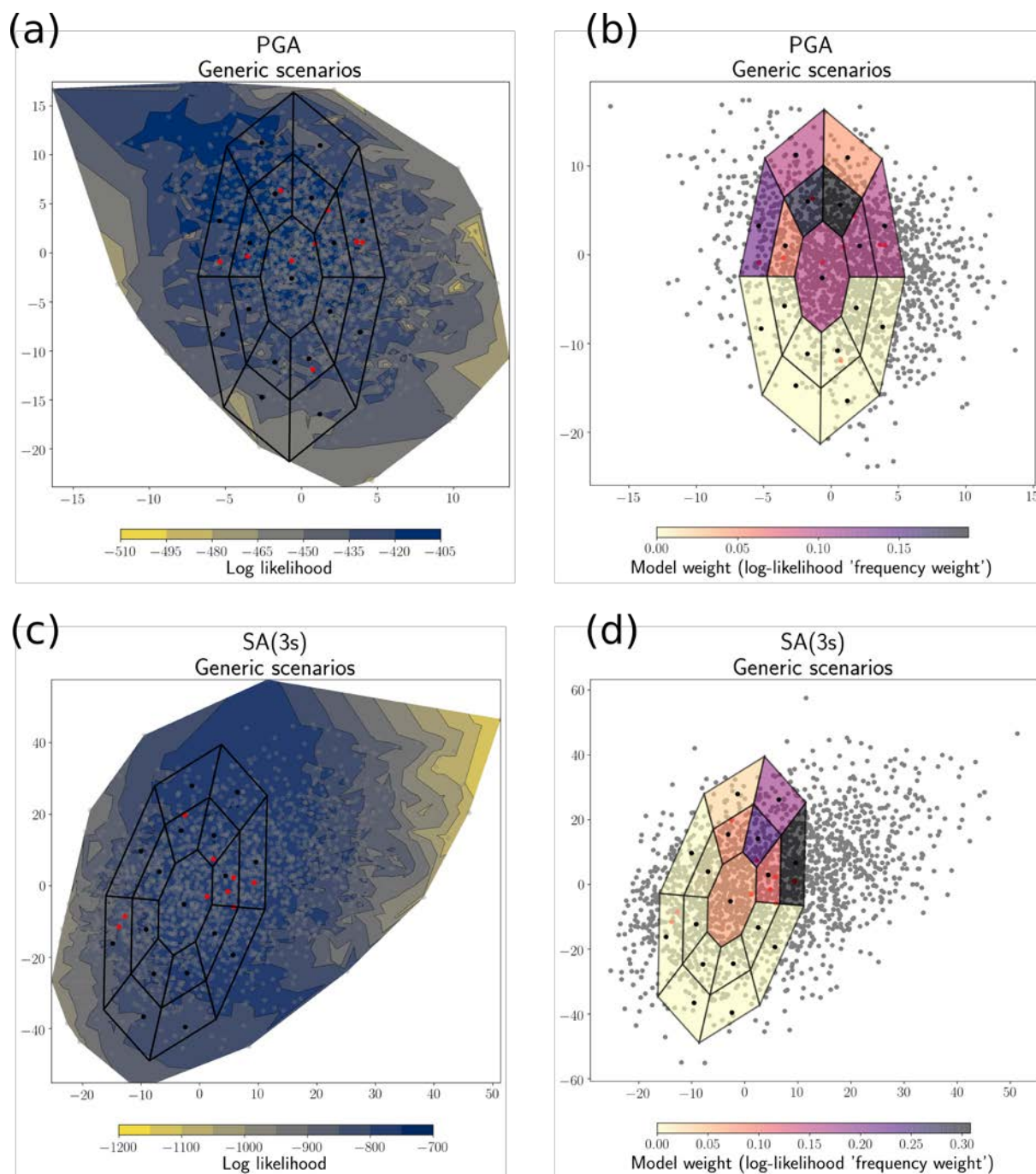


Figure 7.3 (a) and (c) the log-likelihood contours for the widely-applicable set of models, for PGA and SA(3s) respectively. (b)-(d) the corresponding model weights based on the mean between-event residuals in (a) and (c).

Table 7.1 Example “weights on weights” used to calculate hazard results.

Model set	a	b	c	d
Auckland	0.6	0.4	0.5	0.5
Wellington	0.6	0.4	0.5	0.5
Christchurch	0.2	0.8	0.5	0.5
Widely-applicable	0.6	0.4	0.5	0.5

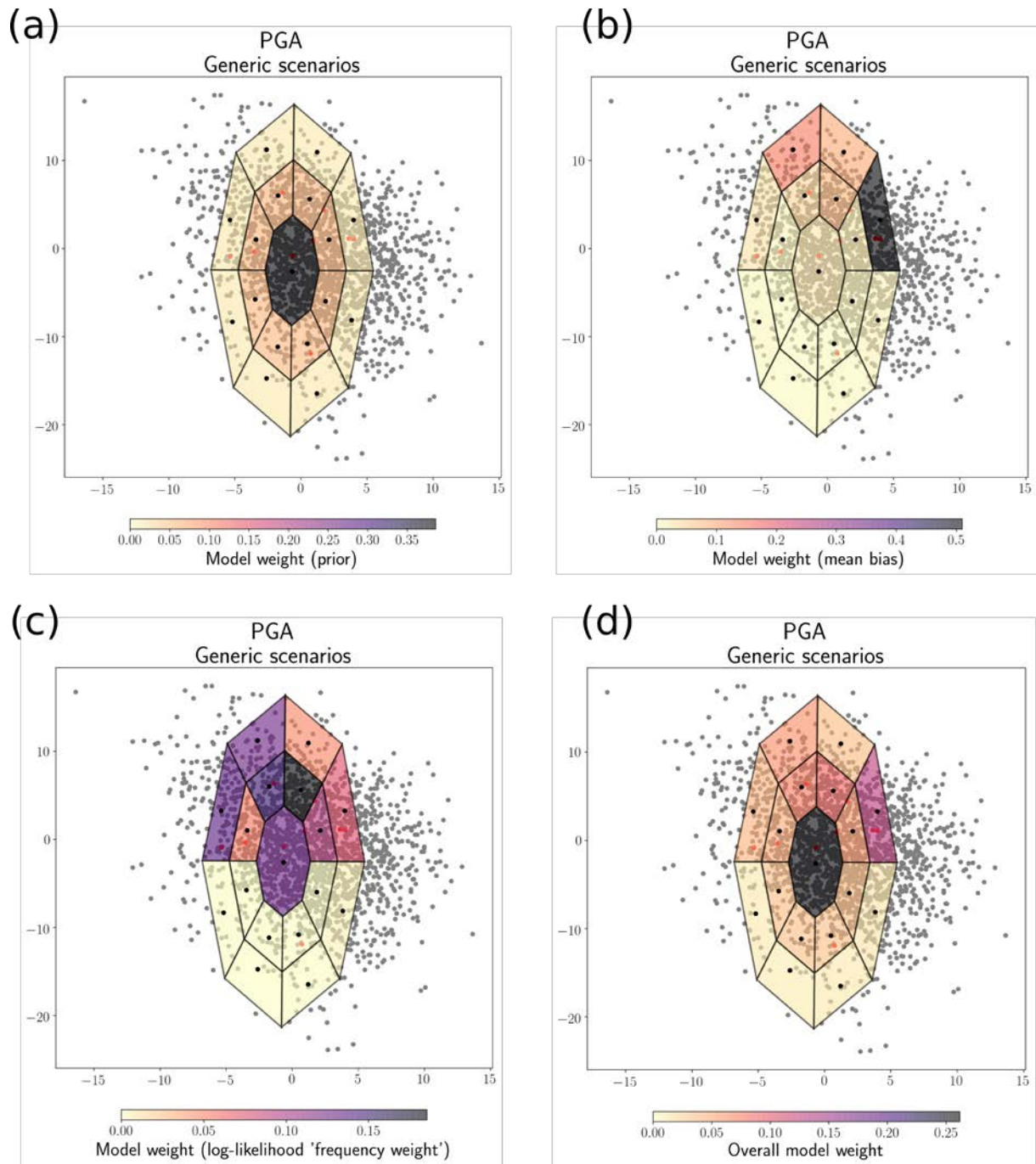


Figure 7.4 Weights for the widely-applicable model set for PGA (a) prior weights, (b) mean between-event residual, (c) log-likelihood and (d) overall weights.

## 8.0 ERGODIC HAZARD RESULTS

Using the suite of common-form crustal models, mean ergodic uniform-hazard spectra are calculated for hypothetical Auckland, Wellington and Christchurch rock sites using the OpenQuake Engine. For Auckland and Wellington, the mean hazard spectra for the models derived in this study have a total of 153 branches (17 crustal median models, three crustal  $\tau$  models, three subduction interface models one seismic source model) using the 2010 NSHM seismic source model. For Christchurch, the Van Houtte and Abbott (2019) version of the Canterbury Seismic Hazard Model source model also has nine branches, so the mean hazard spectra are derived from 1,377 separate branches. The subduction interface models consist of the three “upper”, “central” and “lower” variants of the Abrahamson et al. (2018) model.

The uniform hazard spectra calculated using these ground-motion characterisation models are compared to mean hazard spectra calculated using the seed models with equal weights and compared to NZS1170.5:2004 code spectra in Figure 8.1. For Auckland, the common form models yield slightly higher uniform hazard spectra than the equally-weighted seed models. For Wellington, the differences are smaller because a large proportion of the hazard in Wellington is from the Hikurangi subduction interface, and both curves are underpinned by the same Abrahamson et al. (2018) subduction interface ground-motion models. For oscillator periods greater than 1 s, however, the uniform hazard spectrum from the common-form models is lower than the seed-model spectrum, which is a result of the prior weights providing lower hazard spectra than the data-driven weights. A more rigorous selection of the ‘weights on weights’ in Table 7.1 may yield more comparable long-period hazard spectra between the seed and common-form models. For Christchurch, the uniform hazard spectra have some differences, with the seed models yielding higher hazard at long oscillator periods and lower hazard at short oscillator periods. The hazard spectra for the common-form models are not smooth across oscillator periods because the model selection procedures are calculated without correlation across oscillator periods, and the weights are calculated using recorded data.

To assess the validity of the widely-applicable set of models derived using generic scenarios, Figure 8.2 shows the uniform hazard spectra for Auckland, Wellington and Christchurch calculated using the location-specific suite of models and the widely-applicable set of models. For Auckland and Wellington, the hazard spectra are relatively similar. For Christchurch, the models have some differences, likely due to the different data selection for the weighting schemes. The location-specific models have a more refined estimate of the epistemic uncertainty so are considered preferable where available.

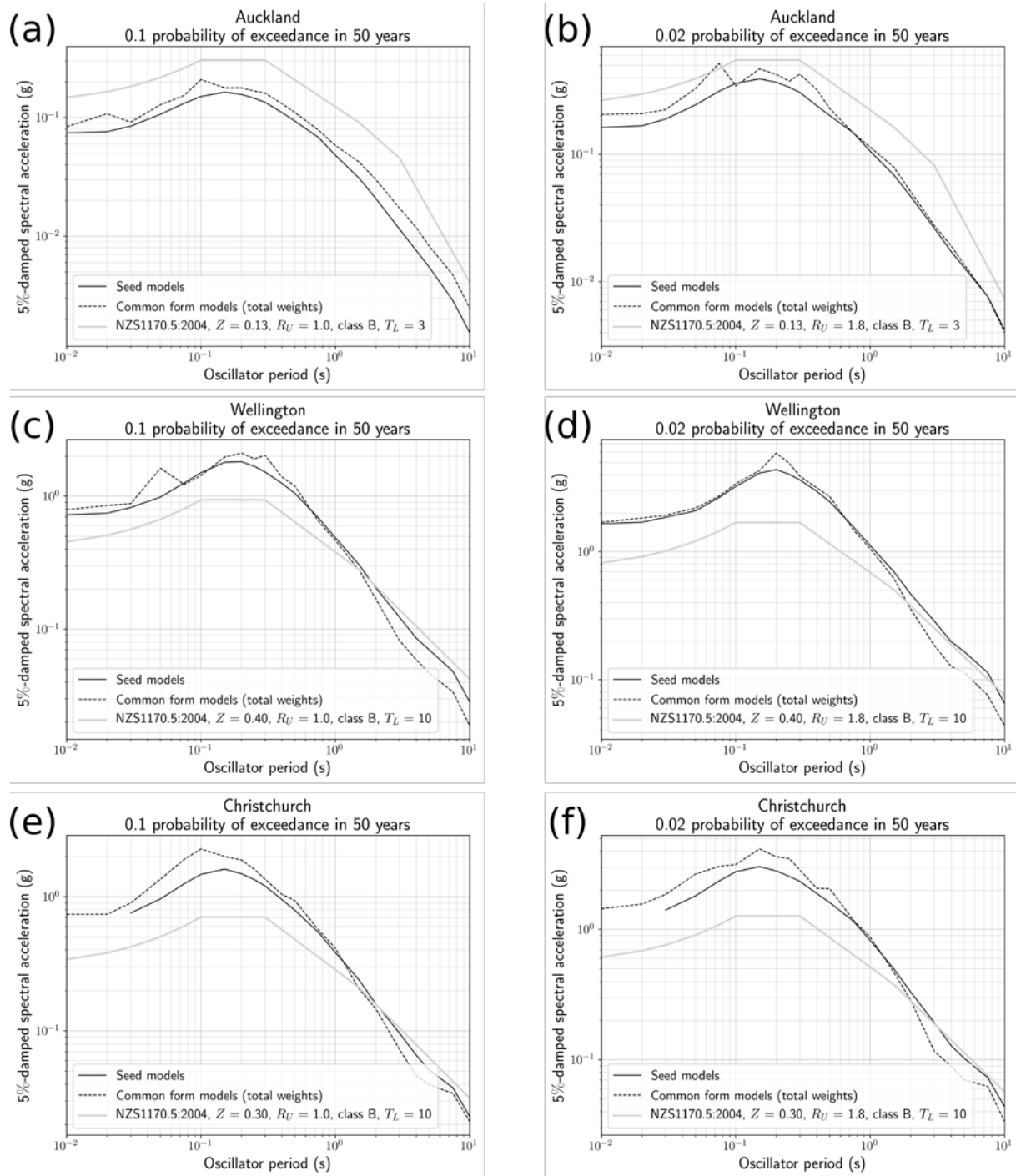


Figure 8.1 Uniform hazard spectra for generic rock sites in (a) and (b) Auckland, (c) and (d) Wellington and (e) and (f) Christchurch, determined using the seed models with the Al Atik and Youngs (2014) epistemic uncertainty model (solid black line) and Wellington-specific common-form models (dotted black line) relative to the NZS1170.5:2004 code spectra (solid grey lines). (a), (c) and (e) correspond to hazard spectra with 10% probability of exceedance in 50 years, while (b), (d) and (f) are for 2% probability of exceedance in 50 years.

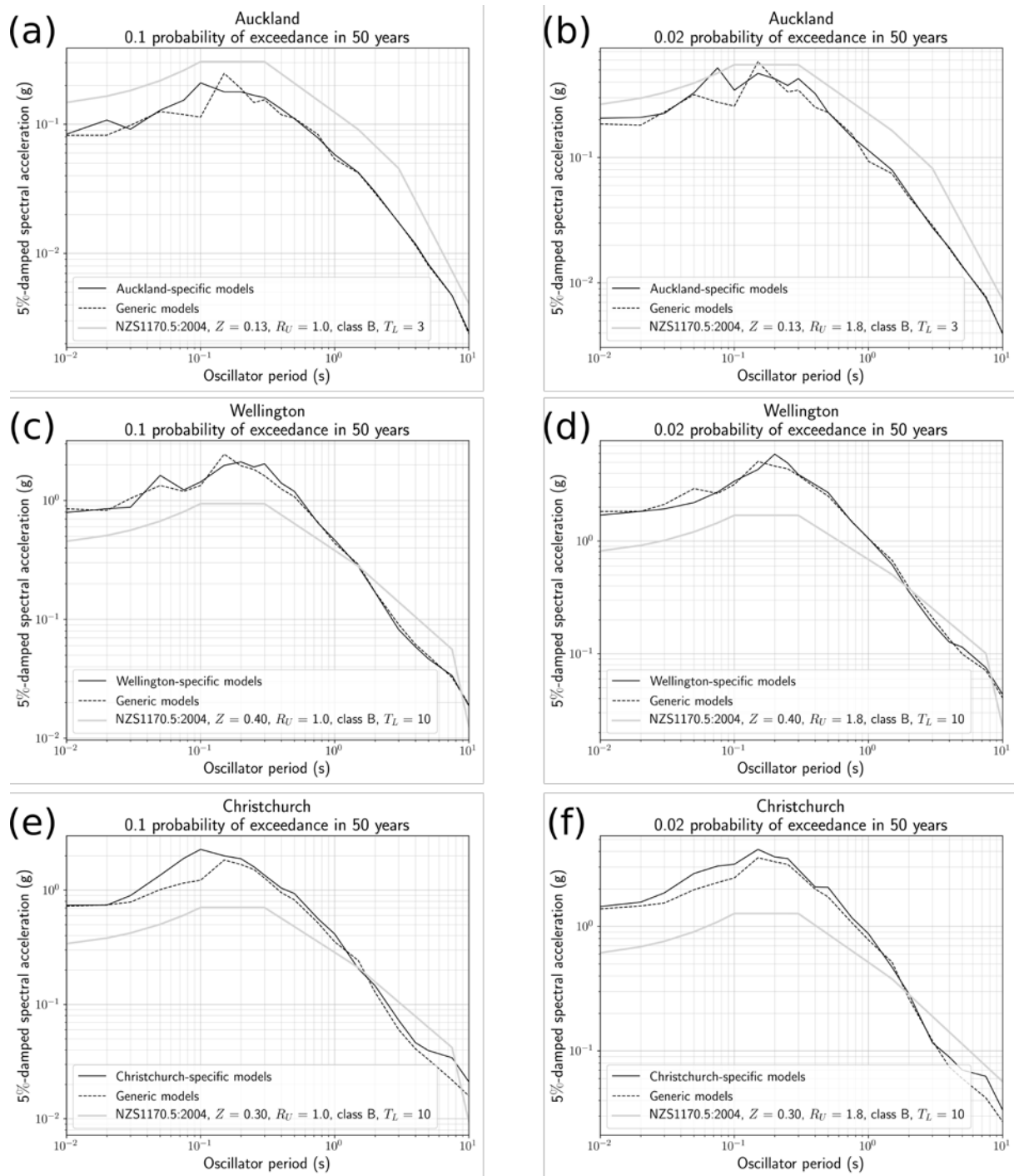


Figure 8.2 Uniform hazard spectra for generic rock sites in (a) and (b) Auckland, (c) and (d) Wellington and (e) and (f) Christchurch, determined using the location-specific common form models (solid black line) and suite of widely-applicable common-form models (dotted black line) relative to the NZS1170.5:2004 code spectra (solid grey lines). (a), (c) and (e) correspond to hazard spectra with 10% probability of exceedance in 50 years, while (b), (d) and (f) are for 2% probability of exceedance in 50 years.

## 9.0 PARTIALLY-ERGODIC HAZARD RESULTS

Partially-ergodic uniform-hazard spectra are calculated for six locations in Wellington and Christchurch using the models derived in this study. The Wellington- and Christchurch-specific set of models are utilised for each city. The mean hazard spectra for the Wellington results are a result the weighted mean from 459 possible logic tree branches (17 crustal median models, three crustal  $\tau$  models, three  $\delta S2S_s$  terms per site and three subduction interface models). The Christchurch results are the weighted mean of 4,131 possible branches, due to the nine branches of the seismic source model and are not presented for computational reasons. The partial removal of the ergodic assumption is currently only possible for the crustal models, so the hazard from the subduction interface is still ergodic. The partially-ergodic uniform hazard spectra for Wellington are compared to ergodic hazard spectra in Figure 9.1, Figure 9.2 and Figure 9.3. The  $\delta S2S_s$  terms from Figure 6.12 are repeated alongside the hazard spectra to facilitate the interpretation of the differences between the ergodic and partially-ergodic uniform hazard spectra.

The partially-ergodic hazard spectra can be higher or lower than the corresponding ergodic hazard spectra depending on the  $\delta S2S_s$  terms. For example, the  $\delta S2S_s$  terms for the WNAS site suggest that this site has smaller site amplification effects than indicated by the assigned  $V_{S30}$  and  $Z_1$  data in Kaiser et al. (2017). The partially-ergodic hazard spectra in Figure 9.1 are lower than the ergodic spectra except at around an oscillator period of 1 s, where the  $\delta S2S_s$  terms indicate a minor site amplification peak. At 1 s oscillator period, the partially-ergodic and ergodic hazard spectra are nearly equal. At the VUWS site, on the other hand, the  $\delta S2S_s$  terms indicate a broadband amplification in site response at short oscillator periods, relative to the assigned  $V_{S30}$  and  $Z_1$  values. The resultant partially-ergodic hazard spectra are higher than the corresponding ergodic hazard spectra across a broad oscillator period range. The clearest example of the benefits of the partially-ergodic approach is TEPS in Figure 9.3, with its strong, well-known site amplification at 1 s oscillator period. The partially-ergodic hazard spectra are higher than the ergodic hazard spectra around 1 s, but lower otherwise.

An interesting case for partially-ergodic hazard spectra is that of the rock site, POTS, in Figure 9.1. As a reference rock site for Wellington, one would expect the hazard spectra at this site to correspond to a benchmark rock hazard spectrum and Z factor for Wellington. The  $\delta S2S_s$  data indicate that site amplification effects are generally higher than what would be predicted by its assigned  $V_{S30}$  and  $Z_1$ , particularly at long periods. This may indicate that the full-basin amplification response in Wellington at 1–2 s also amplifies ground motion for rock sites outside the basin. The partially-ergodic hazard spectrum at 10% probability of exceedance in 50 years is substantially higher than its ergodic counterpart for periods greater than 1 s, but slightly lower at short periods. At short periods, however, both the partially-ergodic and ergodic hazard spectra are higher than the NZS1170.5:2004 code spectra. The ergodic hazard spectra indicate a Z factor of around 0.7, as defined as the rock PGA hazard, but the partially-ergodic approach indicates a  $Z \sim 0.6$ . Such analysis of Z can be misleading, however, as the class B code spectra for  $Z = 0.4$ , the current design standard, is quite close to the partially-ergodic one for oscillator periods greater than 1 s. Changes to the Z factor are unlikely to resolve issues with the code spectra in Wellington, and a wholesale redefinition of the code spectral shapes appears to be necessary. Additionally, partially-ergodic hazard calculations can either be derived using recorded data, as in this report, or using simulated data from ground-response analysis relative to reference rock spectra. For Wellington, the POTS partially-ergodic hazard spectra represent a starting point for such ground-response analyses, which assists the calculation of partially-ergodic hazard at any site in Wellington, not just at a GeoNet recording site.

Note that a large part of these ‘partially-ergodic’ hazard results are made up of an ergodic hazard contribution from the Hikurangi subduction interface. It is expected that the differences between ergodic and partially-ergodic hazard spectra will become more pronounced should partially-ergodic subduction interface predictions be incorporated in the future. For example, the 1 s peak for the TEPS site in Figure 9.3 would likely become more pronounced. This issue is discussed in more detail in section 10.3.1.

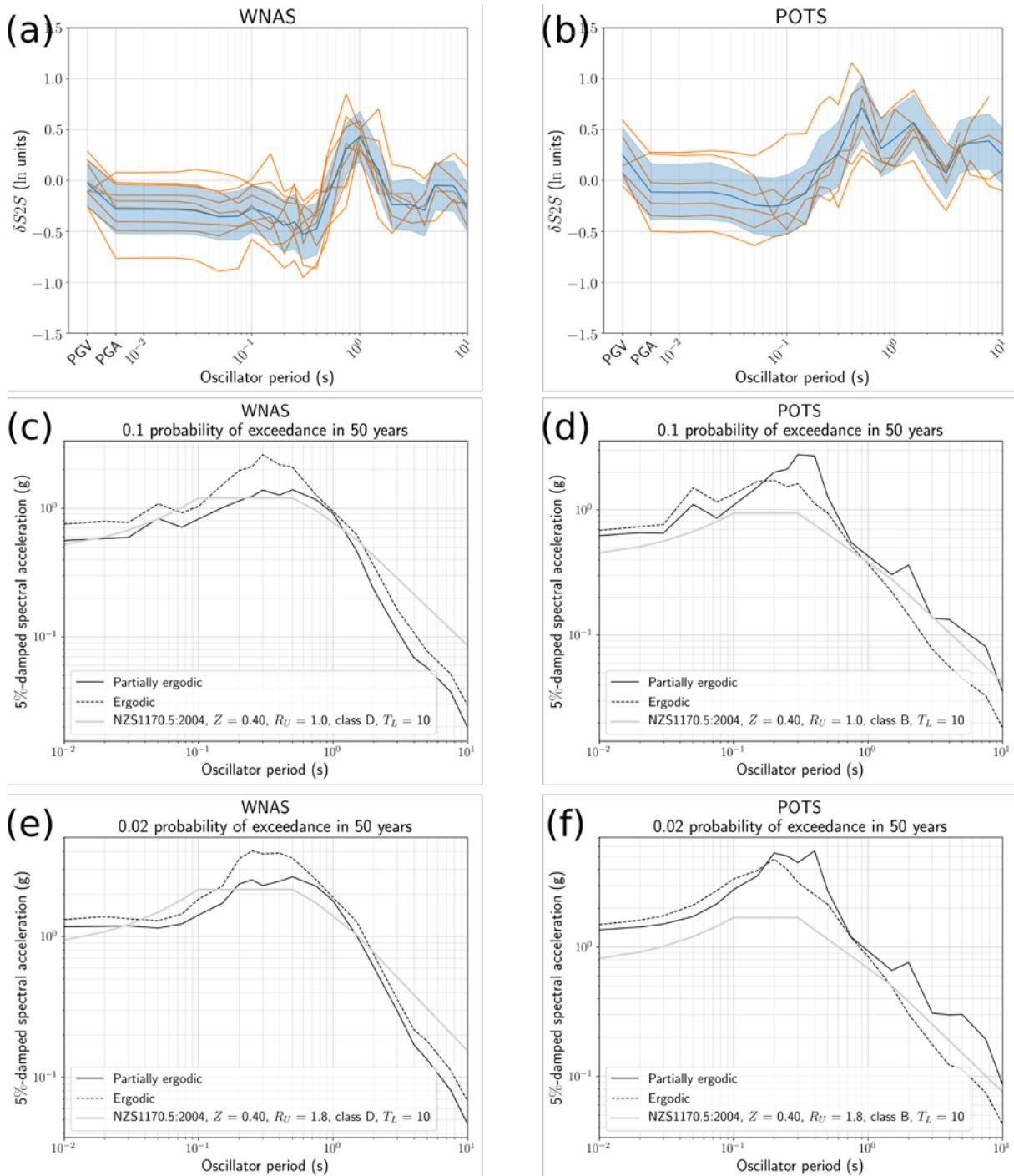


Figure 9.1 Partially-ergodic hazard results for the WNAS and POTS sites. (a) and (b) show the  $\delta S2S_s$  terms derived in Section 6.4, (c) and (d) show the uniform hazard spectra for 10% probability of exceedance in 50 years, and (e) and (f) show the uniform hazard spectra with 2% probability of exceedance in 50 years.

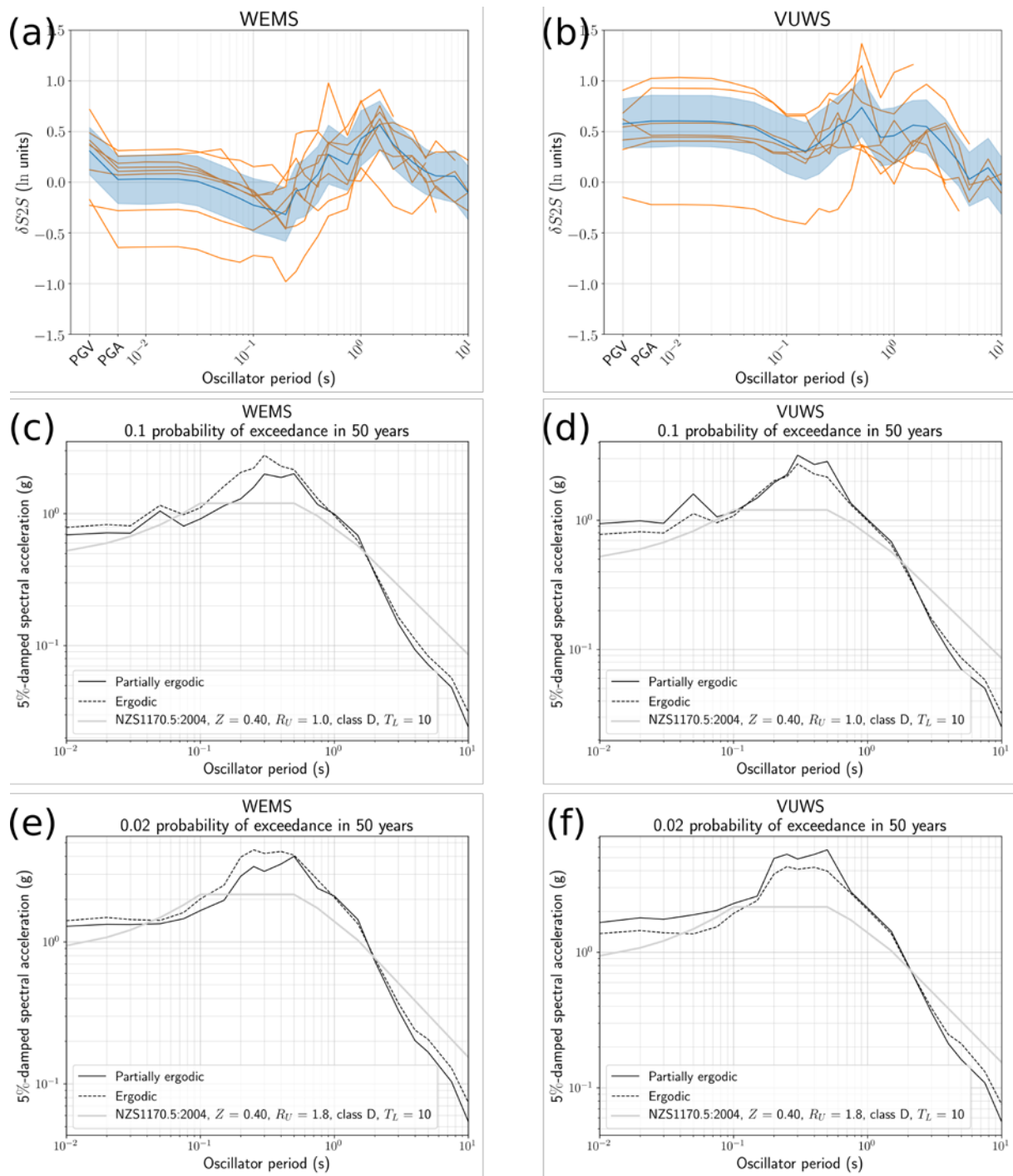


Figure 9.2 Partially-ergodic hazard results for the WEMS and VUWS sites. (a) and (b) show the  $\delta S2S_s$  terms derived in Section 6.4, (c) and (d) show the uniform hazard spectra for 10% probability of exceedance in 50 years, and (e) and (f) show the uniform hazard spectra with 2% probability of exceedance in 50 years.

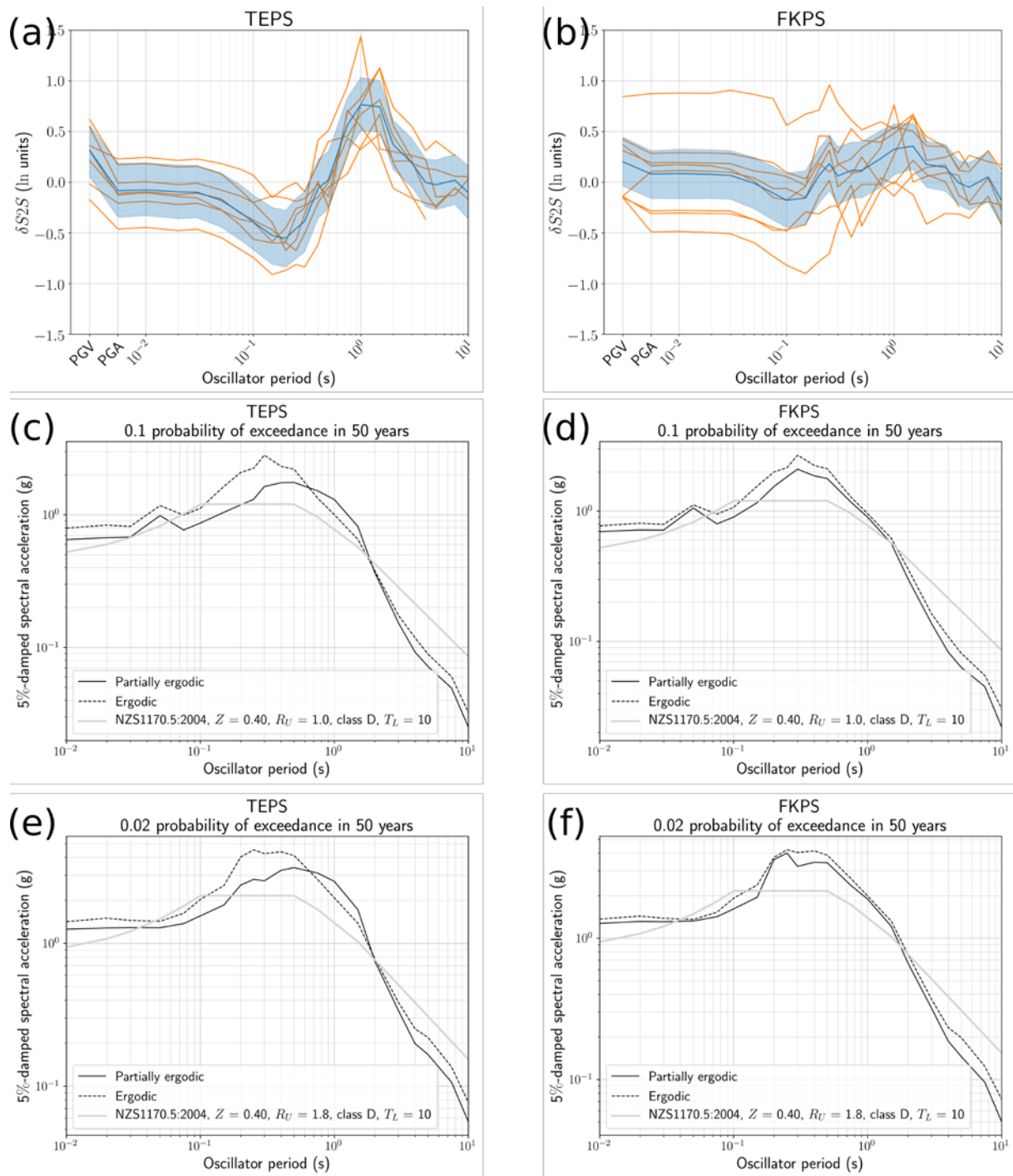


Figure 9.3 Partially-ergodic hazard results for the TEPS and FKPS sites. (a) and (b) show the  $\delta S2S_s$  terms derived in Section 6.4, (c) and (d) show the uniform hazard spectra for 10% probability of exceedance in 50 years, and (e) and (f) show the uniform hazard spectra with 2% probability of exceedance in 50 years.

## 10.0 DISCUSSION AND FUTURE WORK

### 10.1 Use of These Crustal Models

Using the models derived in this study, the ergodic seismic hazard has been calculated for reference rock sites in Auckland, Wellington, and Christchurch, and partially-ergodic seismic hazard has been calculated at six GeoNet stations in Wellington. In New Zealand, it is very rare for seismic hazard analysts to deviate from the ergodic assumption, even when calculating site-specific hazard at soil sites. Site response is often represented using generic, global site terms based on  $V_{S30}$  and  $Z_1$ . The pitfalls of this approach are clear in Wellington, where these generic terms are in significant error for most locations in the Central Business District.

While the models here include a linear and nonlinear site response model and can technically be used to calculate ergodic hazard spectra at any site by assigning  $V_{S30}$  and  $Z_1$ , in the author's opinion this procedure should no longer be permissible for site-specific hazard analysis in New Zealand for engineering design. To utilise these models in site-specific studies, the seismic hazard should be calculated for a reference rock condition, and the site-specific amplification should either be quantified with simulations or recorded data. The rock hazard and site-specific response should then be combined to obtain the site-specific hazard. This procedure is very common outside of New Zealand and is the recommended use case for the models in this study.

### 10.2 Subduction Interface Models

The largest uncertainty in New Zealand seismic hazard analysis is likely to come from the Hikurangi subduction zone, both in terms of the magnitude-frequency distributions of events and the ground-motion modelling. The models derived in this study cannot be used for subduction interface events, as ground-motion for subduction interface events often have different scaling characteristics. To capture the epistemic uncertainty in empirical subduction interface ground-motion models, a set of different seed models are required. Unfortunately, there are too few subduction zone seed models to derive a common-form model with a meaningful parameter covariance matrix. Many new subduction interface models may soon be available through the NGA-Subduction project (e.g. Kishida et al. 2018), after which a similar analysis to what is detailed in this report can be undertaken for subduction interface models too. The analysis of epistemic uncertainty in ground-motion prediction for New Zealand seismic hazard analysis is not complete until a representative suite of models is derived for subduction zone earthquakes as well as shallow crustal earthquakes.

### 10.3 Further Development on Ergodic Assumption Removal

#### 10.3.1 $\delta S2S_s$ Terms for Both Crustal and Subduction Zone Models

Partial removal of the ergodic assumption is clearly the future of empirical ground-motion modelling for seismic hazard analysis. This is particularly the case for site-specific analyses, but likely also for hazard mapping. Currently, the consideration of site-specific data is only possible for shallow crustal ground-motion models, as no subduction interface data are available to derive site terms. The equivalence between response spectral site terms for shallow crustal and subduction interface hasn't yet been well studied and requires further work. Several studies have demonstrated that linear site terms for response spectral models are magnitude and distance dependent (Zhang and Zhao, 2009; Zhao et al. 2009; Stafford et al. 2017), which is an important issue considering the typically large magnitude of subduction interface events.

Zhao et al. (2015), however, derived site models using data from both shallow crustal events and subduction interface events, with any differences in site response between shallow crustal and subduction interface earthquakes captured in the site model's magnitude scaling. Both the Zhao et al. (2016b) shallow crustal model and the Zhao et al. (2016a) subduction interface model utilise the same Zhao et al. (2015) site model. If a magnitude-dependent site model that is common to both subduction interface and shallow crustal models, as modelled by Zhao et al. (2015), can be justifiably adopted, then the  $\delta S2S_s$  determined from crustal data can also be utilised in subduction interface models. The benefits will be large in Wellington, for example, where the Hikurangi subduction interface is a seismic source of great significance.

### 10.3.2 Hazard Maps Using Partially-Ergodic Hazard Analyses

The partially-ergodic seismic hazard results in this study are confined to GeoNet station locations, as the site-specific modifications require recorded ground-motion data. Landwehr et al. (2016) and Kuehn et al. (2019) have demonstrated that it is also possible to derive ground-motion models for calculating nonergodic hazard maps, by deriving models with spatially-varying coefficients. Both studies showed that such models are an improvement upon a typical ergodic-type model and do not overfit the data, at least in an overall sense. Abrahamson et al. (2019) combined the approaches of these two studies to calculate the first fully nonergodic seismic hazard analysis with epistemic uncertainty. These approaches have shown aleatory variability can be reduced by 30–40%, similar to the reductions provided by the CyberShake method when good-quality velocity models are available, yet the epistemic uncertainties are more quantifiable than those from the Cybershake method. These models continuously transition between nonergodic seismic hazard analysis where data are available, and ergodic seismic hazard analysis where there are none. While implementing these models is very difficult within current seismic hazard modelling codes, and the computational burden will be very high, these models could be a promising approach for the near future. If such models are derived for New Zealand, they could be combined using a similar approach in this study to derive nonergodic hazard maps that fully consider epistemic uncertainty in ground-motion prediction.

### 10.4 Epistemic Uncertainty in Hanging Wall Effects

In the models derived in this study, no epistemic uncertainty is applied in the modelling of hanging wall effects or site response, with both terms taken directly from the Abrahamson et al. (2014) model. The lack of uncertainty in site response is not too problematic if site-specific site-response modelling is used in the context of partially-ergodic hazard calculations. For ergodic hazard calculations, site response modelling will need more detailed consideration than what is applied here, but it is the author's opinion that ergodic site response modelling provides misleading results, particularly in Wellington, and should no longer be utilised for site-specific seismic hazard assessment in New Zealand.

Hanging wall effects, however, do have large epistemic uncertainty that need further consideration if seismic sources in the near-field significantly influence a site's seismic hazard. In those instances, a 'hanging wall logic tree' should be developed with different models. Currently few such models exist. Modern hanging wall models are based on the work of Donahue and Abrahamson (2014), who derived simulated data using the Graves and Pitarka (2010) rupture generator, with 1D Greens functions, on the SCEC Broadband Platform (Maechling et al, 2014). Simulated data can be modelled in many different ways, and Withers et al. (2019a) for example, do not observe a strong hanging wall

effect when fault zone plasticity is modelled to simulated data. Additional models on different datasets would help to better model epistemic uncertainty in the hanging wall effect.

## 10.5 Consideration of Simulated Data

In recent years, a great deal of research effort has been directed towards semi-physical, semi-empirical ground-motion simulations. The most widely discussed method for incorporating simulated data into seismic hazard maps is through the CyberShake methodology (Graves et al. 2011). Some difficulties associated with the CyberShake methodology are its limitation to simple seismic source models due to computation issues, the limited scientific understanding of source parameters and their covariances, the lack of consideration of epistemic uncertainty in simulation method, and pragmatic difficulties in combining hazard results from different software.

The latter issue can be addressed using the models derived in this study. Simulated data can still provide valuable information for better constraining the seismic hazard. The models derived in this study can be compared to simulated data in much the same way as they are compared to recorded data in Section 7.2. Weights can be assigned to the common form models based on which locations on the Sammon’s map represent the same ground-motion values as the simulated data. These weights can then be incorporated into the overall hazard calculations using the “weights on weights” approach, i.e. equation (7.5) can be rewritten as

$$w_{overall} = a \times w_{prior} + b \times (c \times w_{\delta B_e, data} + d \times w_{LL, data}) + f \times (g \times w_{\delta B_e, sim} + h \times w_{LL, sim}) \quad (10.1)$$

or similar. In this manner, simulated data can be used to tune the model weights, rather than forming part of the hazard calculations. This solution improves transparency by allowing the empirical evidence and simulated data to be clearly visualised, allows hazard calculations to be performed in a single step using a single seismic hazard software, and facilitates gradual uptake of simulated data by altering the “weights on weights” i.e. the ratio  $b / f$  in equation (10.1).

## 10.6 Sensitivity Studies

Numerous assumptions are required to derive a suite of common form models, for example the definition of the common-form equation, the seed model selection, the method of dimensionality reduction and the method for selecting models from the lower-dimensional ground-motion representation. Before the method outlined in this study can be used in PSHA applications, a large-scale sensitivity study needs to be conducted.

## 11.0 ACKNOWLEDGMENTS

This project was funded by EQC Biennial grant number 16/720. The EQC is gratefully acknowledged for allowing the project to be deferred two years while the author took a temporary research position in the United States. David Rhoades and Matt Gerstenberger are acknowledged for helpful discussions and reviews.

## 12.0 REFERENCES

- Abrahamson N. 2011. Review of “The Canterbury Earthquake Sequence and Implications for Seismic Design Levels” dated July 2011. Wellington (NZ): Canterbury Earthquakes Royal Commission; [accessed 2020 Mar]. [https://canterbury.royalcommission.govt.nz/documents-by-key/20111011.156/\\$File/SEI.ABR.0001.pdf](https://canterbury.royalcommission.govt.nz/documents-by-key/20111011.156/$File/SEI.ABR.0001.pdf).
- Abrahamson NA, Youngs RR. 1992. A stable algorithm for regression analyses using the random effects model. *Bulletin of the Seismological Society of America*. 82(1):505–510.
- Abrahamson NA, Silva WJ, Kamai R. 2014. Summary of the ASK14 ground motion relation for active crustal regions. *Earthquake Spectra*. 30(3):1025–1055. doi:10.1193/070913eqs198m.
- Abrahamson N, Gregor N, Addo K. 2016. BC Hydro ground motion prediction equations for subduction earthquakes. *Earthquake Spectra*. 32(1):23–44. doi:10.1193/051712eqs188mr.
- Abrahamson N, Kuehn N, Gulerce Z, Gregor N, Bozorgnia Y, Parker G, Stewart J, Chiou B, Idriss I, Campbell K, et al. 2018. Update of the BC Hydro subduction ground-motion model using the NGA-Subduction dataset. Berkeley (USA): Pacific Earthquake Engineering Research Center. PEER Report 2018/02.
- Abrahamson N, Kuehn N, Walling M, Landwehr N. 2019. Probabilistic seismic hazard analysis in California using nonergodic ground-motion models. *Bulletin of the Seismological Society of America*. 109(4):1235–1249. doi:10.1785/0120190030.
- Akkar S, Sandikkaya MA, Bommer JJ. 2014. Empirical ground-motion models for point- and extended-source crustal earthquake scenarios in Europe and the Middle East. *Bulletin of Earthquake Engineering*. 12(1):359–387. doi:10.1007/s10518-013-9461-4.
- Al Atik L, Abrahamson N, Bommer J, Scherbaum F, Cotton F, Kuehn N. 2010. The variability of ground-motion prediction models and its components. *Seismological Research Letters*. 81(5):794–801. doi:10.1785/gssrl.81.5.794.
- Al Atik L, Youngs R. 2014. Epistemic uncertainty for NGA-West2 models. *Earthquake Spectra*. 30(3):1301–1318. doi:10.1193/062813EQS173M.
- Al Atik L. 2015. NGA-East: Ground-motion standard deviation models for Central and Eastern North America. Berkeley (USA): Pacific Earthquake Engineering Research Center. Report 2015/07.
- Anderson JG, Brune JN. 1999. Probabilistic seismic hazard analysis without the ergodic assumption. *Seismological Research Letters*. 70(1):19–28. doi:10.1785/gssrl.70.1.19.
- Atkinson G. 2006. Single station sigma. *Bulletin of the Seismological Society of America*. 96(2):446–455. doi:10.1785/0120050137.
- Bommer J, Scherbaum F. 2008. The use and misuse of logic trees in probabilistic seismic hazard assessment. *Earthquake Spectra*. 24(4):997–1009. doi:10.1193/1.2977755.
- Boore D. 2010. Orientation-independent, nongeometric-mean measures of seismic intensity from two horizontal components of motion. *Bulletin of the Seismological Society of America*. 100(4):1830–1835. doi:10.1785/0120090400.

- Boore D, Stewart J, Seyhan E, Atkinson G. 2014. NGA-West2 equations for predicting PGA, PGV, and 5% damped PSA for shallow crustal earthquakes. *Earthquake Spectra*. 30(3):1057–1085. doi:10.1193/070113EQS184M.
- Boore D, Kishida T. 2017. Relations between some horizontal–component ground–motion intensity measures used in practice. *Bulletin of the Seismological Society of America*. 107(1):334–343. doi:10.1785/0120160250.
- Bradley BA. 2013. A New Zealand–specific pseudospectral acceleration ground–motion prediction equation for active shallow crustal earthquakes based on foreign models. *Bulletin of the Seismological Society of America*. 103(3):1801–1822. doi:10.1785/0120120021.
- Bradley BA. 2015. Systematic ground motion observations in the Canterbury earthquakes and region-specific non-ergodic empirical ground motion modeling. *Earthquake Spectra*. 31(3):1735–1761. doi:10.1193/053013EQS137M.
- Bradley BA, Wotherspoon LM, Kaiser AE, Cox BR, Jeong S. 2018. Influence of site effects on observed ground motions in the Wellington region from the  $M_w$ 7.8 Kaikōura, New Zealand, earthquake. *Bulletin of the Seismological Society of America*. 108(3B):1722–1735. doi:10.1785/0120170286.
- Campbell KW, Bozorgnia Y. 2014. NGA-West2 ground motion model for the average horizontal components of PGA, PGV, and 5% damped linear acceleration response spectra. *Earthquake Spectra*. 30(3):1087–1115. doi:10.1193/062913EQS175M.
- Carpenter B, Gelman A, Hoffman M, Lee D, Goodrich B, Betancourt M, Brubaker M, Guo J, Li P, Riddell A. 2017. Stan: a probabilistic programming language. *Journal of Statistical Software*. 76(1). doi:10.18637/jss.v076.i01.
- Cauzzi C, Faccioli E, Vanini M, Bianchini A. 2015. Updated predictive equations for broadband (0.01–10 s) horizontal response spectra and peak ground motions, based on a global dataset of digital acceleration records. *Bulletin of Earthquake Engineering*. 13(6):1587–1612. doi:10.1007/s10518-014-9685-y.
- Chiou B, Youngs R. 2014. Update of the Chiou and Youngs NGA Model for the average horizontal component of peak ground motion and response spectra. *Earthquake Spectra*. 30(3):1117–1153. doi:10.1193/072813EQS219M.
- Chiou B. 2015. GMPE space [abstract]. In: *SSA Annual Meeting announcement, Seismological Society of America technical sessions*; 2015 Apr 21–23; Pasadena, CA. Albany (CA): Seismological Society of America. (Seismological research letters; 86(2B)).
- Cornell CA. 1968. Engineering seismic risk analysis. *Bulletin of the Seismological Society of America*. 58(5):1583–1606.
- Donahue J, Abrahamson N. 2014. Simulation-based hanging wall effects. *Earthquake Spectra*. 30(3):1269–1284. doi:10.1193/071113EQS200M.
- Douglas J. 2003. Earthquake ground motion estimation using strong-motion records: a review of equations for the estimation of peak ground acceleration and response spectral ordinates. *Earth Science Reviews*. 61(1-2):43–104. doi:10.1016/S0012-8252(02)00112-5.
- Douglas J, Edwards B. 2016. Recent and future developments in earthquake ground motion estimation. *Earth Science Reviews*. 160:203–219. doi:10.1016/j.earscirev.2016.07.005.
- Faccioli E, Paolucci R, Vanini M. 2015. Evaluation of probabilistic site-specific seismic-hazard methods and associated uncertainties, with applications in the Po Plain, Northern Italy. *Bulletin of the Seismological Society of America*. 105(5):2787–2807. doi:10.1785/0120150051.

- Gelman A, Rubin DB. 1992. Inference from iterative simulation using multiple sequences. *Statistical Science*. 7(4):457–472. doi:10.1214/ss/1177011136.
- Gerstenberger M, McVerry G, Rhoades D, Stirling M. 2014. Seismic hazard modelling for the recovery of Christchurch. *Earthquake Spectra*. 30(1):17–29. doi:10.1193/021913EQS037M.
- Gerstenberger M, Rhoades D, McVerry G. 2016. A hybrid time-dependent probabilistic seismic hazard model for Canterbury, New Zealand. *Seismological Research Letters*. 87(6):1311–1318. doi:10.1785/0220160084.
- Goulet C, Bozorgnia Y, Abrahamson N, Kuehn N, Al Atik L, Youngs R, Graves R, Atkinson G. 2018. Central and Eastern North America ground-motion characterization - NGA-East final report. Berkeley (CA): Pacific Earthquake Engineering Research Center. Report 2018/08.
- Graves R, Pitarka A. 2010. Broadband ground-motion simulation using a hybrid approach. *Bulletin of the Seismological Society of America*. 100(5A):2095–2123. doi:10.1785/0120100057.
- Graves R, Jordan T, Callaghan S, Deelman E, Field E, Juve G, Kesselman C, Maechling P, Mehta G, Milner K, Okaya D, Small P, Vahi K. 2011. CyberShake: a physics-based seismic hazard model for Southern California. *Pure and Applied Geophysics*. 168(3-4):367–381. doi:10.1007/s00024-010-0161-6.
- Holden C, Kaiser A, Van Dissen R, Jury R. 2013. Sources, ground motion and structural response characteristics in Wellington of the 2013 Cook Strait earthquakes. *Bulletin of the New Zealand Society of Earthquake Engineering*. 46(4):188–195.
- Idriss I. 2014. An NGA-West2 empirical model for estimating the horizontal spectral values generated by shallow crustal earthquakes. *Earthquake Spectra*. 30(3):1155–1177. doi:10.1193/070613EQS195M.
- Imtiaz A, Causse M, Chaljub E, Cotton F. 2015. Is the ground-motion distance dependent? Insight from finite-source rupture simulations. *Bulletin of the Seismological Society of America*. 105(2A):950–962. doi:10.1785/0120140107.
- Kaiser A, Van Houtte C, Perrin N, Wotherspoon L, McVerry G. 2017. Site characterisation of GeoNet stations for the New Zealand strong motion database. *Bulletin of the New Zealand Society of Earthquake Engineering*. 50(1):39–49.
- Kale O, Akkar S, Ansari A, Hamzehloo H. 2015. A Ground-Motion Predictive Model for Iran and Turkey for Horizontal PGA, PGV, and 5% Damped Response Spectrum: Investigation of Possible Regional Effects. *Bulletin of the Seismological Society of America*. 105(2A):963–980. doi:10.1785/0120140134.
- Kishida T, Contreras V, Bozorgnia Y, Abrahamson N, Ahdi S, Ancheta T, Boore D, Campbell K, Chiou B, Darragh R, Gregor N, Kuehn N et al. 2018. NGA-Sub ground motion database. [In]: *Proceedings of the 11th National Conference in Earthquake Engineering*; 2018 Jun 25–28; Los Angeles, CA: Earthquake Engineering Research Institute.
- Kotha S, Bindi D, Cotton F. 2015. Partially non-ergodic region specific GMPE for Europe and Middle-East. *Bulletin of Earthquake Engineering*. 14(4):1245–1263. doi:10.1007/s10518-016-9940-5.
- Kotha S, Bindi D, Cotton F. 2017. From ergodic to region- and site-specific probabilistic seismic hazard assessment: method development and application at European and Middle Eastern sites. *Earthquake Spectra*. 33(4):1433–1453. doi:10.1193/081016EQS130M.
- Kuehn N, Abrahamson N. 2015. Selecting and weighting of GMPEs for PSHA based on high-dimensional visualisation tools [abstract]. In: *SSA Annual Meeting announcement, Seismological Society of America technical sessions*; 2015 Apr 23–25; Pasadena, CA. Albany (CA): Seismological Society of America. (Seismological research letters; 86(2B)).

- Kuehn NM, Abrahamson NA. 2018. The effect of uncertainty in predictor variables on the estimation of ground-motion prediction equations. *Bulletin of the Seismological Society of America*. 108(1):358–370. doi:10.1785/0120170166.
- Kuehn NM, Abrahamson NA, Walling MA. 2019. Incorporating nonergodic path effects into the NGA-West2 ground-motion prediction equations. *Bulletin of the Seismological Society of America*. 109(2):575–585. doi:10.1785/0120180260.
- Landwehr N, Kuehn N, Scheffer T, Abrahamson N. 2016. A nonergodic ground-motion model for California with spatially varying coefficients. *Bulletin of the Seismological Society of America*. 106(6):2574–2583. doi:10.1785/0120160118.
- Lin P-S. 2009. Ground-motion attenuation relationship and path-effect study using Taiwan data set [PhD thesis]. Taoyuan City (TW): National Central University. [Chinese].
- Maechling PJ, Silva F, Callaghan S, Jordan TH. 2014. SCEC Broadband Platform: system architecture and software implementation. *Seismological Research Letters*. 86(1):27–38. doi:10.1785/0220140125.
- Mai PM, Spudich P, Boatwright J. 2005. Hypocenter locations in finite-source rupture models. *Bulletin of the Seismological Society of America*. 95(3):965–980. doi:10.1785/0120040111.
- Mak S, Clements R, Schorlemmer D. 2017. Empirical evaluation of hierarchical ground-motion models: score uncertainty and model weighting. *Bulletin of the Seismological Society of America*. 107(2):949–965. doi:10.1785/0120160232.
- Manighetti I, Campillo M, Bouley S, Cotton F. 2007. Earthquake scaling, fault segmentation, and structural maturity. *Earth and Planetary Science Letters*. 253(3-4):429–438. doi:10.1016/j.epsl.2006.11.004.
- McVerry G, Zhao J, Abrahamson N, Somerville P. 2006. New Zealand acceleration response spectrum attenuation relations for crustal and subduction zone earthquakes. *Bulletin of the New Zealand Society for Earthquake Engineering*. 39(1):1–58.
- Melgar D, Hayes G. 2019. The correlation lengths and hypocentral locations in great earthquakes. *Bulletin of the Seismological Society of America*. 109(6):2582–2593. doi:10.1785/0120190164.
- Molkenthin C, Scherbaum F, Griewank A, Kuehn N, Stafford P. 2014. A study on the sensitivity of response spectral amplitudes on seismological parameters using algorithmic differentiation. *Bulletin of the Seismological Society of America*. 104(5):2240–2252. doi:10.1785/0120140022.
- Morikawa N, Fujiwara H. 2013. A new ground motion prediction equation for Japan applicable up to M9 mega-earthquake. *Journal of Disaster Research*. 8(5):878–888. doi:10.20965/jdr.2013.p0878.
- Pagani M, Monelli D, Weatherill G, Danciu L, Crowley H, Silva V, Henshaw P, Butler L, Nastasi M, Panzeri L, et al. 2014. OpenQuake Engine: an open hazard (and risk) software for the Global Earthquake Model. *Seismological Research Letters*. 85(3):692–702. doi:10.1785/0220130087.
- Phung V-B, Loh C-H, Cha S-H, Abrahamson N. 2019. Analysis of epistemic uncertainty associated with GMPEs and their weight within the logic tree for PSHA: Application to Taiwan. *Terrestrial, Atmospheric and Oceanic Sciences*. 29(6):611–633. doi:10.3319/TAO.2018.08.13.01.
- Radiguet M, Cotton F, Manighetti I, Campillo M, Douglas J. 2009. Dependency of near-field ground motions on the structural maturity of the ruptured faults. *Bulletin of the Seismological Society of America*. 99(4):2572–2581. doi:10.1785/0120080340.

- Ren Y, Zhou Y, Wang H, Wen R. 2018. Source characteristics, site effects and path attenuation from spectral analysis of strong-motion recordings in the 2016 Kaikōura earthquake sequence. *Bulletin of the Seismological Society of America*. 108(3B):1757–1773. doi:10.1785/0120170290.
- Rhoades DA. 1997. Estimation of attenuation relations for strong-motion data allowing for individual earthquake magnitude uncertainties. *Bulletin of the Seismological Society of America*. 87(6):1674–1678.
- Rodriguez-Marek A, Rathje EM, Bommer JJ, Scherbaum F, Stafford PJ. 2013. Application of single-station sigma and site-response characterization in a probabilistic seismic-hazard analysis for a new nuclear site. *Bulletin of the Seismological Society of America*. 104(4):1601–1619. doi:10.1785/0120130196.
- Roten D, Olsen KB, Day SM, Cui Y, Fäh D. 2014. Expected seismic shaking in Los Angeles reduced by San Andreas fault zone plasticity. *Geophysical Research Letters*. 41(8):2769–2777. doi:10.1002/2014GL059411.
- Sammon J. 1969. A nonlinear mapping for data structure analysis. *IEEE Transactions on Computers*. C-18(5):401–409. doi:10.1109/t-c.1969.222678.
- Scherbaum F, Delavaud E, Riggelsen C. 2009. Model selection in seismic hazard analysis: an information-theoretic perspective. *Bulletin of the Seismological Society of America*. 99(6):3234–3247. doi:10.1785/0120080347.
- Scherbaum F, Kuehn NM, Ohrnberger M, Koehler A. 2010. Exploring the proximity of ground-motion models using high-dimensional visualization techniques. *Earthquake Spectra*. 26:1117–1138. doi:10.1193/1.3478697.
- Schmedes J, Archuleta RJ. 2008. Near-source ground-motion along strike-slip faults: insights into magnitude saturation of PGV and PGA. *Bulletin of the Seismological Society of America*. 98(5):2278–2290. doi:10.1785/0120070209.
- Silva V, Crowley H, Pagani M, Monelli D, Pinho R. 2014. Development of the OpenQuake engine, the Global Earthquake Model's open-source software for seismic risk assessment. *Natural Hazards*. 72(3):1409–1427. doi:10.1007/s11069-013-0618-x.
- Stafford PJ. 2014a. Crossed and nested mixed-effects approaches for enhanced model development and removal of the ergodic assumption in empirical ground-motion models. *Bulletin of the Seismological Society of America*. 104(2):702–719. doi:10.1785/0120130145.
- Stafford PJ. 2014b. Source-scaling relationships for the simulation of rupture geometry within probabilistic seismic-hazard analysis. *Bulletin of the Seismological Society of America*. 104(4):1620–1635. doi:10.1785/0120130224.
- Stafford PJ, Rodriguez-Marek A, Edwards B, Kruiver PP, Bommer JJ. 2017. Scenario dependence of linear site-effect factors for short-period response spectral ordinates. *Bulletin of the Seismological Society of America*. 107(6):2859–2872. doi:10.1785/0120170084.
- Standards New Zealand. 2004. Structural design actions. Part 5, Earthquake actions: New Zealand. Wellington (NZ): Standards New Zealand. 76 p. NZS 1170.5:2004.
- Stirling M, McVerry G, Gerstenberger M, Litchfield N, Van Dissen R, Berryman K, Barnes P, Wallace L, Villamor P, Langridge R, et al. 2012. National seismic hazard model for New Zealand: 2010 update. *Bulletin of the Seismological Society of America*. 102(4):1514–1542. doi:10.1785/0120110170.
- Van Houtte C. 2017a. Performance of response spectral models against New Zealand data. *Bulletin of the New Zealand Society of Earthquake Engineering*. 50(1):21–38.

- Van Houtte C. 2017b. Incorporating near-surface attenuation in empirical ground motion models [PhD thesis]. Auckland (NZ): University of Auckland. [236] leaves.
- Van Houtte C, Abbott E. 2019. OpenQuake implementation of the Canterbury Seismic Hazard Model. *Seismological Research Letters*. 90(6):2227–2235. doi:10.1785/0220190100.
- Van Houtte C, Bannister S, Holden C, Bourguignon S, McVerry G. 2017. The New Zealand strong motion database. *Bulletin of the New Zealand Society of Earthquake Engineering*. 50(1):1–20.
- Vyas JC, Mai PM, Galis M. 2016. Distance and azimuthal dependence of ground-motion variability for unilateral strike-slip ruptures. *Bulletin of the Seismological Society of America*. 106(4):1584–1599. doi:10.1785/0120150298.
- Withers KB, Olsen KB, Shi Z, Day SM. 2019a. Validation of deterministic broadband ground motion and variability from dynamic rupture simulations of buried thrust earthquakes. *Bulletin of the Seismological Society of America*. 109(1):212–229. doi:10.1785/0120180005.
- Withers KB, Olsen KB, Day SM, Shi Z. 2019b. Ground motion and intraevent variability from 3D deterministic broadband (0–7.5 Hz) simulations along a nonplanar strike-slip fault. *Bulletin of the Seismological Society of America*. 109(1):229–250. doi:10.1785/0120180006.
- Zhang J, Zhao JX. 2009. Response spectral amplification ratios from 1- and 2-dimensional nonlinear soil site models. *Soil Dynamics and Earthquake Engineering*. 29(3):563–573. doi:10.1016/j.soildyn.2008.06.006.
- Zhao JX, Zhang J, Irikura K. 2009. Side-effect of using response spectral amplification ratios for soil sites – variability and earthquake-magnitude and source-distance dependent amplification ratios for soil sites, *Soil Dynamics and Earthquake Engineering*. 29(9):1262–1273. doi:10.1016/j.soildyn.2009.02.005.
- Zhao JX, Hu J, Jiang F, Zhou J, Zhang Y, An X, Lu M, Rhoades DA. 2015. Nonlinear site models derived from 1D analyses for ground-motion prediction equations using site class as the site parameter. *Bulletin of the Seismological Society of America*. 105(4):2010–2022. doi:10.1785/0120150019.
- Zhao JX, Liang X, Jiang F, Xing H, Zhu M, Hou R, Zhang Y, Lan X, Rhoades DA, Irikura K, et al. 2016a. Ground-motion prediction equations for subduction interface earthquakes in Japan using site class and simple geometric attenuation functions. *Bulletin of the Seismological Society of America*. 106(4):1518–1534. doi:10.1785/0120150034.
- Zhao JX, Zhou S, Zhou J, Zhao C, Zhang H, Zhang Y, Gao P, Lan X, Rhoades D, Fukushima Y, et al. 2016b. Ground-motion prediction equations for shallow crustal and upper-mantle earthquakes in Japan using site class and simple geometric attenuation functions. *Bulletin of the Seismological Society of America*. 106(4):1552–1569. doi:10.1785/0120150063.

This page left intentionally blank

## **APPENDICES**

This page left intentionally blank.

## APPENDIX 1 WEIGHT CALCULATIONS FOR THE AUCKLAND-SPECIFIC MODELS

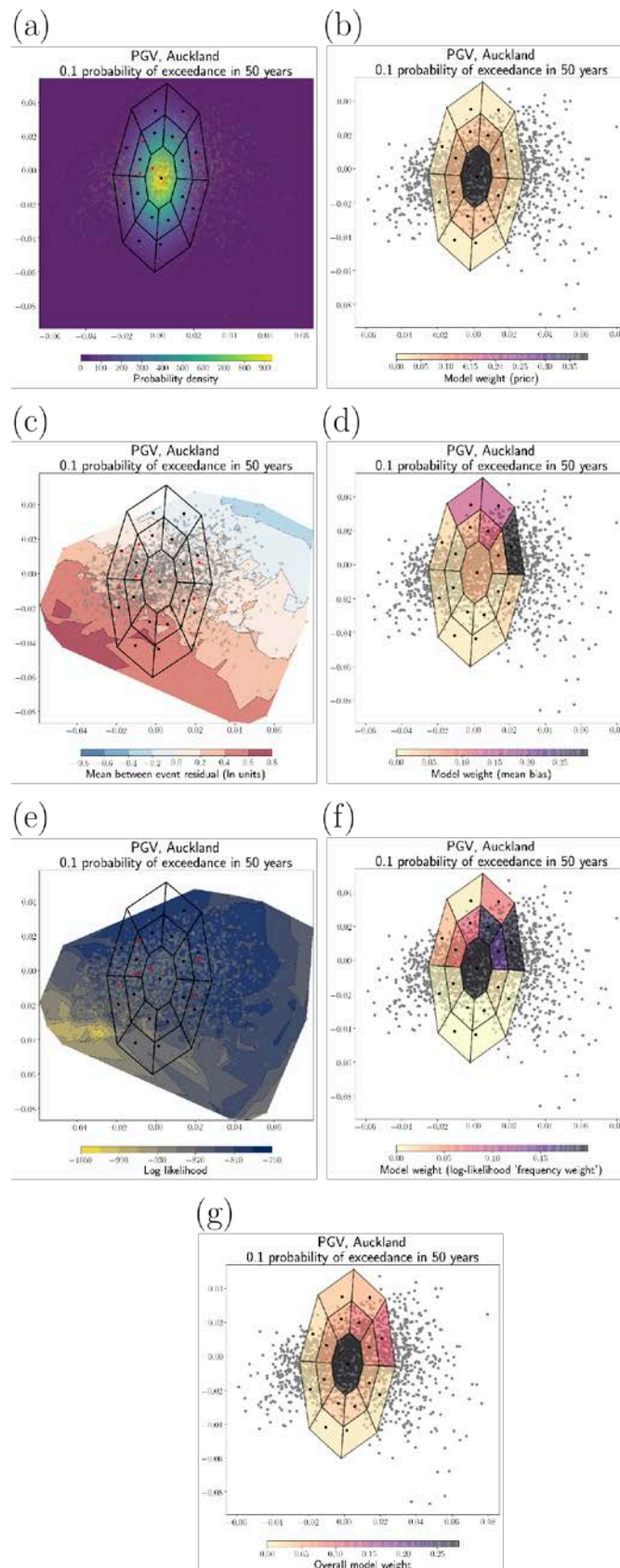


Figure A1.1 Weights for the Auckland suite of PGV models for 0.1 probability of exceedance in 50 years.

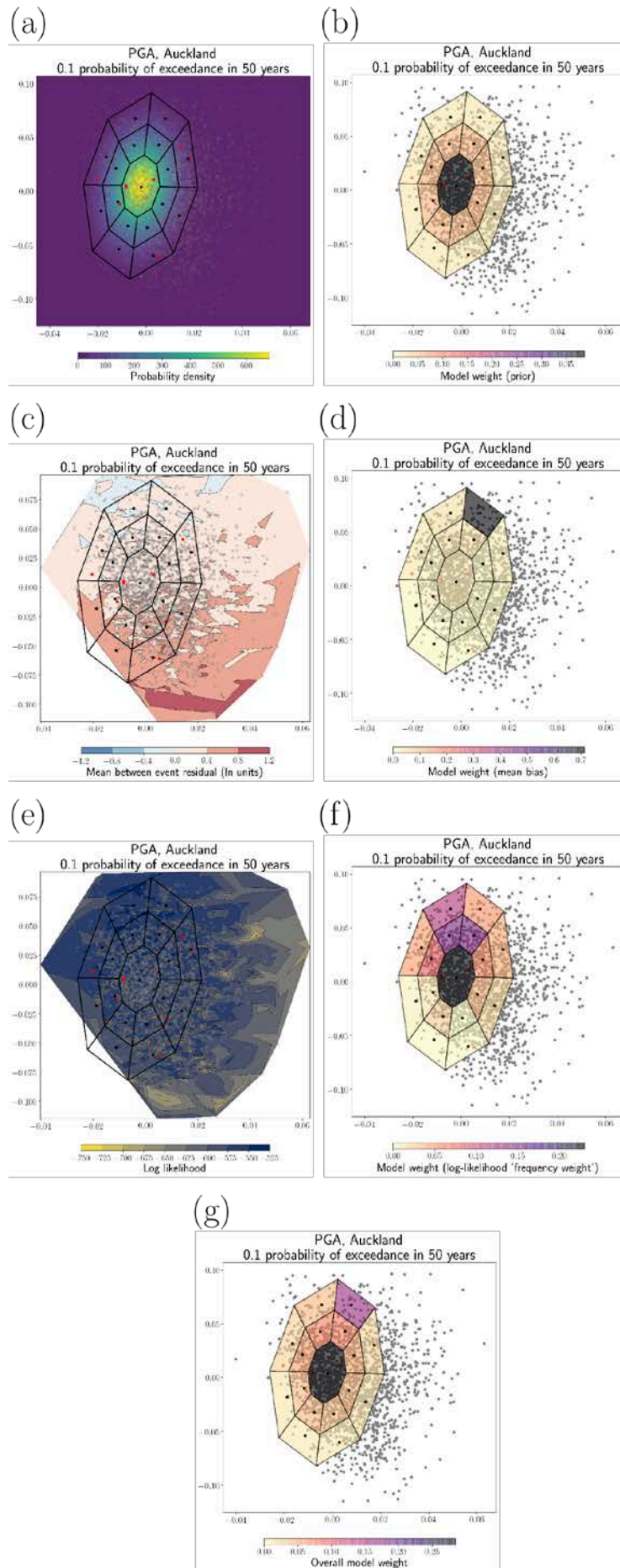


Figure A1.2 Weights for the Auckland suite of PGA models for 0.1 probability of exceedance in 50 years.

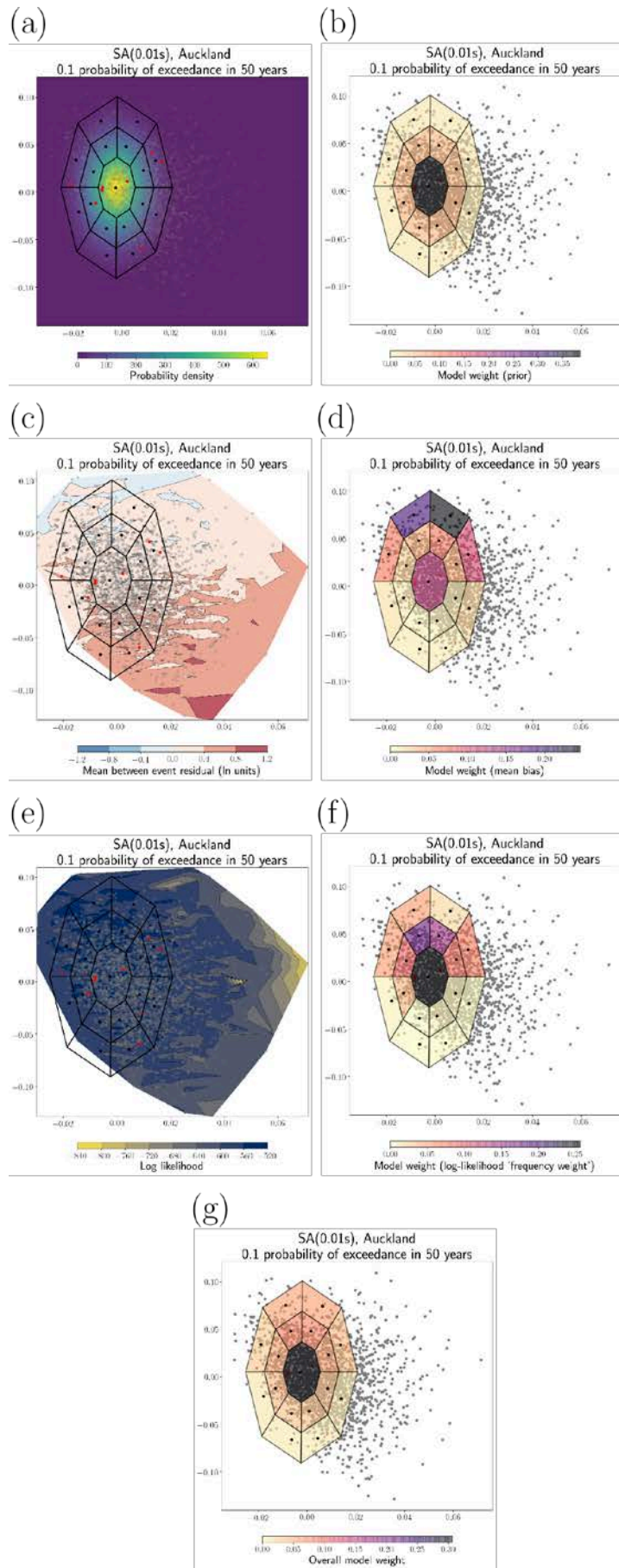


Figure A1.3 Weights for the Auckland suite of SA(0.01 s) models for 0.1 probability of exceedance in 50 years.

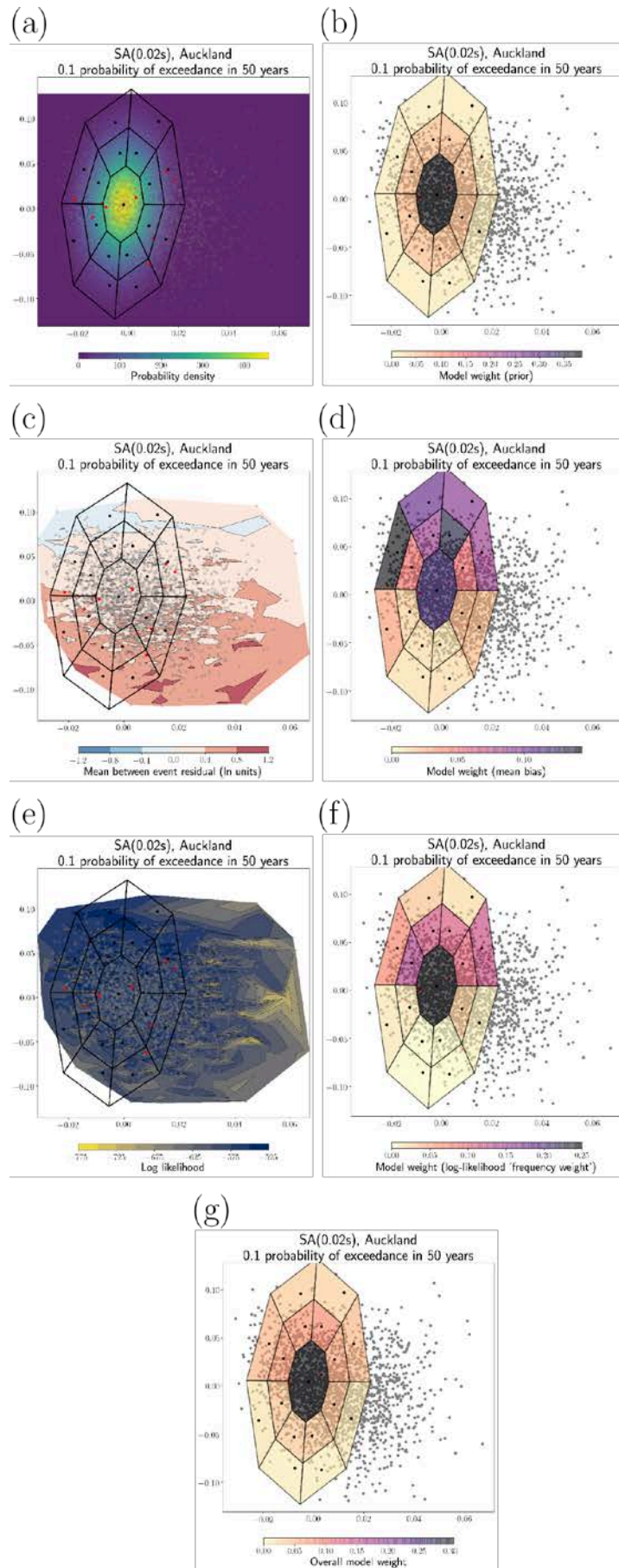


Figure A1.4 Weights for the Auckland suite of SA(0.02 s) models for 0.1 probability of exceedance in 50 years.

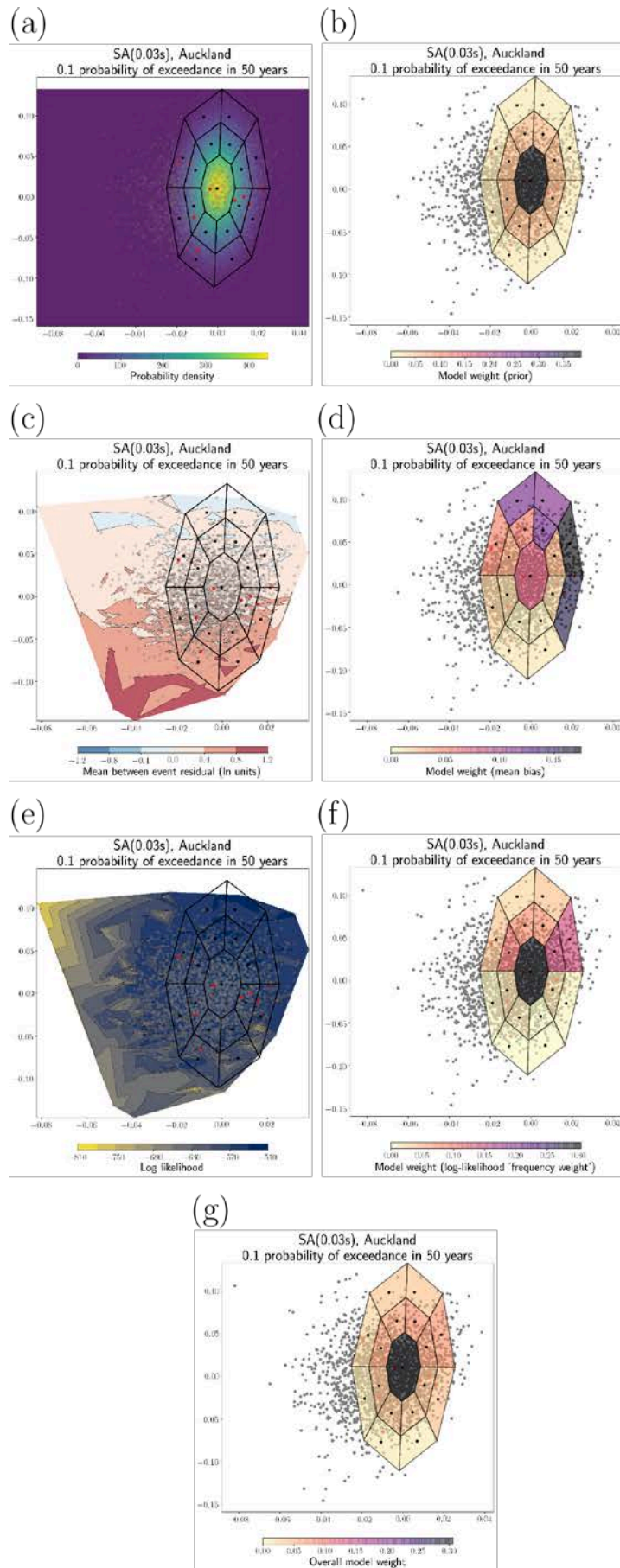


Figure A1.5 Weights for the Auckland suite of SA(0.03 s) models for 0.1 probability of exceedance in 50 years.

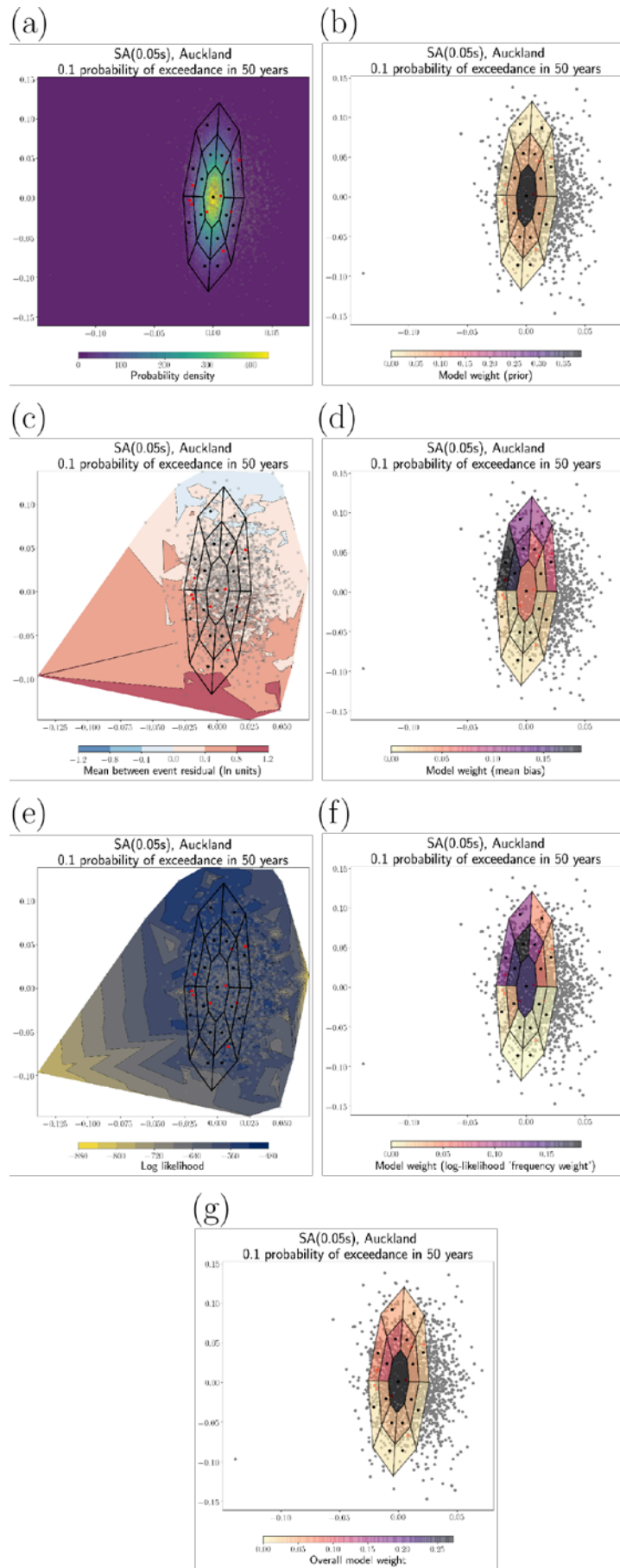


Figure A1.6 Weights for the Auckland suite of SA(0.05s) models for 0.1 probability of exceedance in 50 years.

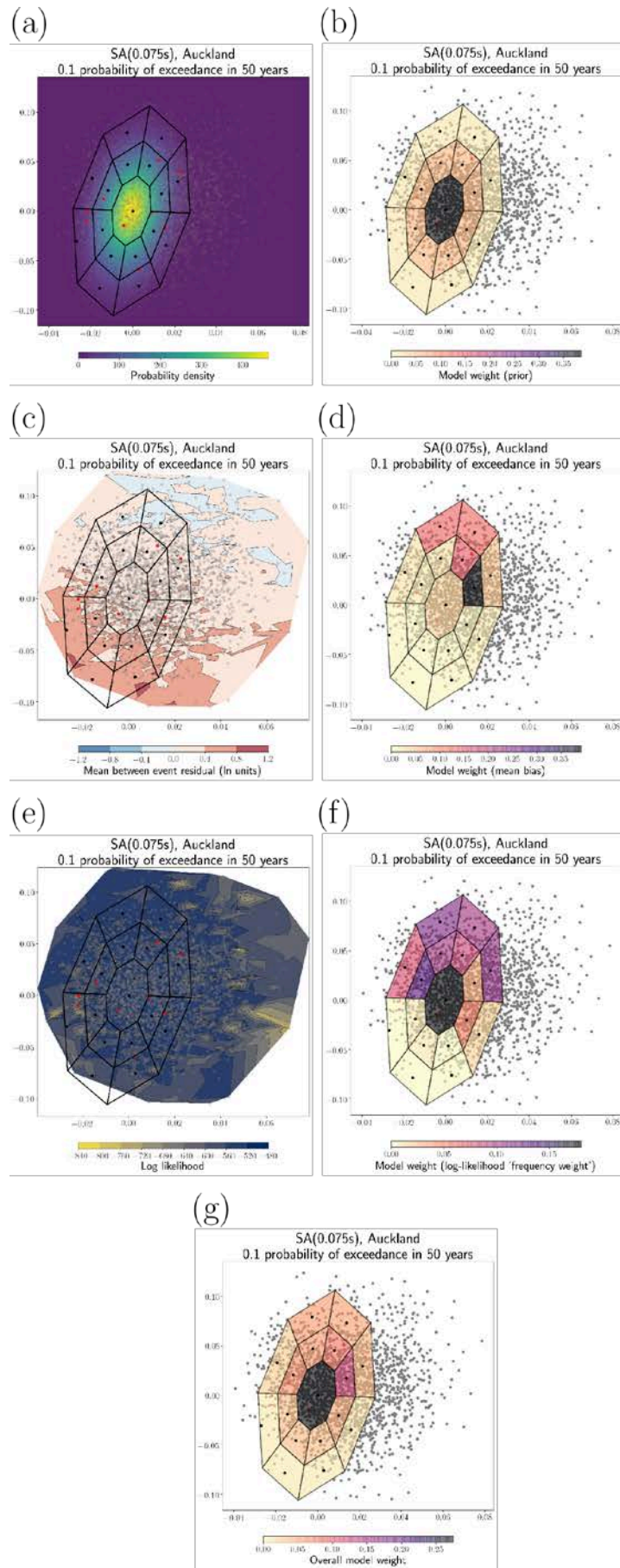


Figure A1.7 Weights for the Auckland suite of SA(0.075 s) models for 0.1 probability of exceedance in 50 years.

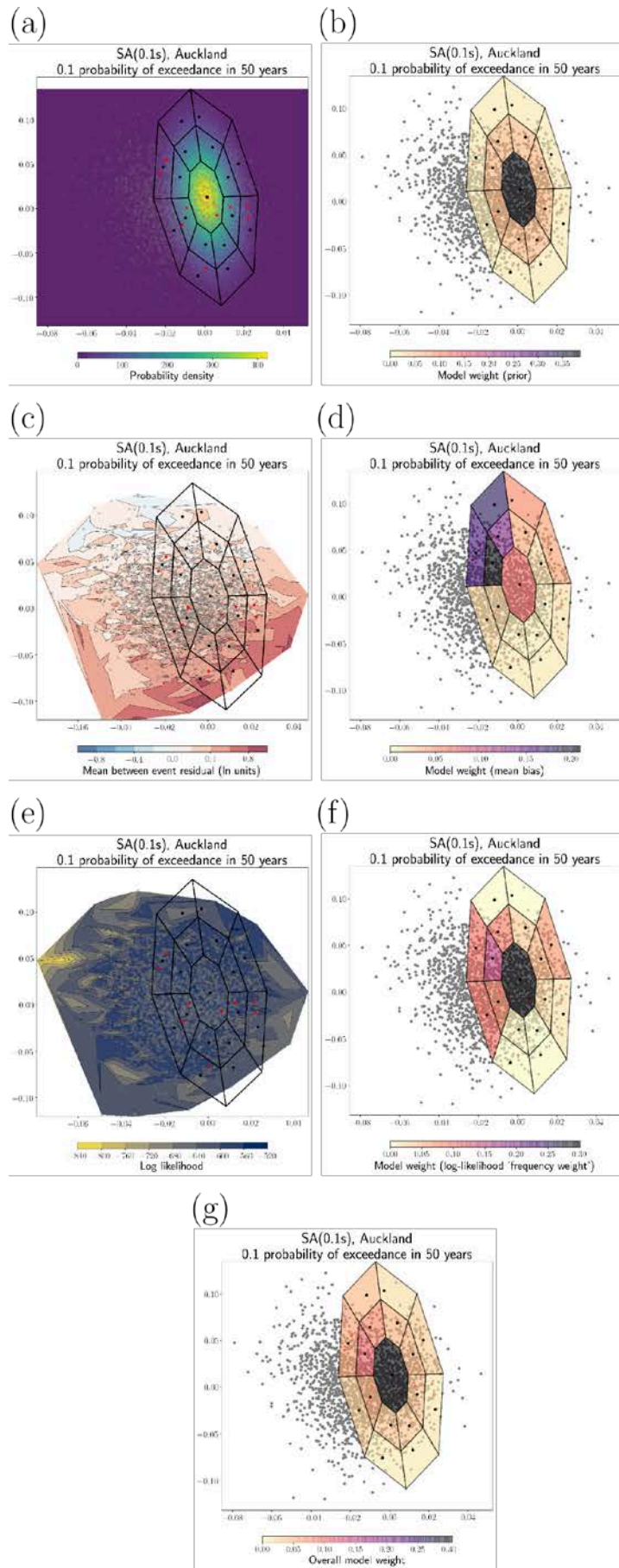


Figure A1.8 Weights for the Auckland suite of SA(0.1s) models for 0.1 probability of exceedance in 50 years.

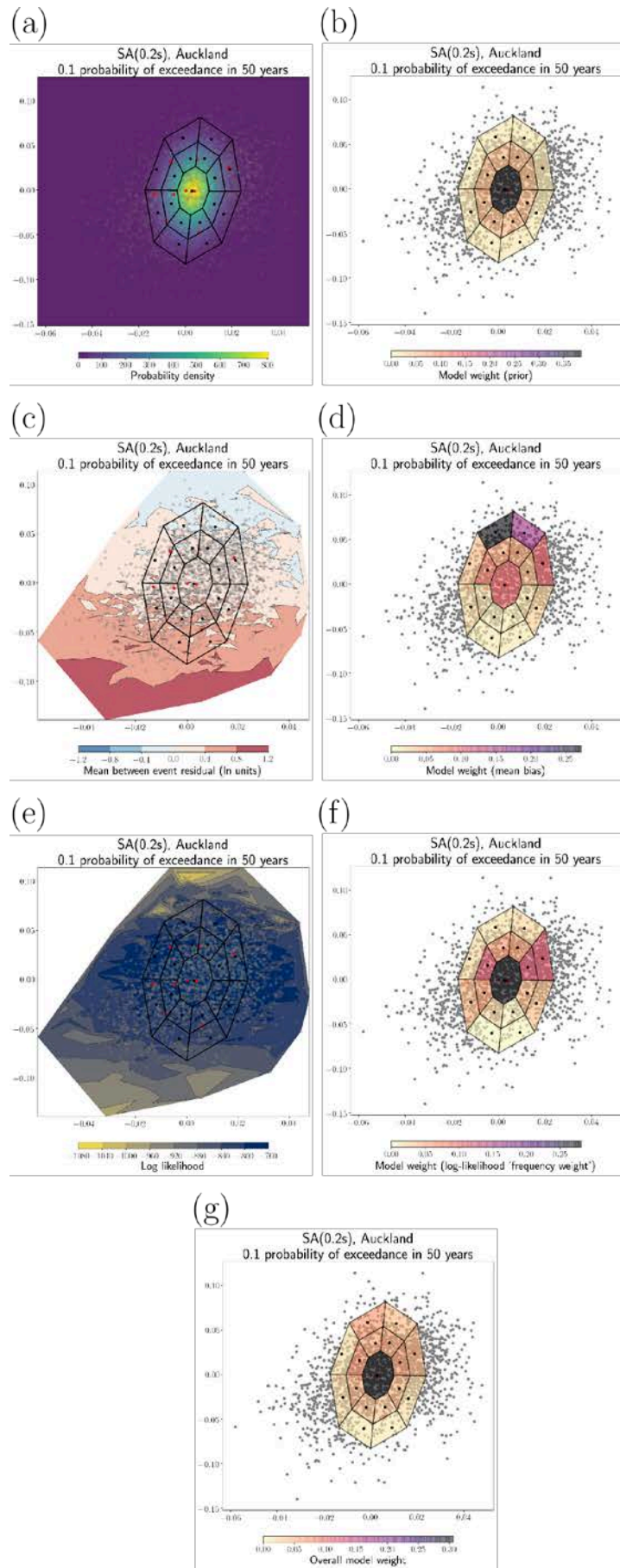


Figure A1.9 Weights for the Auckland suite of SA(0.2 s) models for 0.1 probability of exceedance in 50 years.

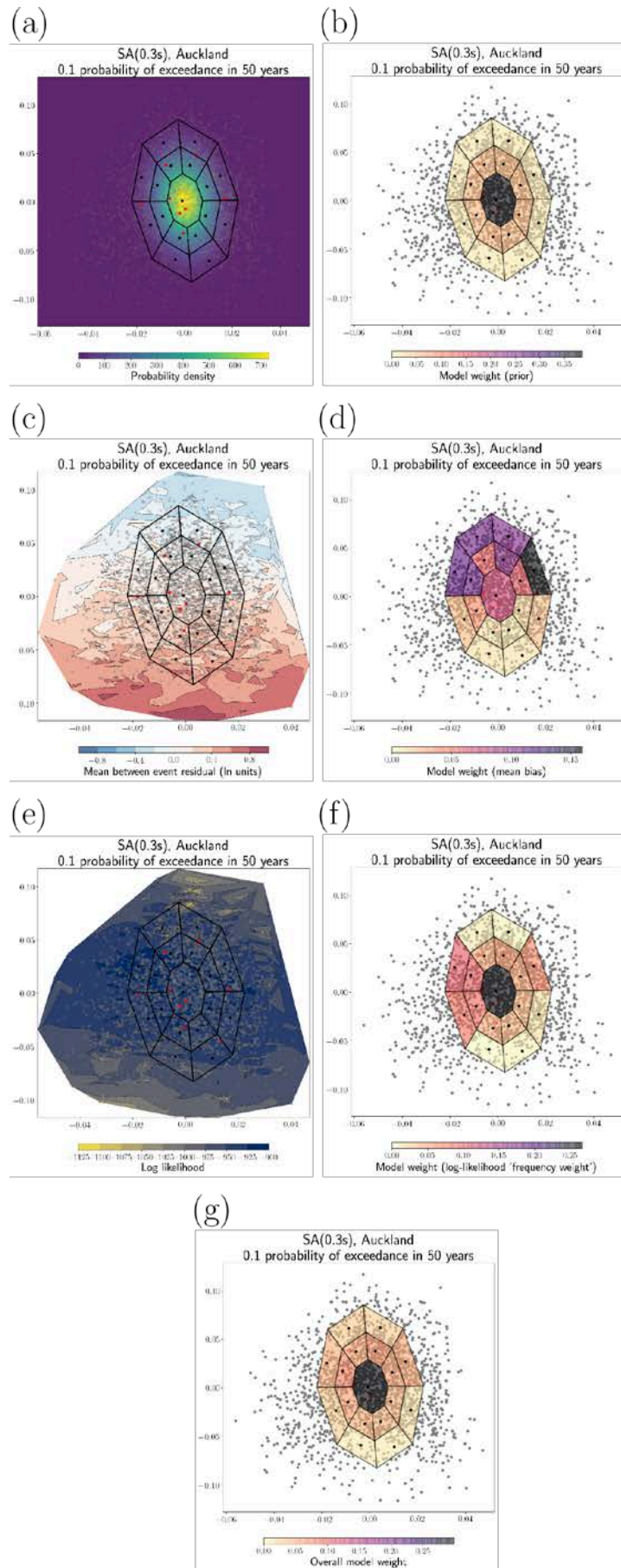


Figure A1.10 Weights for the Auckland suite of SA(0.3s) models for 0.1 probability of exceedance in 50 years.

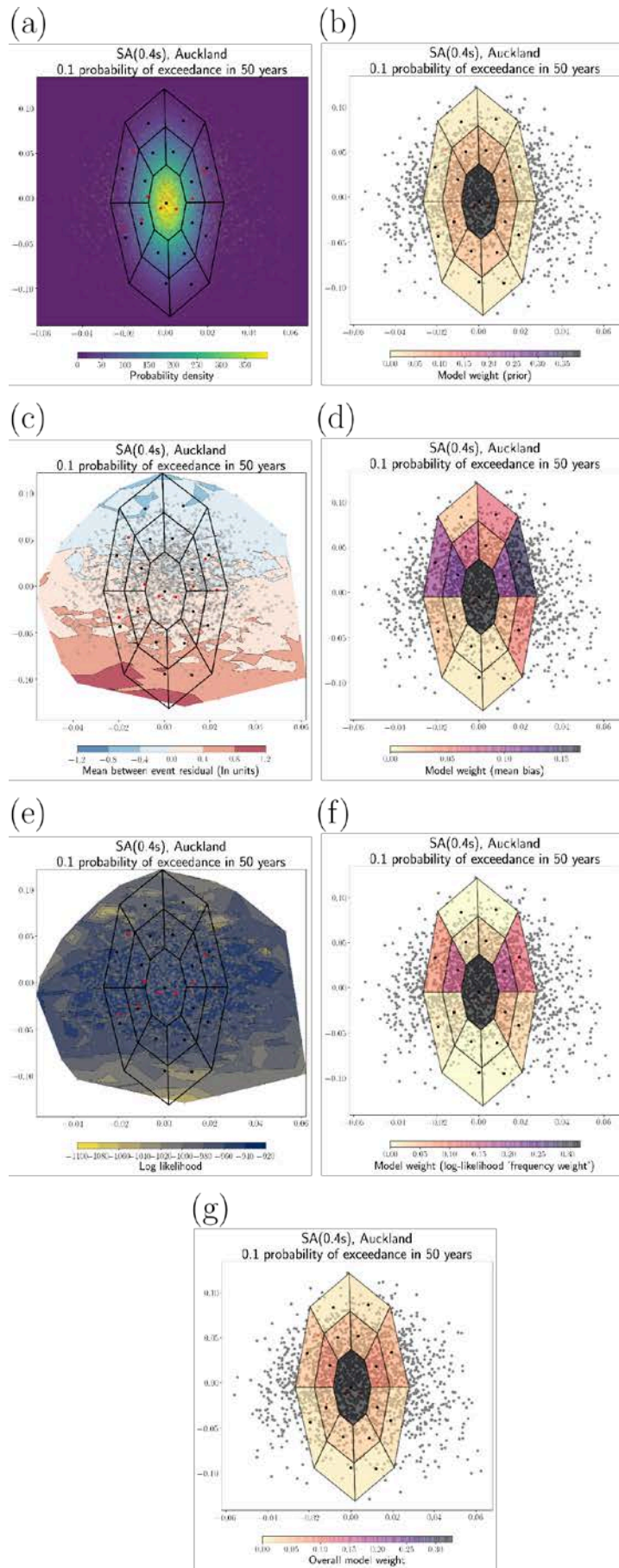


Figure A1.11 Weights for the Auckland suite of SA(0.4s) models for 0.1 probability of exceedance in 50 years.

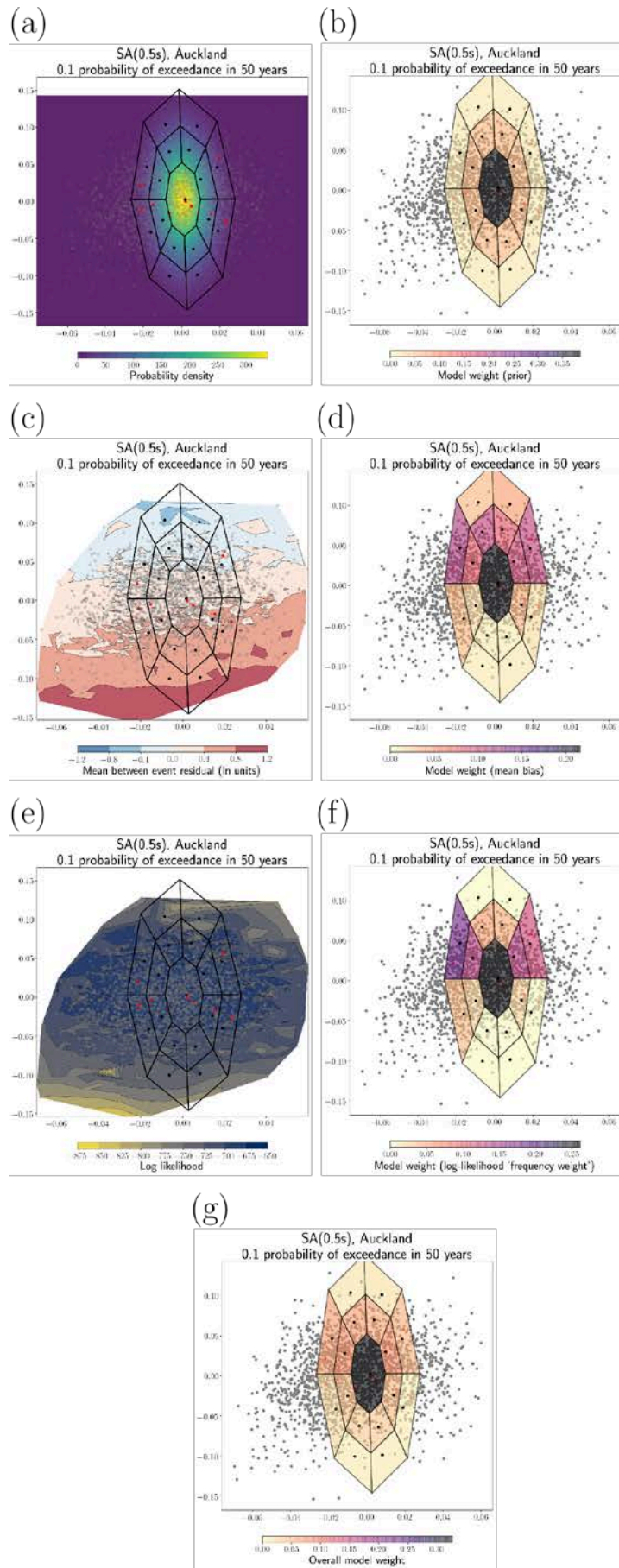


Figure A1.12 Weights for the Auckland suite of SA(0.5s) models for 0.1 probability of exceedance in 50 years.

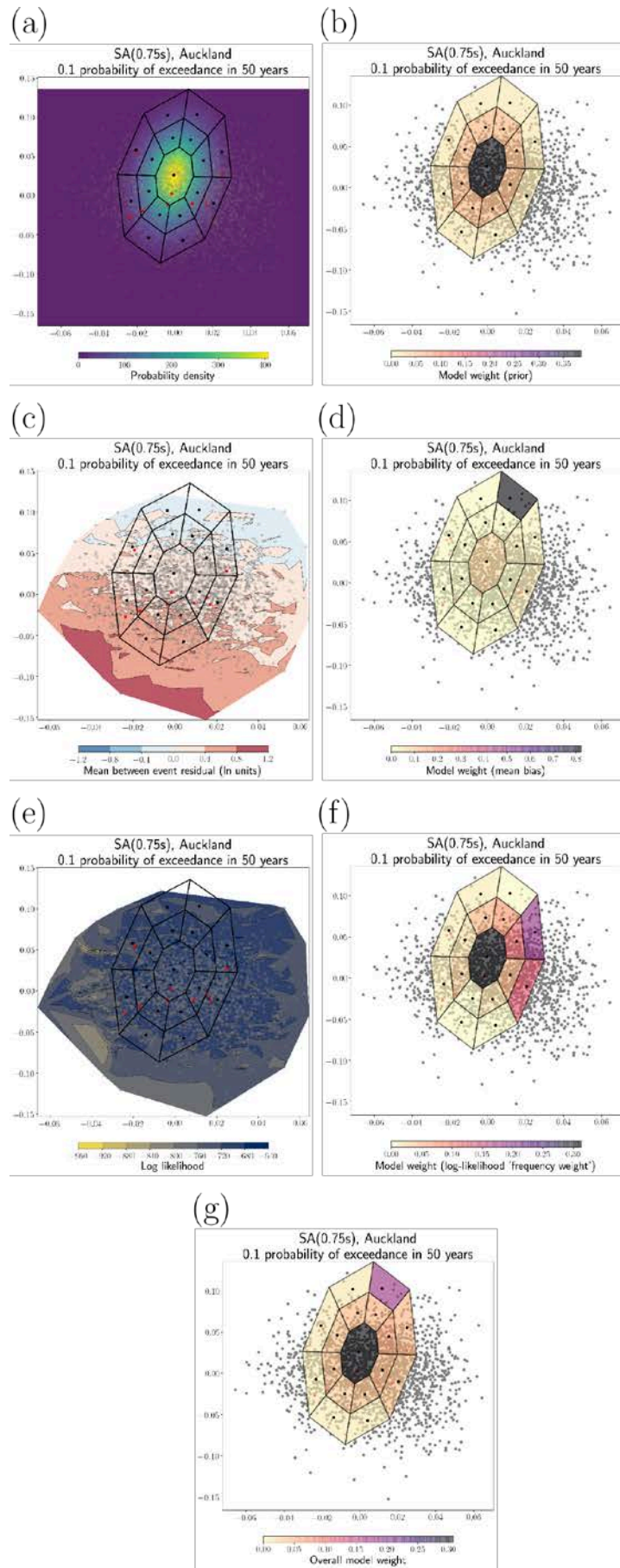


Figure A1.13 Weights for the Auckland suite of SA(0.75s) models for 0.1 probability of exceedance in 50 years.

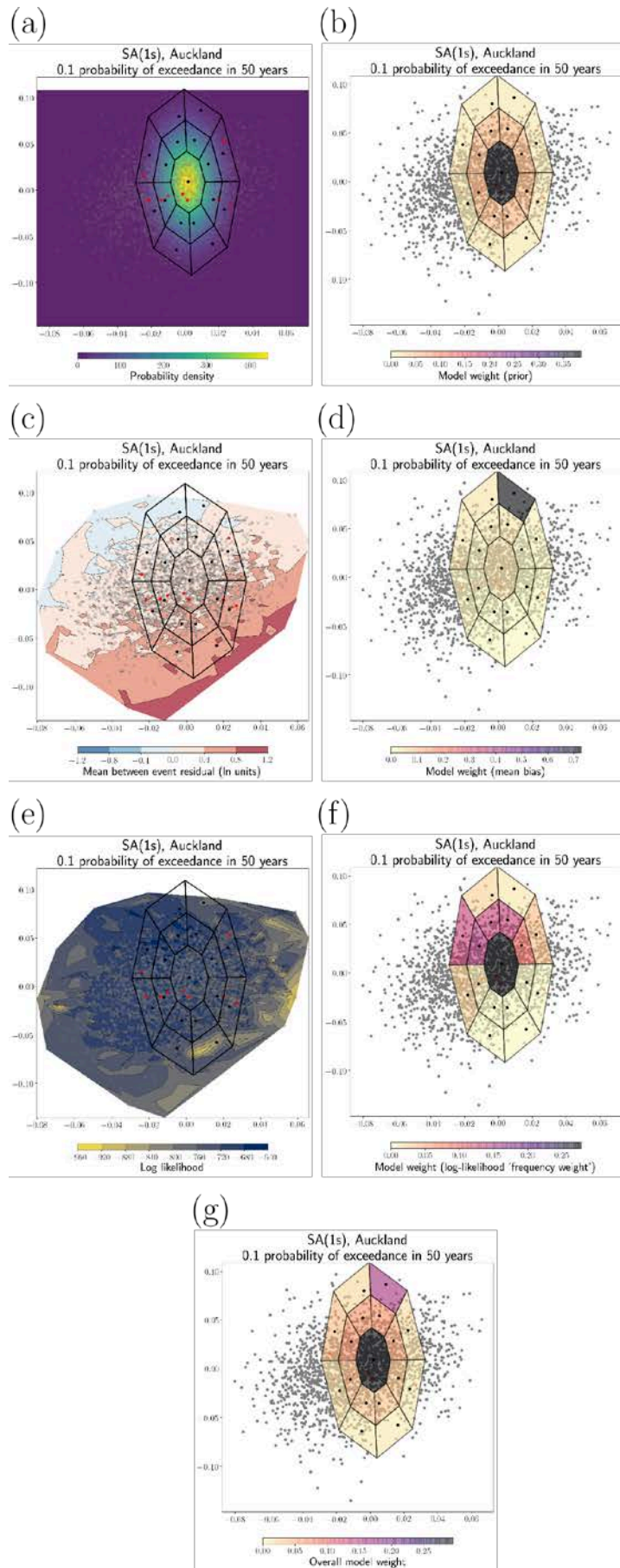


Figure A1.14 Weights for the Auckland suite of SA(1 s) models for 0.1 probability of exceedance in 50 years.

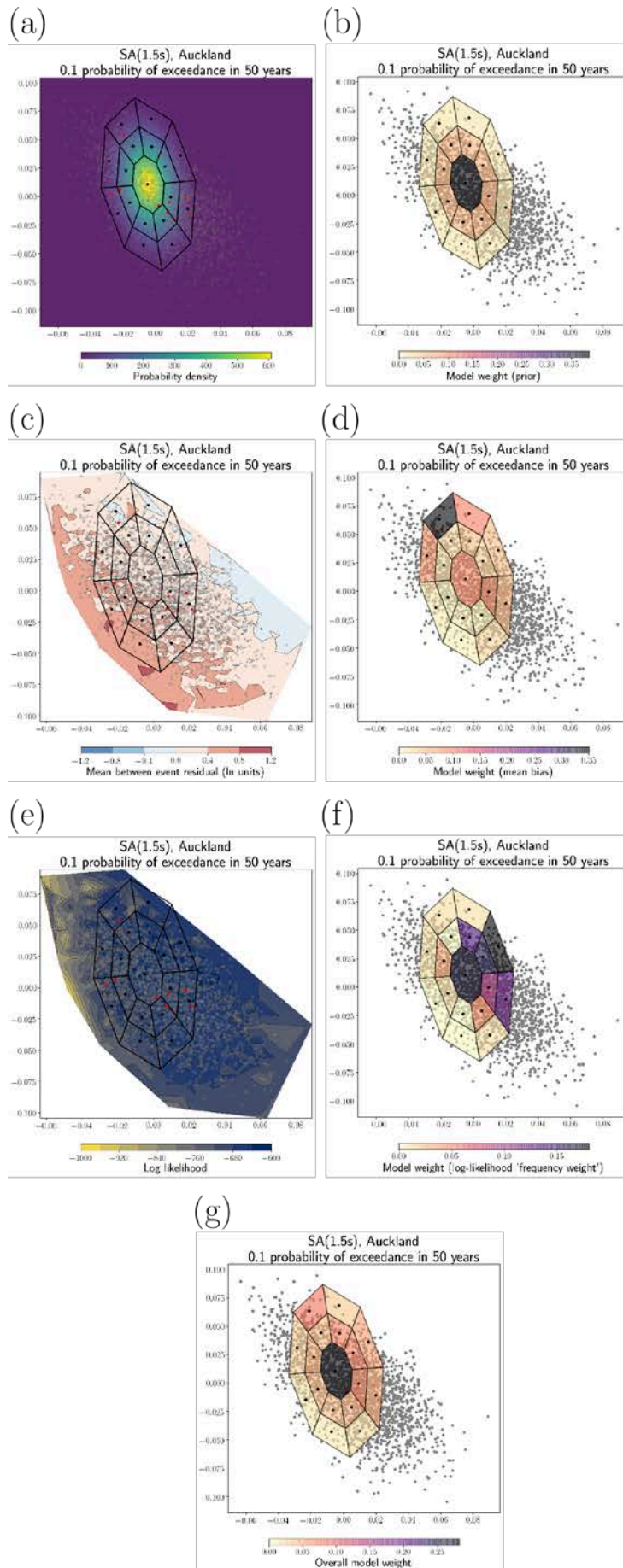


Figure A1.15 Weights for the Auckland suite of SA(1.5 s) models for 0.1 probability of exceedance in 50 years.

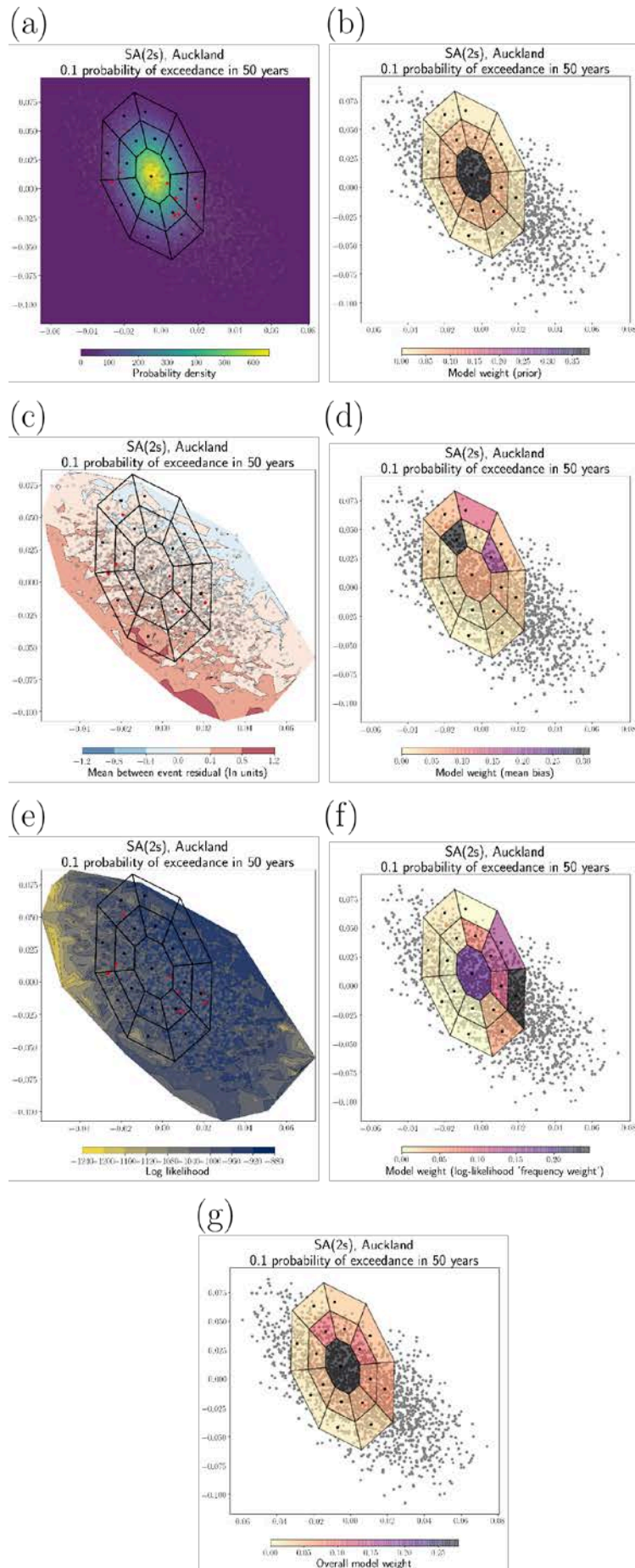


Figure A1.16 Weights for the Auckland suite of SA(2 s) models for 0.1 probability of exceedance in 50 years.

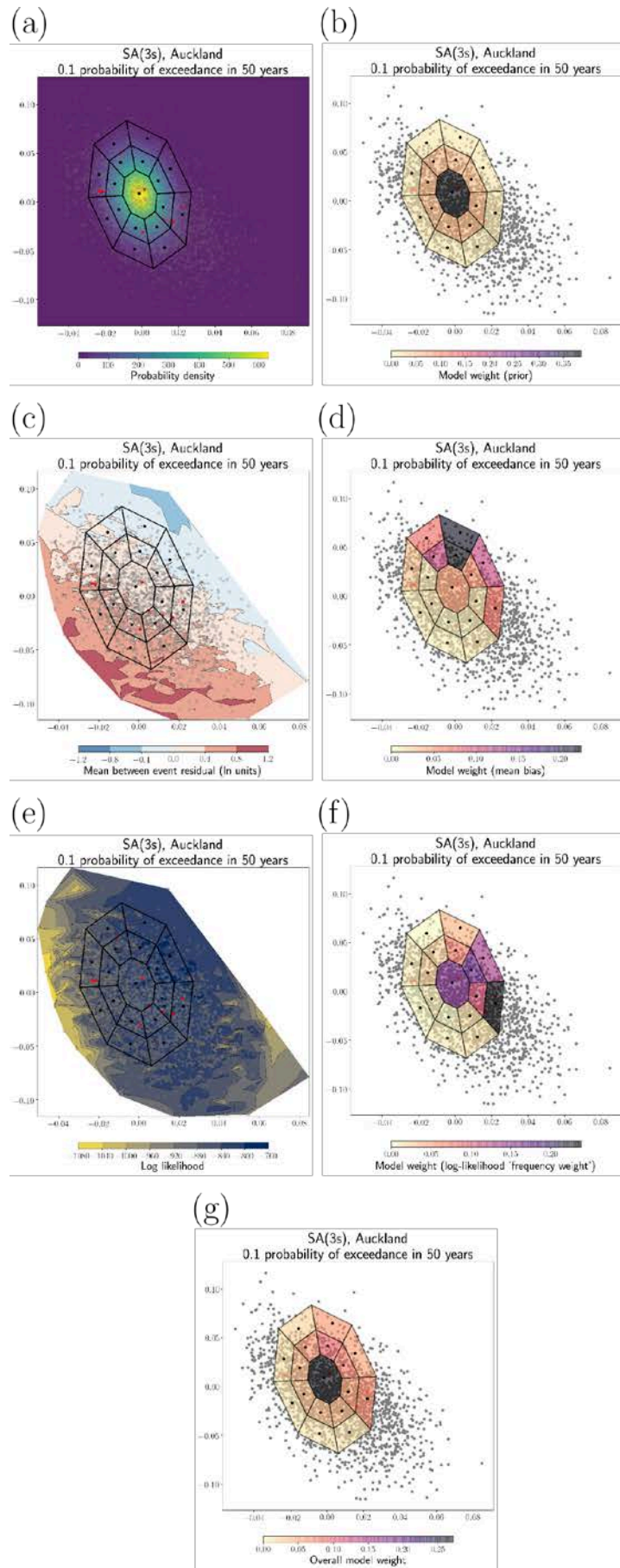


Figure A1.17 Weights for the Auckland suite of SA(3 s) models for 0.1 probability of exceedance in 50 years.

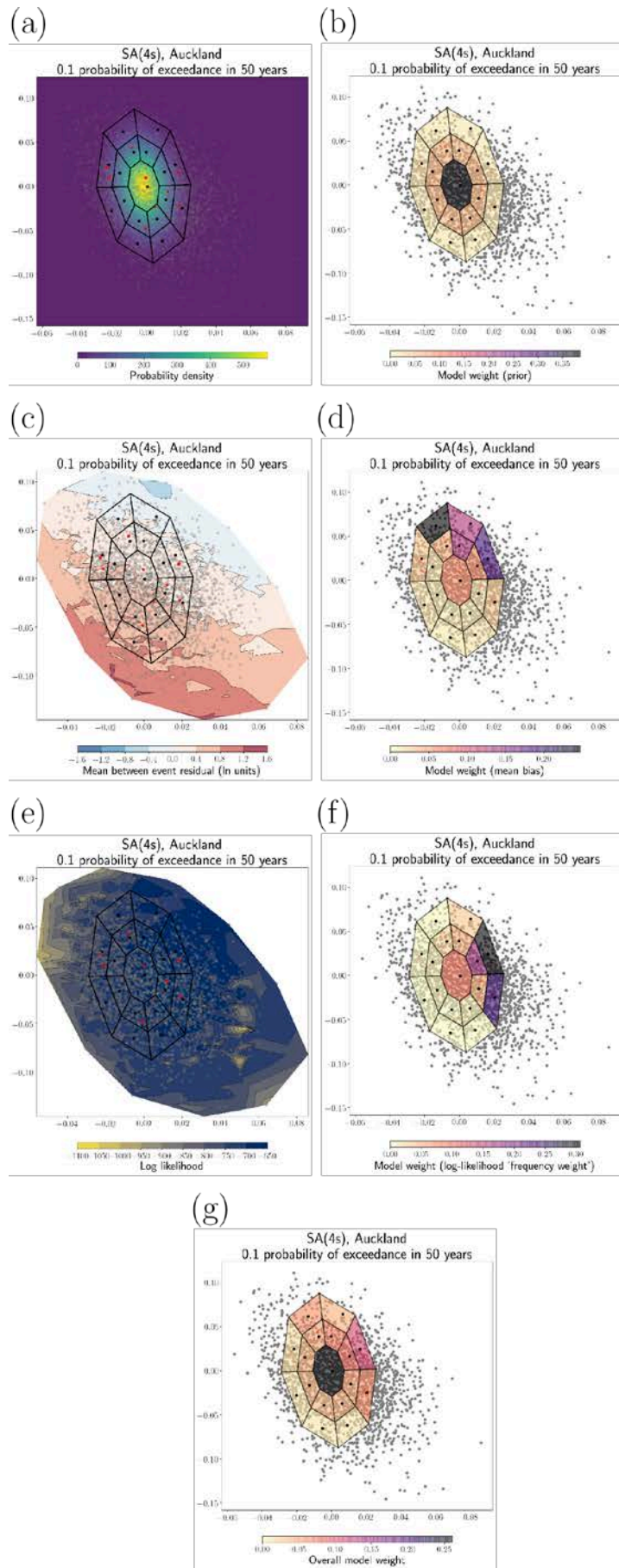


Figure A1.18 Weights for the Auckland suite of SA(4 s) models for 0.1 probability of exceedance in 50 years.

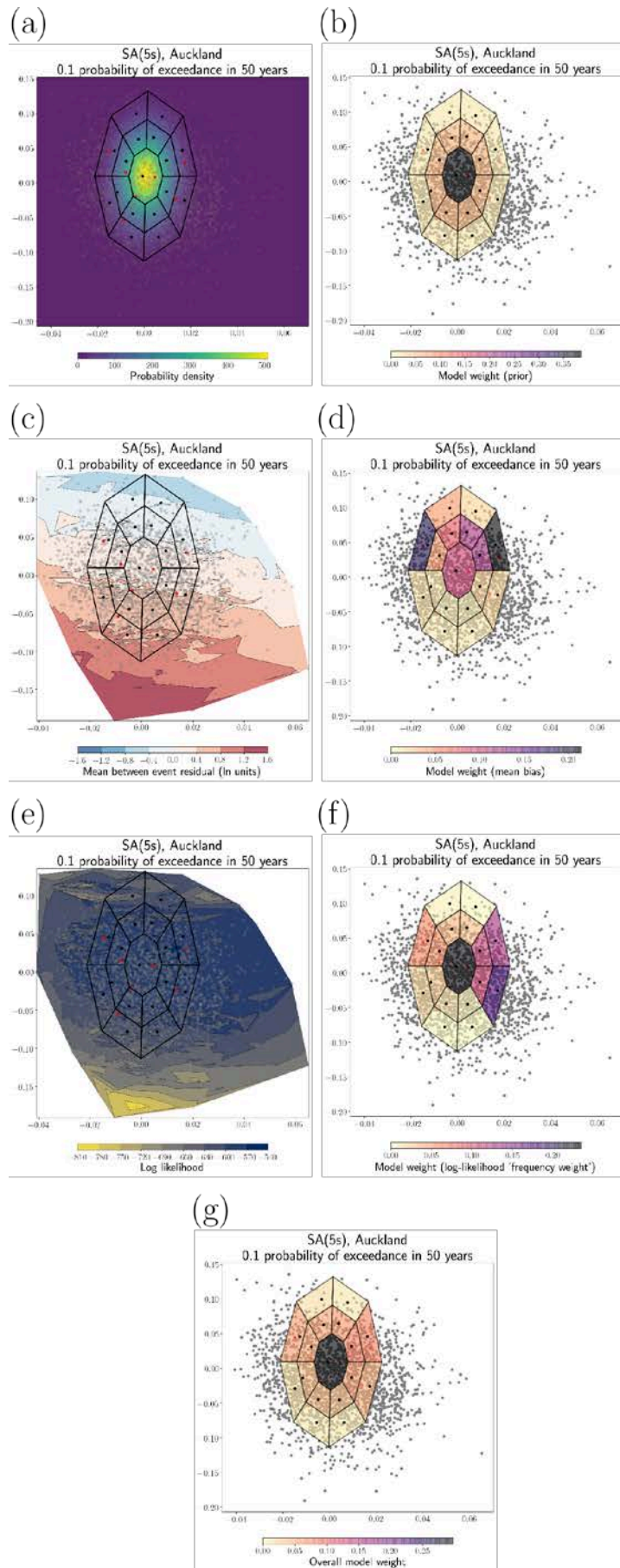


Figure A1.19 Weights for the Auckland suite of SA(5 s) models for 0.1 probability of exceedance in 50 years.

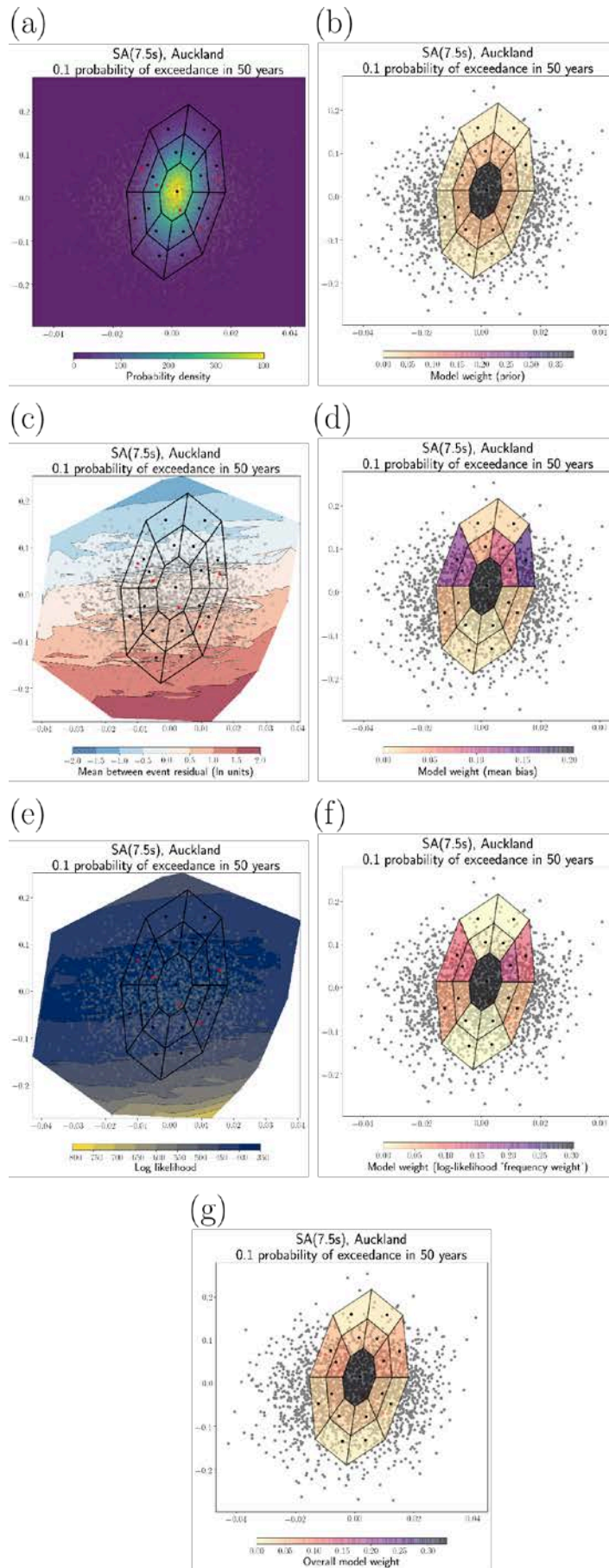


Figure A1.20 Weights for the Auckland suite of SA(7.5s) models for 0.1 probability of exceedance in 50 years.

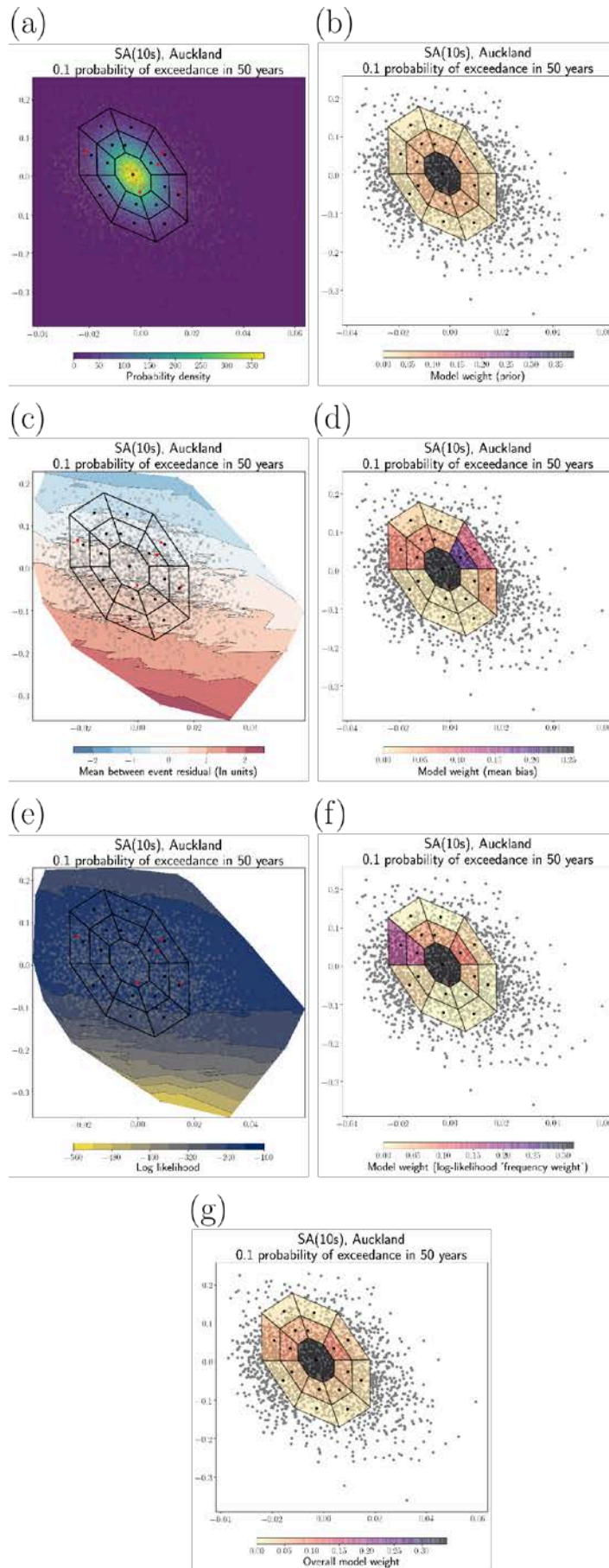


Figure A1.21 Weights for the Auckland suite of SA(10 s) models for 0.1 probability of exceedance in 50 years.



[www.gns.cri.nz](http://www.gns.cri.nz)

#### Principal Location

1 Fairway Drive, Avalon  
Lower Hutt 5010  
PO Box 30368  
Lower Hutt 5040  
New Zealand  
T +64-4-570 1444  
F +64-4-570 4600

#### Other Locations

Dunedin Research Centre  
764 Cumberland Street  
Private Bag 1930  
Dunedin 9054  
New Zealand  
T +64-3-477 4050  
F +64-3-477 5232

Wairakei Research Centre  
114 Karetoto Road  
Private Bag 2000  
Taupo 3352  
New Zealand  
T +64-7-374 8211  
F +64-7-374 8199

National Isotope Centre  
30 Gracefield Road  
PO Box 30368  
Lower Hutt 5040  
New Zealand  
T +64-4-570 1444  
F +64-4-570 4657